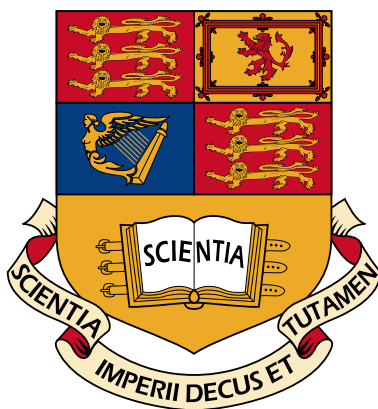


Imperial College London
Department of Mathematics

A Novel Computational Model of the Axoneme for Microswimmers in Stokes Flow

Author:
Peter M. N. Hull

Supervisor:
Dr. Eric E. Keaveny



Submitted in part fulfilment of the requirements for the degree of
MSci Mathematics with a Year Abroad
Imperial College London, June 2020

Abstract

The axoneme is ubiquitous in biology as the fundamental structure for cilia and flagella. These structures, attached to eukaryotic cells, employ complex inner biological processes to enable the swimming of microorganisms such as spermatozoa. In this thesis, a novel two-dimensional model of the axoneme using Kirchhoff filaments inter-connected with geometric time-dependent cross-links is developed to represent the flagellum of a microswimmer in Stokes Flow. Variants of the model are optimised according to a measure of hydrodynamic efficiency, in which a non-trivial relationship between wavenumber and inner driving force amplitude is revealed. The model is modified by introducing and optimising more nuanced tail beating behaviour, and the model is also tested in multiple-swimmer environments in which certain behaviours, such as synchronisation and coordination, are demonstrated.

Declaration

This is my own work except where otherwise stated.

Acknowledgements

There are countless people to thank, without whom the completion of this thesis would not have been possible. First and foremost I would like to thank Dr. Eric Keaveny for his patient supervision and pushing me to dig deeper, Dr. Adam Townsend for helping me build and then debug MATLAB code, and the rest of the team at the multi-filament research group at Imperial College London for countless engaging conversations about tiny wiggling organisms.

I would also like to thank my parents and my sister Noamie for always being there and believing in me. To my friends, in particular my housemates Enrico, Christophe, Austin, Matt and Roland for being my biggest source of inspiration. To Natasha, for her endless love and support every step of the way.

Contents

1	Introduction	1
1.1	Locomotion of Small Organisms	1
1.2	Models for the Axoneme	2
1.3	Overview of Thesis	4
2	Theory	5
2.1	Fundamentals of Stokes Flow	5
2.1.1	Navier-Stokes Equations	5
2.1.2	Stokes Flow	6
2.1.3	Locomotion in Stokes Flow	7
2.2	Rod Theory	8
2.2.1	Elastic Theory	8
2.2.2	Kirchhoff Rod Model	9
2.3	Modelling Kirchhoff Filaments in Stokes Flow	10
2.3.1	Discrete Kirchhoff Rod Model	10
2.3.2	Low-Reynolds Number Hydrodynamics	12
2.3.3	Time Integration Scheme	13
2.3.4	Summary	14
2.4	Conclusion	14
3	Computational Microswimmer Model	16
3.1	Motivation	16
3.2	Two-Dimensional Axoneme Model	17
3.2.1	Force Balance Equation	17
3.2.2	Modelling Active Dynein Motor Proteins as Cross-Linked Spring Forces	18
3.2.3	Retaining Body Structure using Stiff Springs	19
3.2.4	Bending Dynamics using Variable Equilibrium Lengths	19
3.2.5	Notation	20
3.2.6	Parameters for Filament Model	20
3.2.7	Justification	21
3.3	Bending Dynamics	21
3.3.1	Theoretical Understanding	22
3.3.2	Computational Demonstration	23
3.4	Swimmer Model	23
3.4.1	Asymmetric Swimmer	23
3.4.2	Symmetric Swimmer	25
3.4.3	Final Swimmer	26
3.4.4	Non-Undulatory Swimmer	28

3.5	Optimisation	28
3.5.1	Model Selection	29
3.5.2	Parameters	29
3.5.3	Displacement	30
3.5.4	Viscous Dissipation	32
3.5.5	Hydrodynamic Efficiency	35
3.5.6	Final Optimisation	37
3.6	Conclusion	38
4	Further Biological and Environmental Modelling	39
4.1	Variations in Tail Beating	39
4.1.1	Initial Grid Search	40
4.1.2	Finer Grid Search for Head-Driven Swimmers	42
4.2	Multiple Swimmers	43
4.2.1	Model Selection	43
4.2.2	Synchronisation of Out-of-Phase Swimmers	44
4.2.3	Coplanar and Frontal Swimmers	45
4.2.4	Collisions	47
4.3	Conclusion	48
5	Conclusion	49
5.1	Summary of Results	49
5.2	Conclusions, Applications, and Further Work	50
5.3	Code for Multiple Swimmers	51
Bibliography		55
Appendices		56
A	Additional Examples	57
A.1	Bending Dynamics	57
A.1.1	Trigonometric Arc-Length Dependence	57
A.2	Swimming Examples	58
A.2.1	Asymmetric Swimmer, Second Example	58
A.2.2	Swimmers without Passive Links	58
A.2.3	Biologically-Motivated Swimmer	59
B	Hydrodynamic Efficiency	61
C	Coplanar and Frontal Swimmers	63
D	Large-Scale Coordination	65
E	Swimmer Visualisations	67

List of Figures

1.1	The Axoneme (Lindemann & Lesich 2010)	3
2.1	Filament Model	8
3.1	Two-dimensional axoneme model for a microswimmer driven by cross-linked forces. This consists of two connected filaments with 31 segments each, such that segments are visually emphasised as circles. Red and blue links correspond to sets of forces that drive bending. Yellow links correspond to forces that retain structure of the swimmer.	18
3.2	Bending Dynamics of Axoneme Model	22
3.3	Bending Dynamics of Axoneme Model, Computational Result	23
3.4	Motion of Asymmetric Swimmer	25
3.5	Undulation Cycle of Asymmetric Swimmer	25
3.6	Motion of Symmetric Swimmer	26
3.7	Undulation Cycle of Symmetric Swimmer	26
3.8	Motion of Swimmer, Final Model	27
3.9	Undulation Cycle of Swimmer, Final Model	27
3.10	Motion of Non-Undulatory Swimmer	28
3.11	Undulation Cycle of Non-Undulatory Swimmer	29
3.12	Undulation Cycle of Symmetric Swimmer, Small λ_s	30
3.13	Motion of Swimmer, Varying Wavenumber	31
3.14	Motion of Swimmer, Varying Characteristic Amplitude Ratio	31
3.15	Motion of Swimmer, Final Distance from Origin	31
3.16	Viscous Dissipation of Swimmer, Mean and Variance over $t \in [0.2T, T]$. . .	33
3.17	Viscous Dissipation of Swimmer over Time	34
3.18	Hydrodynamic Efficiency of Swimmer	36
3.19	Grid Search over (k_s, λ_s) . For each row (λ_s) a circle gives the highest value and a dotted square gives the lowest value.	38
4.1	Undulation Cycle of Tail-Driven Swimmer ($\beta_A = 2, \zeta = \frac{1}{6}$)	40
4.2	Undulation Cycle of Head-Driven Swimmer ($\beta_A = \frac{1}{16}, \zeta = \frac{1}{5}$)	40
4.3	Grid Search over (ζ, β_A) . For each row (β_A) a circle gives the highest value and a dotted square gives the lowest value.	41
4.4	Fine Grid Search over (ζ, β_A) . For each row (β_A) a circle gives the highest value.	42
4.5	Synchronisation of Swimmers with a Phase Difference $\Delta\phi = \pi - \varepsilon$	44
4.6	Average Individual Swimmer Measurements for Coplanar and Frontal Clusters	46
4.7	Collision Between Three Swimmers	47

4.8	Collision between Multiple Swimmers, Velocity	47
A.1	Bending Motion to Equilibrium, Trigonometric Arc-Length Dependence	57
A.2	Motion of Swimmer, Second Example	58
A.3	Motion of Biologically-Motivated Swimmer	60
C.1	Velocities of Individual Swimmers in Clusters	63
C.2	Average Viscous Dissipation of Individual Swimmers in Clusters	64
C.3	Hydrodynamic Efficiency of Individual Swimmers in Clusters	64
D.1	Multiple Swimmers, Randomised Phase and Amplitude	66
D.2	Multiple Coordinated Swimmers	66
E.1	Undulation Cycle of Second Asymmetric Swimmer	67
E.2	Undulation Cycle of Asymmetric Swimmer	67
E.3	Undulation Cycle of Second Asymmetric Swimmer with No Passive Links . .	67
E.4	Undulation Cycle of Symmetric Swimmer	68
E.5	Undulation Cycle of Symmetric Swimmer with No Passive Links	68
E.6	Undulation Cycle of Swimmer, Final Model	68
E.7	Undulation Cycle of Non-Undulatory Swimmer	68
E.8	Undulation Cycle of Biologically-Motivated Swimmer	68
E.9	Undulation Cycle of Symmetric Swimmer, Small λ_s	69
E.10	Undulation Cycle of Symmetric Swimmer, High Wave Number ($k_s = 4$) . . .	69
E.11	Undulation Cycle of Tail-Driven Swimmer ($\beta_A = 2, \zeta = \frac{1}{6}$)	69
E.12	Undulation Cycle of Head-Driven Swimmer ($\beta_A = \frac{1}{16}, \zeta = \frac{1}{5}$)	69
E.13	Synchronisation of Swimmers with a Phase Difference $\Delta\phi = \pi$	69
E.14	Synchronisation of Swimmers with a Phase Difference $\Delta\phi = \pi - \varepsilon$	70
E.15	Synchronisation of Swimmers with a Phase Difference $\Delta\phi = \frac{\pi}{2}$	70
E.16	Collision Between Two Swimmers	70
E.17	Collision Between Three Swimmers	70
E.18	Large-Scale Behaviour of Coordinated Swimmers	71

List of Tables

3.1	Standard geometrical and forcing parameters for axoneme model.	20
3.2	Standard parameters for filament model.	20
3.3	Parameters for wave propagation.	24
3.4	Parameters for wave propagation, final model.	29
3.5	Standard numerical values for parameters.	30
A.1	Standard parameters for filament lengths.	59

Chapter 1

Introduction

Biological microorganisms such as spermatozoa have been an interest of mathematicians for decades. They are primarily studied within an innovative cross-section of applied mathematics, physics, engineering, scientific computation, and biophysics, with the central goal of implementing numerical computational techniques to understand organism locomotion through complex fluid environments. The methodology used by researchers for this is vast, in which equations governing swimming velocities and biochemical interactions can be analysed computationally using methods including finite differences, boundary element methods, finite element methods, and spectral elements. In particular in this thesis, we bring together ideas from mechanical rod theory, Low-Reynolds number hydrodynamics, numerical ordinary differential equations, and numerical analysis to model cellular organisms and the internal structures of such organisms. The goal of this thesis is the understand the machinery of these models, and to adapt them in a new way in order to better represent the complexities of the inner biological mechanisms that have fascinated researchers across the scientific spectrum.

1.1 Locomotion of Small Organisms

A well documented area of research in biological fluids and mathematical biology is that of locomotion, referring to procedures implemented by living organisms for displacement. Studying the locomotion of cells and small organisms in particular provides an endless area of study for applied mathematicians and experimental biologists. This is due to the wide variety of styles of movement seen in nature, with conditions such as the environment and the scale profoundly influencing how they move.

The primary example of locomotion that we consider in this thesis comes under the term of appendicular locomotion, in which an appendage is used to displace the organism. This is seen in cilia, which is a hair-like appendage which tends to live on cells, often with the role of propelling fluid flow for swimming (Adams et al. 2007). Cilia employ asymmetric beating patterns for this purpose, characterised by a power and recovery stroke (Camalet & Jülicher 2000). Another example, which will be the principal motivation for this thesis, is the spermatozoa, which can move through planar beating cycles or helical wave propagations, with both being observed in sea urchin sperm cells (Woolley & Vernon 2001).

Other single-celled organisms, such as unicellular eukaryotes and migrating metazoans, move

through the quick protusion and retraction of appendages. The result can vary greatly from simple gliding motions to more complex contractions called plasma membrane blebbing characterised by the separation of interlocking protein filaments of the cytoskeleton, fragmenting the cell in order to allow movement (Fackler & Grosse 2008). Similar locomotion has been confirmed computationally, with Lammermann & Sixt (2009) categorising the wide variety of amoeboid locomotion through the differences in force generation and transduction. In contrast to this, many types of bacteria achieve similar gliding motion on surfaces but in the absence of propulsive organelles, instead using helical tracks of proteins (Nan et al. 2014). Furthermore, in myxobacteria there is a secretion of slime, which appears to be necessary for gliding motion Wolgemuth et al. (2002), with reversals in direction being dictated by an internal clock (Zusman et al. 2007).

The *Gordialycus*, a genus of a family of mites called Nematalycidae, exhibit motion similar to that of the earthworms. Instead of sending a travelling wave laterally down the body to undulate, like spermatozoa or snakes, travelling waves are sent through the body, in which there is a contracted zone which is pushed along the body opposite to the direction of travel. These contractions produce backthrust, which propel the mite forward (Bolton et al. 2015). At a larger scale this contrasts to the motion of the earthworm, which has zones of radial expansions periodically moving through the body, a subtle difference in motion not possible for *Gordialycus* due to the lack of circular muscles. On a slightly larger scale for the earthworm, this locomotion is particularly efficient in the small narrow spaces that earthworms inhabit within layers of soil (Juhász & Zelei 2013). This motion is called peristalsis, primarily seen in the human digestive tract as a procedure for moving objects through the esophagus.

These are but a few examples of the way in which small organisms migrate through fluids. We focus on appendicular locomotion which relies on a structure called the axoneme, which brings us to the next topic of how exactly organisms such as cilia work biologically and mathematically.

1.2 Models for the Axoneme

In order to understand the locomotion of cilia and flagella, which are both different iterations of the same sub-structure of cell called an organelle (Lindemann & Lesich 2010), it is important to recognise the complex biological structures that they are composed of. Of particular interest is the active structure referred to as the axoneme, effectively the skeleton of cilia and flagella (Porter & Sale 2000). The axoneme consists of a cylinder made of up nine pairs of microtubules. Microtubules are a form of cytoskeletal filament in the shape of a hollow cylinder formed through a process of polymerisation, typically 23 nanometers in length (Lodish et al. 2000). The different microtubules are inter-connected with proteins, called dynein motor proteins, which drive the movement of the axoneme by applying certain kinds of inner driving forces that cause the microtubules to slide past each-other in the presence of ATP (Gibbons 1981, Porter & Sale 2000). Figure 1.1 visualises this complex architecture, reprinted from Lindemann & Lesich (2010).

Models of cellular locomotion have been studied by mathematicians as early as 1955 when Gray & Hancock (1955) first proposed theoretical models for interpreting the swimming of rotating helical flagellum. However, there are also many modern computational models

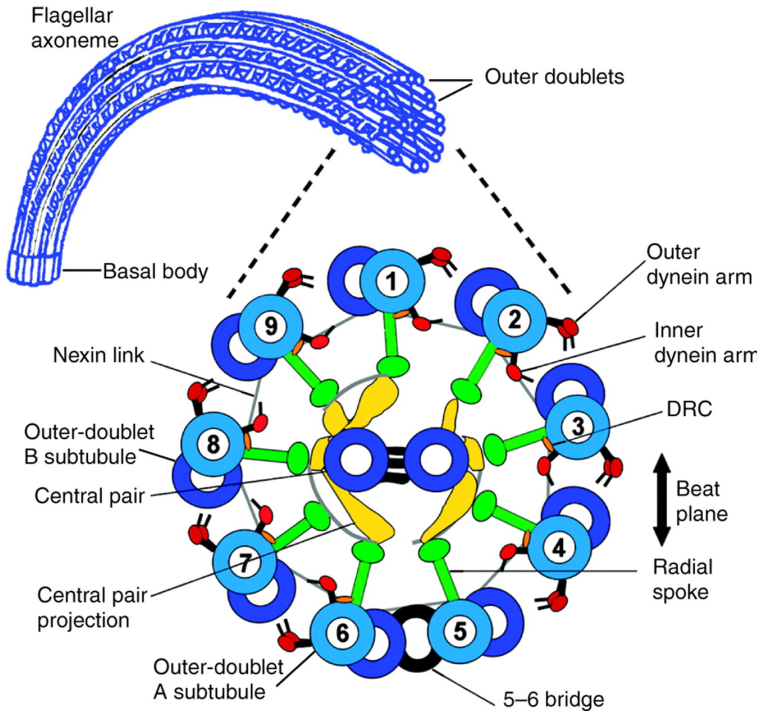


Figure 1.1: The Axoneme (Lindemann & Lesich 2010)

which zoom in on the intricacies of the inner structures of the axoneme to better capture biological behaviours seen in these cilia and flagella, which we review some of here.

In a systematic analysis of experimental findings, Lindemann & Lesich (2010) summarise the main competing views for how the beat cycle of the axoneme is governed: the mechanical geometric clutch model, curvature control, the CP-spoke axis hypothesis, and the cross-bridge cycles of dynein proteins. The geometric clutch model proposes that bends in flagella are due to the positioning of active motor proteins which are able to reach over to adjacent doublets and form a bridge, which instigates a force that brings the doublets together. Secondly, curvature control relies on mechanical information of the curvature of the flagellum for the activation of dyneins, for example when the local curvature passes a certain value certain links are formed, which then instigate bending. The third model relies on a sub-structure of the axoneme called the CP-spoke axis, which is composed of two inner tubes surrounded by the nine pairs of microtubules. Therefore, the CP-spoke axis hypothesis, dating back to 1980, proposes that the spokes connecting the inner two doublets to the outer nine pairs acts as a rotor, cycling through each pair for activation and bending. Finally, the dynein cross-bridge cycle assumes a control mechanism by which dyneins sequentially attach themselves to microtubules through a systematic movement of power stroke and detachment, differing from the geometric clutch model in that the attachments occur due to an internal clock instead of due to geometric information.

Beyond these mechanisms detailed by Lindemann & Lesich (2010), there exist many alternative and hybrid models used by mathematicians that are worth considering individually. Riedel-Kruse et al. (2007) use the cross-bridge cycle hypothesis in a sliding filament model, in which a coarse-grain description of the mechanical behaviour of active and passive cross-links is inferred from analysing the beat patterns of bull sperm using Fourier averaging. This work, loosely based on the analytical study of Camalet & Jülicher (2000), concluded

with the proposition that the sliding of individual filaments that make up the axoneme is determined by detachment rate of the motor proteins, in turn being significantly influenced by the basal constraints at the cell body where the cilia is attached. Finally, Han & Peskin (2018) model the axoneme through a mechanical structure consisting of flexible filaments interconnected by cross-links which represent active motor proteins, and geometric constraints for passive proteins. This system is a hybrid of the geometric clutch model, due to the activation of bridges between doublets, and the curvature control mechanism, due to dynamical systems that change according to curvature. We return to this final model many times in the investigations to follow and use it as inspiration for our own model of an axoneme.

1.3 Overview of Thesis

This work has three aims: to understand the physics required for producing a computational framework to model an individual flexible filament in Stokes Flow, to define a novel model of the axoneme that can be used for microswimmers, and to use the filament model to extensively test the axoneme model. The modelling process results in a novel approach for instigating swimming in microscopic mechanically-modeled organisms, which is inspired by recent research and provides groundwork for further applications and research for deepening our collective understanding of how existing biological microswimmers function.

First, in Chapter 2 we present an outline of the necessary theory to have an understanding of a process for modelling filaments that are then used to represent microswimmers. This includes an overview of fundamental fluid dynamics, locomotion in Stokes Flow, Classical Rod Theory, with the chapter culminating in using these concepts in a full description of a complete framework for modelling filaments in Stokes Flow.

The main section of this thesis, Chapter 3, details the novel model of the axoneme for swimming microorganisms. We commence with a detailed outline of the model and how it can be simulated through the adaptation of an existing hydrodynamic solver. Different implementations of this framework are presented, concluding with a full description of a final model. Variants of the model are tested according to measures commonly used in biofluid dynamics such as viscous dissipation and hydromechanical efficiency.

Chapter 4 presents a variety of experiments evaluating how the model for individual swimmers can be adapted for more advanced biological and environmental considerations. In particular, we develop more nuanced modelling of the tail of the swimmer including an optimisation over different variants, and multiple swimmers are introduced into the same environment. The results obtained refine the model and provide evidence in support of the concept behind the model as a method to capture behaviour of microswimmers in Stokes flow.

The conclusion, Chapter 5, summarises the key results and presents avenues for further research, in particular for further refining and expanding the model, and considering applications such as artificial microswimmers for drug delivery and fertility testing.

Chapter 2

Theory

We start this chapter by presenting an overview of the physics involved in the computational modelling processes for microorganisms such as spermatozoa. The theoretical understanding we seek to achieve concerns the fundamentals of fluid dynamics at Low Reynolds number, consequences of Low Reynolds Number Flow for locomotion, the classical theories of elasticity and elastic rods, and finally a composite numerical model for filaments in Stokes Flow that incorporate all of the above which we use in Chapter 3 for an axoneme model.

2.1 Fundamentals of Stokes Flow

The filament models we examine in this report occur in the environment of Stokes Flow, a simplification of the Navier-Stokes equations. In this section we summarise the relevant well-established theory of the fundamentals of Stokes Flow. This section has been largely adapted from Acheson (1990) and Ruban & Gajjar (2014) unless otherwise stated.

2.1.1 Navier-Stokes Equations

Consider some fluid flow at time t , with velocity \mathbf{u} , position \mathbf{x} , pressure $p = p(\mathbf{x}, t)$, density ρ , and viscosity μ . First we begin with mass conservation of the fluid, which is known as the continuity equation,

$$\frac{D\rho}{Dt} + \nabla \cdot (\rho\mathbf{u}) = 0. \quad (2.1)$$

For our purposes, we consider incompressible flow such that density is constant. Therefore the continuity equation reduces to the much simpler form,

$$\nabla \cdot \mathbf{u} = 0. \quad (2.2)$$

For incompressible fluid flow we can also write down the elements σ_{ij} of the stress tensor, which represent the rate of change of deformation in the fluid,

$$\sigma_{ij} = -p\delta_{ij} + \mu \left(\frac{\partial \mathbf{u}_i}{\partial x_j} + \frac{\partial \mathbf{u}_j}{\partial x_i} \right), \quad (2.3)$$

where we have used the Kronecker-Delta function δ_{ij} . This is the key starting point for modelling fluid flow. Conservation of momentum can be written in terms of the stress tensor, meaning that the material derivative of each velocity component can be written as the following,

$$\rho \frac{D\mathbf{u}_i}{Dt} = \mathbf{f}_i + \frac{\partial \sigma_{ij}}{\partial x_j}. \quad (2.4)$$

such that \mathbf{f}_i are the components of external forces, such as gravity. Using the continuity and constitutive equations to rewrite the components of the momentum equations, and expanding out the material derivative of the velocity, we arrive at the Navier-Stokes equations governing the motion of incompressible fluids,

$$\rho \frac{D\mathbf{u}}{Dt} = \rho \left(\frac{\partial \mathbf{u}}{\partial t} + (\mathbf{u} \cdot \nabla) \mathbf{u} \right) = \mathbf{f} - \nabla p + \mu \nabla^2 \mathbf{u}, \quad (2.5)$$

$$\nabla \cdot \mathbf{u} = 0. \quad (2.6)$$

2.1.2 Stokes Flow

To consider the microscopic scale that organisms such as flagellum and bacteria live in, we introduce the notion of Reynolds number. In essence, the Reynolds number is the ratio of inertial forces to viscous forces (Purcell 1977). More concretely in the case of a fluid flow with typical velocity U past a sphere of radius a ,

$$Re = \frac{\text{Inertial Forces}}{\text{Viscous Forces}} \approx \frac{aU\rho}{\mu}. \quad (2.7)$$

In all our following analysis we deal with Low Reynolds number flows, and so we take $Re \ll 1$ to be small. In other words, we can assume that viscous forces are much more important than inertial forces. In the Navier-Stokes equations shown in Equation 2.5, we know that the $\mathbf{u} \cdot \nabla \mathbf{u}$ term results from inertial forces, and that the $\nabla^2 \mathbf{u}$ term results from viscous forces. Therefore in Stokes Flow we can neglect the inertial term $\mathbf{u} \cdot \nabla \mathbf{u}$. Furthermore, in Low Reynolds Number Flow we assume instantaneity, meaning that the flow is not time-dependent other than in the case of certain boundary conditions. Therefore, we can take these two assumptions into account and rewrite the Navier-Stokes equations in the following way,

$$0 = \mathbf{f} - \nabla p + \mu \nabla^2 \mathbf{u}, \quad (2.8)$$

$$0 = \nabla \cdot \mathbf{u}. \quad (2.9)$$

These are the Stokes equations, which are the governing equations for the environments that organisms such as bacteria live in due to the Low Reynolds number. A well-known consequence of Stokes equations is Stokes' Law, which states in the absence of external forces for a sphere of radius a in a fluid with flow velocity \mathbf{u} , the drag force \mathbf{F}_D on the sphere is linearly related to the velocity,

$$\mathbf{F}_D = 6\pi\mu a \mathbf{u}. \quad (2.10)$$

This is also the case if the fluid is stable and the sphere translates with velocity \mathbf{u} , which is the framing more relevant for our purposes later on. The linearity of Stokes equations is an essential property, which allows for the use of the kinds of computational methods seen later.

2.1.3 Locomotion in Stokes Flow

A key consequence of the governing equations of Stokes flow is that of the type of locomotion permitted. Due to the reversible nature of the fluid flow, swimmers in this environment cannot displace themselves through symmetric movement. This is known as the Scallop Theorem¹. Purcell (1977) explores this phenomenon, noting that in Stokes Flow a scallop cannot move, which arises from only having one degree of freedom in its hinge mechanism of opening and closing, which leads to reciprocal movement. This is due to the fact that at Low Reynolds number, fluid flow is time-reversible meaning that time-reversible motion cannot lead to displacement. This is the reason for which organisms in Stokes Flow display the vast variety of motion discussed in Chapter 1²; microorganisms such as cilia, bacterium, and spermatozoa need to employ non-time-reversible motions such as asymmetric power and recovery strokes or helical wave propagations in order to displace themselves.

Now, there is question of how to model the hydrodynamics associated to biological locomotion such as flagellar beating. We tackle this problem by modeling organisms as individual filaments, with hydrodynamic forces resulting from a balance with internal stress forces of the deforming filaments. In the next section we introduce Classical Rod Theory for formalising this process.

However, there are a number of widely used assumptions that allow for simpler computations of hydrodynamic forces of moving organisms. For example, Resistive-Force Theory (RFT) was introduced by Gray & Hancock (1955) for this purpose, and is a widely used method for modelling flagellar hydrodynamics (Blum & Lubliner 1973, Brokaw 1965, 1972, Lighthill 1975). The main assumption of RFT is that the force per unit length exerted by a segment of the flagellum onto the fluid can be separated into tangential and normal components as follows,

$$\mathbf{F} = \mu (C_N \mathbf{u}_N + C_T \mathbf{u}_T), \quad (2.11)$$

such that \mathbf{u}_N and \mathbf{u}_T are the velocities of the segment normal and tangential to the flagellum respectively, for dimensionless tangential and normal drag coefficients C_T and C_N (Johnson 1979). The forces across the whole length of the flagellum can be obtained by summing up all the individual forces of each segment. The hydrodynamics can then be calculated using widely recognised approximations for the drag coefficients C_N and C_T . For example we can use the original equations given by Gray & Hancock (1955),

$$C_N = \frac{4\pi}{2 \log \frac{2\xi}{a} - 1}, \quad C_T = \frac{1}{2} C_N, \quad (2.12)$$

such that a is the constant radius of the cross-section of the flagellum and ξ is the wavelength of the fully prescribed body shape (Johnson 1979).

However, there are a number of limitations to models such as RFT. Specifically for our case, we want to avoid prescribing the motion of the body, as we want to allow the motion of the swimmer to be a result of more complex inner workings of an axoneme model. The assumptions of RFT are too restrictive for this purpose. Therefore, we instead adopt a mechanical

¹This theorem has been extensively discussed and proved in the literature, and an analytical demonstration can be found in Childress (1981).

²This excludes the earthworm as it does not live in Stokes flow despite displaying time-irreversible movement.

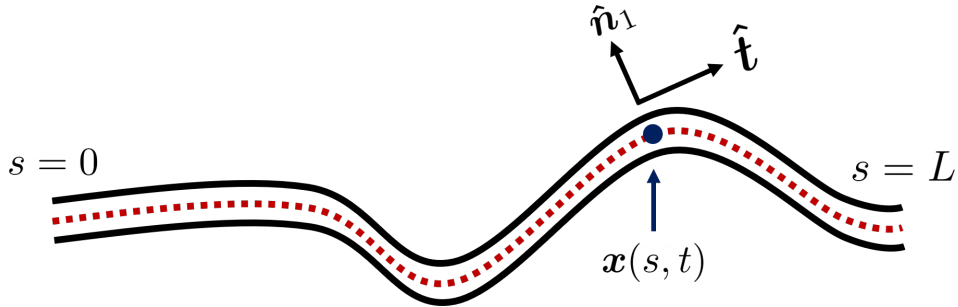


Figure 2.1: Filament Model

model which provides a more appropriate framework for computing hydrodynamic forces associated with more complicated swimmer models.

2.2 Rod Theory

Flagellum have often been modelled in the context of Stokes flow as a single rod, in which the body of the organism is assumed to be an inextensible flexible filament that can deform and bend in order to locomote. Filaments such as this can be modelled using Classical Rod Theory. The main motivation for introducing rod theory is that the elastic forcing that occurs inside microorganisms is as important as the hydrodynamics of the fluids, and computational methods can be built for computing the movement of a deforming rod when the forces due to hydrodynamics are known.

In this section we provide a summary of Rod Models and their mechanical behaviour as detailed in Landau & Lifshitz (1970), Lim et al. (2008), and Audoly & Pomeau (2010). For consistency we use the notation in Schoeller et al. (2019a). We explore the necessary elastic theory and Kirchhoff's Rod Model, which has the basic assumption of taking averages of stress, derived from elastic theory, over cross-sections of a filament.

An inextensible, flexible, and thin filament of length L is described through a position $\mathbf{x}(s, t)$ depending on time t and arc-length $s \in [0, L]$, as seen in the Figure 2.1. For the governing equations, an orthogonal frame $\{\hat{\mathbf{t}}(s, t), \hat{\mathbf{n}}_1(s, t), \hat{\mathbf{n}}_2(s, t)\}$ is used, with $\hat{\mathbf{n}}_2$ out of the page in Figure 2.1.

2.2.1 Elastic Theory

First, we need to define the notion of an internal moment, \mathbf{M} . If a rod is not in its equilibrium position due to an external force, there will be an internal force in response to this that drives bending of the rod. The internal moment is then the vector of internal moments on a certain cross-section of the filament, with the moment of a force being defined as the cross product of the force vector and position vector with respect to a reference or origin point.

For our purposes, we define the constitutive equation for elastic bending moments as follows, which linearly relates the internal moments \mathbf{M} to filament bending

$$\mathbf{M}(s, t) = K_B \left(\left(\hat{\mathbf{t}} \cdot \frac{d\hat{\mathbf{n}}_2}{ds} \right) \hat{\mathbf{n}}_1 + \left(\hat{\mathbf{n}}_1 \cdot \frac{d\hat{\mathbf{t}}}{ds} \right) \hat{\mathbf{n}}_2 \right) + K_T \left(\hat{\mathbf{n}}_2 \cdot \frac{d\mathbf{n}_1}{ds} \right) \hat{\mathbf{t}}, \quad (2.13)$$

such that we define the bending and twist constants K_B, K_T respectively. This gives an equation that relates the shape of the filament to the internal stress. Therefore if the filament is in its equilibrium shape then the internal moments will be zero.

For our purposes, we can further constrain the deformation of the filament to a two-dimensional plane, meaning that the filament only bends in two directions. We assume that about each point, rotation must be aligned with the fixed vector \mathbf{n}_2 , i.e. in Figure 2.1 this corresponds to the unit vector out of the page, so bending can only occur in the plane defined by $\hat{\mathbf{t}}$ and $\hat{\mathbf{n}}_1$. Therefore, we can write \mathbf{M} as

$$\mathbf{M} = K_B \left(\hat{\mathbf{t}} \times \frac{d\hat{\mathbf{t}}}{ds} - \kappa \hat{\mathbf{n}}_2 \right). \quad (2.14)$$

For our purposes κ is constant, which results in internal moments for a filament where the equilibrium shape is straight and uniform. A different equilibrium shape can be introduced by making κ dependent on both the arc-length of the filament and time, which Schoeller et al. (2019a) use in order to give the filament a time-dependent preferred curvature. This is useful if we have the goal of modelling a swimmer as a single rod, as we can assign a preferred curvature at different points in time such that the rod can adopt the form of a travelling wave.

2.2.2 Kirchhoff Rod Model

First, we introduce a kinematic constraint on $\hat{\mathbf{t}}$,

$$\frac{d\mathbf{x}}{ds} = \hat{\mathbf{t}}. \quad (2.15)$$

This ensure that the unit vector $\hat{\mathbf{t}}$ is in the same plane as the deformation of the filament. The kinematic constraint produces internal tension, $\Lambda(s, t)$. This tension also provides inextensibility and the necessary coupling of force and moment balances. Considering external forces \mathbf{f} and torques $\boldsymbol{\tau}$ which act along the filament, and internal moments \mathbf{M} , we can summarise the filament dynamics with the following governing equations,

$$\frac{d\mathbf{x}}{ds} = \hat{\mathbf{t}}, \quad (2.16)$$

$$\frac{d\Lambda}{ds} + \mathbf{f} = 0, \quad (2.17)$$

$$\frac{d\mathbf{M}}{ds} + \hat{\mathbf{t}} \times \boldsymbol{\Lambda} + \boldsymbol{\tau} = 0. \quad (2.18)$$

External forces can include gravitational and applied spring forces. \mathbf{M} is related through a linear relationship to the filament bending and twisting, as shown above. If there are no external forces \mathbf{f} and torques $\boldsymbol{\tau}$, then the preferred curvatures discussed previously will entirely determine the shape of the filament.

These equations need to be coupled with boundary conditions. For our purposes the filament has completely free ends, and so the following simple conditions need to be satisfied,

$$\boldsymbol{\Lambda}(0, t) = \boldsymbol{\Lambda}(L, t) = 0, \quad (2.19)$$

$$\mathbf{M}(0, t) = \mathbf{M}(L, t) = 0. \quad (2.20)$$

Boundary conditions quickly become more complicated in other cases. For example, these conditions do not hold when modelling spermatozoa flagellum with a cell body in the form of a head, with the tethering required between the filament and the head altering the moments and internal tensions at this end.

2.3 Modelling Kirchhoff Filaments in Stokes Flow

In order to simulate the movement of an axoneme in Stokes Flow, we model the axoneme as various inter-connected rods as defined in the previous section. For our purposes, we will be using the method outlined by Schoeller et al. (2019a) for a two-dimensional flexible inextensible filament falling under gravity. In Chapter 3, we implement this method by extensively adapting the code in the supplementary material (Schoeller et al. 2019b) in order to instead build a model for a swimmer. Our model will use two rods and inter-connect them to create a composite model in the form of a swimmer, and the hydrodynamic solver for the filament model by Schoeller et al. (2019a) will allow us to compute the motion of each of the filaments individually.

Previously in this chapter we outlined the relevant physics for this filament model, namely the fundamentals of fluid dynamics and rod theory, along with some ideas of flagellar locomotion. In this section, we give an overview of the filament model by Schoeller et al. (2019a) which brings together the ideas of fluid dynamics and rod theory in order to produce a computational model for a flexible filament in Stokes flow.

2.3.1 Discrete Kirchhoff Rod Model

The goal of this section is to use the physics defined in Section 2.2 to calculate the hydrodynamic forces acting on a filament, which can then be used in the next section to calculate velocities. The forces associated to individual filaments are computed using the Kirchhoff Rod Model detailed in Section 2.2.2. This models each filament as thin, inextensible, flexible, and with a uniform and straight equilibrium shape. The governing equations for the filaments from the Kirchhoff Rod Model are discretised into N segments using a staggering grid and a central differencing scheme to get the following governing equations,

$$\mathbf{x}_{n+1} - \mathbf{x}_n - \frac{\Delta L}{2} (\hat{\mathbf{t}}_{n+1} + \hat{\mathbf{t}}_n) = 0, \quad (2.21)$$

$$\mathbf{M}_{n+0.5} - \mathbf{M}_{(n-1)+0.5} + \frac{\Delta L}{2} \hat{\mathbf{t}}_n \times (\Lambda_{n+0.5} + \Lambda_{(n-1)+0.5}) + \mathbf{T}_n = 0, \quad (2.22)$$

$$\Lambda_{n+0.5} - \Lambda_{(n-1)+0.5} + \mathbf{F}_n = 0, \quad (2.23)$$

where ΔL is the length of a segment, $\mathbf{M}_{n+0.5}$ is the internal moment between segments n and $n + 1$, $\Lambda_{n+0.5}$ is the internal stress between segments n and $n + 1$, $\mathbf{T}_n = \Delta L \boldsymbol{\tau}_n$ is the external torque per unit length on segment n , and $\mathbf{F}_n = \Delta L \mathbf{f}_n$ is the external force per unit length on segment n . These force balances give us equations for \mathbf{F}_n and \mathbf{T}_n . The moments are calculated by discretising Equation (2.14) which resulted from restricting deformation to bending in a plane,

$$\mathbf{M}_{n+0.5} = \frac{K_B}{\Delta L} (\hat{\mathbf{t}}_n \times \hat{\mathbf{t}}_{n+1} - \kappa \hat{\mathbf{n}}_3). \quad (2.24)$$

This restriction also means that the unit vector $\hat{\mathbf{t}}$ tangent to the filament can be written as,

$$\hat{\mathbf{t}}_n = (\cos \theta_n, \sin \theta_n, 0), \quad (2.25)$$

such that θ_n is the angle of segment n from the x -axis.

The external forces and torques represented by \mathbf{F}_n and \mathbf{T}_n respectively can take into account forces due to fields such as gravity, as considered for the sedimentation examples in Schoeller et al. (2019a). However for our purposes in the absence of gravity, the external force \mathbf{F}_n will be a combination of inter-segment steric interactions, hydrodynamic forces, and axonemal forces arising from representations of dynein motor proteins, the latter of which we define in the full swimmer model in Chapter 3. Explicitly, for a single segment of an individual filament we arrive at the following force and torque balance equations,

$$\mathbf{F}_n = \mathbf{F}_n^S - \mathbf{F}_n^H + \mathbf{F}_n^A, \quad (2.26)$$

$$\mathbf{T}_n = -\mathbf{T}_n^H, \quad (2.27)$$

such that for segment n of the filament, \mathbf{F}_n^S are the steric forces on the segment, \mathbf{F}_n^H is the hydrodynamic force³ the segment exerts on the fluid, \mathbf{F}_n^A is the axonemal driving force on the segment, and \mathbf{T}_n^H is the torque the segment exerts onto the fluid. We can have the steric interactions be a known variable, by modelling them as a repulsive force \mathbf{F}_n^S experienced by segment n as in Dance et al. (2004),

$$\mathbf{F}_n^S = \begin{cases} \frac{F^S}{2aR_{nm}} \sum_{m \neq n} \delta_N(m, n) \left(\frac{4a^2\sigma^2 - R_{nm}^2}{4a^2(\sigma^2 - 1)} \mathbf{R}_{nm} \right), & \text{if } R_{nm} < 2a\sigma, \\ 0, & \text{otherwise,} \end{cases} \quad (2.28)$$

$$\delta_N(n, m) = \begin{cases} 0, & \text{if } |n - m| = 1 \\ 1, & \text{otherwise.} \end{cases} \quad (2.29)$$

$\delta_N(n, m)$ removes the repulsive forces for segments that are next to each other in the filament. Furthermore, $\mathbf{R}_{nm} = \mathbf{x}_n - \mathbf{x}_m$, and the distance between segments is notated as $R_{nm} = \|\mathbf{R}_{nm}\|$. The constant F^S controls the overall strength of the interaction. The factor of σ controls how close together the segments are allowed to get to each other, and given that $2a$ is the thickness of the segment, setting $\sigma = 1.1$ prevents the segments overlapping.

To conclude, using a discretisation of the rod model, we can write down a formula for the hydrodynamics of the rod,

$$\mathbf{F}_n^H = \mathbf{F}_n^S + \mathbf{F}_n^A - \mathbf{F}_n \quad (2.30)$$

$$\mathbf{T}_n^H = -\mathbf{T}_n \quad (2.31)$$

such that \mathbf{F}_n is known from Equation (2.23), \mathbf{F}_n^A is known and defined in our full swimmer model in Chapter 3, \mathbf{F}_n^S is known from Equation (2.28), and \mathbf{T}_n^H is known from Equation (2.22). The only additional missing pieces are the values of $\Lambda_{n+0.5}$, associated to the translations and rotations of segments n and $n + 1$, which are computed as the filament deforms. Therefore, we have everything we need to calculate the hydrodynamic forces and torques.

³These are negative to symbolise the force the segment exerts onto the fluid.

2.3.2 Low-Reynolds Number Hydrodynamics

The placement of the filament defined above into a Stokes flow leads to a Low-Reynolds number multiple-body mobility problem. Specifically, the segments are approximated as spheres, giving an N -body problem in which we assume that the motion of the fluid is the result of the motion of the spheres. The hydrodynamic forces and moments are balanced by the internal forces and moments, the inter-segment repulsive forces, and other external forces such as the cross-links that we will introduce later in the composite swimmer body. Therefore the hydrodynamic forces that the segments exert onto the fluid are known, and this can be used to calculate the velocities and angular velocities of the spheres. The velocities and angular velocities of the spheres then can be used to computationally model the movement of the segments of the filament. Due to linearity of Stokes flow, the following linear relationship results,

$$\begin{pmatrix} \mathbf{u} \\ \boldsymbol{\Omega} \end{pmatrix} = \mathcal{M} \cdot \begin{pmatrix} \mathbf{F}^H \\ \mathbf{T}^H \end{pmatrix}, \quad (2.32)$$

such that $\mathbf{u} = (\mathbf{u}_1, \dots, \mathbf{u}_N)$ and $\boldsymbol{\Omega} = (\boldsymbol{\Omega}_1, \dots, \boldsymbol{\Omega}_N)$ contain the velocities and angular velocities of each segment respectively. This can be thought of as a generalisation of Stokes Law as seen in Section 2.1, which introduces the linear relationship between the frictional force produced by a sphere of radius a moving with velocity \mathbf{u} ,

$$\mathbf{F}^H = 6\pi\mu a \mathbf{u}. \quad (2.33)$$

with the generalisation stemming from the addition of more spheres, and taking into account the local disturbances in the flow field caused by the inter-sphere interactions.

In this model, the coefficients of the mobility matrix \mathcal{M} are calculated by a direct evaluation of the RPY tensor seen in Wajnryb et al. (2013). Firstly, for an undisturbed flow, in which we assume there are N spheres of radius a that do not overlap, we can write the following relation down,

$$\begin{pmatrix} \mathbf{u}_n \\ \boldsymbol{\Omega}_n \end{pmatrix} = \sum_{m=1}^N \begin{pmatrix} \boldsymbol{\mu}_{nm}^{tt} & \boldsymbol{\mu}_{nm}^{tr} \\ \boldsymbol{\mu}_{nm}^{rt} & \boldsymbol{\mu}_{nm}^{rr} \end{pmatrix} \begin{pmatrix} \mathbf{F}_n^H \\ \mathbf{T}_n^H \end{pmatrix}, \quad (2.34)$$

such that $\boldsymbol{\mu}_{nm}$ are the components of the mobility tensor \mathcal{M} which give information on the drag forces between spheres n and m . The superscripts t and r refer to friction due to translation and rotation respectively. Note that if we only have one sphere, i.e. $N = 1$, then we can write the components as

$$\boldsymbol{\mu}_{11}^{tt} = \frac{1}{\zeta_{tt}} \mathbf{1}, \quad \boldsymbol{\mu}_{11}^{rr} = \frac{1}{\zeta_{rr}} \mathbf{1}, \quad \boldsymbol{\mu}_{11}^{rt} = \boldsymbol{\mu}_{11}^{tr} = 0, \quad (2.35)$$

where ζ_{tt}, ζ_{rr} are the frictional coefficients and $\mathbf{1}$ is the identity. For a single sphere, we can then write,

$$\begin{pmatrix} \mathbf{u} \\ \boldsymbol{\Omega} \end{pmatrix} = \begin{pmatrix} \boldsymbol{\mu}_{11}^{tt} & \mathbf{0} \\ \mathbf{0} & \boldsymbol{\mu}_{11}^{rr} \end{pmatrix} \begin{pmatrix} \mathbf{F}^H \\ \mathbf{T}^H \end{pmatrix} = \begin{pmatrix} \frac{1}{\zeta_{tt}} \mathbf{1} & \mathbf{0} \\ \mathbf{0} & \frac{1}{\zeta_{rr}} \mathbf{1} \end{pmatrix} \begin{pmatrix} \mathbf{F}^H \\ \mathbf{T}^H \end{pmatrix}. \quad (2.36)$$

Finally, we note that this can be rewritten as follows,

$$\mathbf{u} = \frac{1}{\zeta_{tt}} \mathbf{F}^H, \quad \boldsymbol{\Omega} = \frac{1}{\zeta_{rr}} \mathbf{T}^H. \quad (2.37)$$

Note that the equation for \mathbf{u} is exactly the statement of Stokes Law, such that $\zeta^{tt} = 6\pi\mu a$.

However, our model will of course require $N > 1$ to have a sufficiently discretised rod composed of N spheres. Therefore we need the components of the mobility matrix for each pair of particles n, m in order to calculate their velocities and angular velocities. For this, Wajnryb et al. (2013) deduce the translational-rotational, the purely rotational, and the purely translational mobilities to be the following respectively,

$$\boldsymbol{\mu}_{nm}^{rt} = [\boldsymbol{\mu}_{nm}^{tr}]^T = \begin{cases} \frac{1}{8\pi\mu R_{nm}^3} (\boldsymbol{\varepsilon} \cdot \mathbf{R}_{nm}), & \text{if } n \neq m, \\ \mathbf{0}, & \text{if } n = m. \end{cases} \quad (2.38)$$

$$\boldsymbol{\mu}_{nm}^{rr} = \begin{cases} \frac{1}{16\pi\mu(R_{nm})^5} (3\mathbf{R}_{nm}\mathbf{R}_{nm} - R_{nm}^2 \mathbf{1}), & \text{if } n \neq m, \\ \frac{1}{6\pi\mu a} \mathbf{1}, & \text{if } n = m. \end{cases} \quad (2.39)$$

$$\boldsymbol{\mu}_{nm}^{tt} = \begin{cases} \frac{1}{3R_{nm}^2} (3R_{nm}^2 + 2a^2) \mathbf{1} + \frac{1}{R_{nm}^4} (R_{nm}^2 - 2a^2) \mathbf{R}_{nm}\mathbf{R}_{nm}, & \text{if } n \neq m, \\ \frac{1}{8\pi\mu a} \mathbf{1}, & \text{if } n = m. \end{cases} \quad (2.40)$$

In the above formulae, we use the same notation as in the previous section with $\mathbf{R}_{nm} = \mathbf{x}_n - \mathbf{x}_m$, and the magnitude of the separation between the two spheres being notated as $R_{nm} = \|\mathbf{R}_{nm}\|$. Finally, we also used the three-dimensional Levi-Civita symbol $\boldsymbol{\varepsilon}$, such that for a vector $\boldsymbol{\rho}_k$ we have $(\boldsymbol{\varepsilon} \cdot \boldsymbol{\rho}_k) = \varepsilon_{\alpha\beta\gamma}\rho_{k\gamma}$, where $\varepsilon_{\alpha\beta\gamma}$ is the standard Levi-Civita symbol which is 1 for cyclic permutations of $\{\alpha, \beta, \gamma\}$, -1 for acyclic permutations, and 0 otherwise. The equations are simplified from a more general form where spheres are allowed to overlap, however assuming that spheres do not overlap is a reasonable assumption to make given that we enforce it in the steric interactions for the rod model.

To summarise, given the forces and torques on the segments of the filament as a result of the Kirchhoff Rod Model, the segments are considered as spheres in Stokes Flow, and the velocities and angular velocities can be directly computed using the components of the mobility matrix defined above which only depend on the inter-sphere distances. Therefore given a filament and the forces due to deformation, we have a direct method to compute the instantaneous velocities.

2.3.3 Time Integration Scheme

Now that the velocities and angular velocities for the segments of the filament can be calculated using the hydrodynamic forces, we need to step in time to model the deformation of the rod in time. In order to implement a time dependence and a time integration scheme, we start with the following expressions resulting from earlier restrictions,

$$\frac{d\mathbf{x}_n}{dt} = \mathbf{u}_n, \quad (2.41)$$

$$\frac{d\theta_n}{dt} = \Omega_n, \quad (2.42)$$

$$\mathbf{x}_{n+1} - \mathbf{x}_n = \frac{\Delta L}{2} (\hat{\mathbf{t}}_n + \hat{\mathbf{t}}_{n+1}). \quad (2.43)$$

Due to the restriction of bending the plane, the angle θ_n and the angular velocity $\Omega_n = (0, 0, \Omega_n)$ are one dimensional, and $\hat{\mathbf{t}}_n$ can be written only in terms of the angle θ_n as in Equation (2.25). Next, a timestep size Δt is defined, and we seek to find the positions and

angles at time $k + 1$, denoted here as \mathbf{x}_n^{k+1} and θ_n^{k+1} respectively, given the positions \mathbf{x}_n^k and angles θ_n^k of a segment n at time k .

An additional mechanism is introduced to reduce the number of variables in the system, which comes in the form of the following equation,

$$\mathbf{x}_n^{k+1} = \mathbf{x}_1^{k+1} + \frac{\Delta L}{2} \sum_{m=2}^n (\hat{\mathbf{t}}_{m-1}^{k+1} + \hat{\mathbf{t}}_m^{k+1}). \quad (2.44)$$

This allows us to determine the entire position of the filament using only the position and orientation of the first segment. The positions \mathbf{x}_n and angles θ_n are updated by using an implicit second-order backwards differential formula (BDF), as seen in Ascher & Petzold (1998), giving us our final set of equations

$$\mathbf{x}_1^{k+1} = \frac{4}{3}\mathbf{x}_1^k - \frac{1}{3}\mathbf{x}_1^{k-1} + \frac{2}{3}(\Delta t)\mathbf{u}_1^{k+1}, \quad (2.45)$$

$$\theta_n^{k+1} = \frac{4}{3}\theta_n^k - \frac{1}{3}\theta_n^{k-1} + \frac{2}{3}(\Delta t)\Omega_n^{k+1}, \quad (2.46)$$

$$\mathbf{x}_1^{k+1} + \frac{\Delta L}{2} \sum_{m=2}^n (\hat{\mathbf{t}}_{m-1}^{k+1} + \hat{\mathbf{t}}_m^{k+1}) = \frac{4}{3}\mathbf{x}_n^k - \frac{1}{3}\mathbf{x}_n^{k-1} + \frac{2}{3}(\Delta t)\mathbf{x}_n^{k+1}, \quad (2.47)$$

which gives a discretised time integration scheme that can be used to find the positions and angles of the first segment of the filament, with the values for remaining segments being consequently updated by using Equation (2.44). This is a non-linear system that can be expressed as $\mathbf{h}(\mathbf{Z}^*) = 0$ where \mathbf{Z}^* contains the updated position for the first segment, angles, and internal force Lagrange multipliers $\Lambda_{n+0.5}^{k+1}$. The non-linear system is then solved by using *Broyden's method* as defined by Broyden (1965), a well-known method we omit here.

2.3.4 Summary

To summarise, the model we use considers a filament placed in Stokes flow. The filaments are discretised into N segments, and are modelled using the Kirchhoff Rod Model such that the internal moments can be entirely determined by the shape of the filament. Internal moments along with other known factors such as inter-segment repulsive forces and external forces balance with hydrodynamic forces, meaning that the hydrodynamic forces can be calculated. Using a generalisation of Stokes law, the velocities and angular velocities of the segments can be calculated by treating each of the N segments of the rod as an individual sphere in an N -body Stokes flow mobility problem using the hydrodynamic forces and a mobility matrix that defines the linear force-velocity relationship. Then, now that velocities and angular velocities are known, time-stepping using an implicit scheme along with an additional simplification provides a non-linear system for the positions, angles, and internal forces. Finally, this non-linear system is solved by Broyden's Method, providing the measurements for the next point in time.

2.4 Conclusion

In this chapter, the details necessary for modelling microswimmers as connected filaments in Stokes Flow were summarised, as well as the related fundamental concepts such as Navier-Stokes equations and Kirchhoff Rod Models. The theoretical framework in Section 2.3 takes

in a wide variety of ideas across applied mathematics, and is an innovative method for modelling filaments in fluids. In the next chapter, we take the final discrete computational model for a rod in Stokes Flow presented here and develop it into a full model of a two-dimensional axoneme, developing the composite body into a microswimmer that can move through viscous fluids.

Chapter 3

Computational Microswimmer Model

3.1 Motivation

In *Spontaneous oscillation and fluid-structure interaction of cilia*, Han & Peskin (2018) propose a geometrical model for representing bending dynamics of cilia and flagellum. This model treats a cilium as a 3D mechanical structure with discrete levels connected by different types of dynamical forces, representing the forces generated by passive and active dynein links in the axonemal architecture of the cilia. These dynamical forces generate the bending dynamics required for beating.

The model presented by Han & Peskin (2018) consists of a $9+2$ arrangement of microtubules, as explored in Chapter 1, which discretises a cilium into 11 space-curves in \mathbb{R}^3 . These space-curves are anchored to correspond to the attachment of cilium to a cell body, and geometric constraints are imposed to retain a certain structure. The geometric constraints effectively amount to a stack of cross-sections that can only move in rigid translations, with twist and tilting not being permitted. The motion of the structure is driven by a dynamical modelling of the active dynein motors proteins that are present in the cross-sections of actual cilium. The most important modelling decision is that the active links generate a tension according to the following equation

$$\frac{dT_k^{(j)}}{dt} = \beta \left(K_k \left(L_k^{(j)} \right)^2 - T_k^{(j)} \right) \quad (3.1)$$

such that $T_k^{(j)}$ is the tension between adjacent nodes on levels k and $k-1$ for $k = 1, \dots, N$, where N is the number of segments per filament, $j = 1, \dots, 4, 6, \dots, 9$, $L_k^{(j)}$ is the instantaneous length of the link between connected nodes, K_k is a level-dependent constant, and β is a scaling constant. This assumes that at any given point in time the only information available to the filaments is the instantaneous length between certain cross-links.

Equation (3.1) can be interpreted holistically as follows. There is a negative feedback loop present in the tension, i.e. as tension in a link increases, the growth in tension decreases. An increase in tension means the forcing between the linked segments increases, and so physically our intuition tells us the segments are brought together. This decreases the instantaneous length $L_k^{(j)}$, and so in the equation we see that the growth in tension is further decreased

on top of the self-inhibition. This means the tension will eventually work in the opposite direction as the length-squared term will be very small compared to the tension, and so the opposite behaviour will follow, i.e. an increase in the separation between the segment. The above pattern then happens again but in reverse, with the segments achieving their maximum separation, leading to a much larger length-squared term compared to tension, which increases tension. Consequently this increases the pulling force between the segments and thus physically pulls them back together. Han & Peskin (2018) take advantage of this cycle of tension and release to generate a beating pattern in the cilia model.

The conclusion we take from this study is that cylindrical biological organisms can be modelled as filaments which are connected by active cross-links, which deform in certain ways in order to drive the whole body into motion. In the following we outline a model inspired by this, which will be in 2D and will replace the dynamical tension equation by a wave propagation on cross-link equilibrium lengths.

3.2 Two-Dimensional Axoneme Model

In this section we outline a two-dimensional mechanical system, which will be used as a loose representation of the axoneme, seen in swimming microorganism such as spermatozoa or cilia. The complex three-dimensional $9+2$ axonemal architecture of flagella which produce the planar beating patterns that can be observed can be represented effectively in a two-dimensional system, in which the axoneme is represented by two elastic inextensible beams separated by some fixed distance (Camalet & Jülicher 2000, Riedel-Kruse et al. 2007, Hilfinger et al. 2009). This commonly used simplification, along with the cross-link mechanisms presented by Han & Peskin (2018), are the primary motivations for the system we create here. Note that we will simply refer to the composite structure as a *swimmer*, refraining from referring to it as a particular biological structure such as a flagellum, cilia, sperm or bacterium.

Using similar notation to that in Han & Peskin (2018), we model the configuration of the swimmer as 2 discretised space curves in \mathbb{R}^2 with N points each,

$$\{\boldsymbol{x}_{i,n} : n = 1, \dots, N\}_{i=1}^2 \quad (3.2)$$

Each space curve corresponds to a flexible inextensible filament as defined in Section 2.3 of Chapter 3, and so we will refer to each space curve as a *filament*, and each point as a *segment* of the filament.

3.2.1 Force Balance Equation

In Equation (3.3) of Section 2.3, in which we detail the force balances which take place in the filament model, we use $\mathbf{F}_{i,n}^A$ to represent the forces arising from the inner driving forces of the axoneme. Therefore we can rewrite the force balance equation for segment n of filament i as follows,

$$\mathbf{F}_{i,n} = \mathbf{F}_{i,n}^S - \mathbf{F}_{i,n}^H + \mathbf{F}_{i,n}^A, \quad (3.3)$$

$$\mathbf{F}_{i,n}^A = \mathbf{F}_{i,n}^{(a)} + \mathbf{F}_{i,n}^{(b)} + \mathbf{F}_{i,n}^{(c)}, \quad (3.4)$$

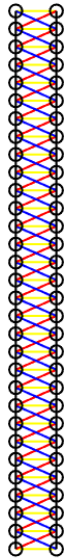


Figure 3.1: Two-dimensional axoneme model for a microswimmer driven by cross-linked forces. This consists of two connected filaments with 31 segments each, such that segments are visually emphasised as circles. Red and blue links correspond to sets of forces that drive bending. Yellow links correspond to forces that retain structure of the swimmer.

in which we represent all of the forces generated by the inner workings of the axoneme as $\mathbf{F}_{i,n}^A$. In the following, we define the forces $\mathbf{F}_{i,n}^{(a)}$ and $\mathbf{F}_{i,n}^{(b)}$ that model active dynein motor proteins, and $\mathbf{F}_{i,n}^{(c)}$ which enforces an overall swimmer shape.

3.2.2 Modelling Active Dynein Motor Proteins as Cross-Linked Spring Forces

The forces $\mathbf{F}_{i,n}^{(a)}$ and $\mathbf{F}_{i,n}^{(b)}$ are defined with the goal of modelling active dynein motor proteins in the form of cross-linked forces that are time-dependent with variable equilibrium lengths. Specifically for $n = 1, \dots, N - 1$, we get the following set of forces,

$$\mathbf{F}_{1,n}^{(a)}(t) = -k^{(a)} \left(l_{n,n+1}(t) - r_{n,n+1}^{(a)}(t) \right), \quad (3.5)$$

$$\mathbf{F}_{2,n+1}^{(a)}(t) = -\mathbf{F}_{1,n}^{(a)}(t), \quad (3.6)$$

$$\mathbf{F}_{1,n+1}^{(b)}(t) = -k^{(b)} \left(l_{n+1,n}(t) - r_{n+1,n}^{(b)}(t) \right), \quad (3.7)$$

$$\mathbf{F}_{2,n}^{(b)}(t) = -\mathbf{F}_{1,n+1}^{(b)}(t). \quad (3.8)$$

$\mathbf{F}_{i,n}^{(\Xi)}(t)$ is the force applied to segment n of filament i at time t due to the set of links Ξ . This force is a two-dimensional vector, with x and y components. $\Xi = a, b$ correspond to the red and blue links respectively in Figure 3.1. $l_{n,m}(t)$ is the distance at time t between segments n and m of filaments 1 and 2 respectively. $k^{(\Xi)}$ is a spring constant, and $r_{n,m}^{(\Xi)}(t)$ refers to a time-dependent equilibrium length between segments n and m of filaments 1 and 2 respectively. Note that the bending in our system will rely on equilibrium lengths varying according to time, segment, and filament, which we detail in Section 3.2.4.

3.2.3 Retaining Body Structure using Stiff Springs

The three-dimensional model in Han & Peskin (2018) introduces the following geometrical constraint for some constant H , and for $n \in \{1, \dots, N\}$,

$$|\mathbf{x}_{1,n} - \mathbf{x}_{2,n}| = H. \quad (3.9)$$

This forces the model to retain an equilibrium distance between the microtubules, or outer *walls*, of the motile cilia. For our swimmer, we replace this geometric constraint with a set of forces $\mathbf{F}_{i,n}^{(c)}$ that come in the form of stiff springs. This is an alternative way of achieving the same outcome of retaining some sort of constant thickness and structure as it bends and swims, and instead of prescribing a fixed distance between filaments we have a preferred distance. This relationship will come from the following set of forces for $n \in \{1, \dots, N\}$,

$$\mathbf{F}_{1,n}^{(c)}(t) = -k^{(c)} (l_{n,n}(t) - r_{n,n}^{(c)}(t)), \quad (3.10)$$

$$\mathbf{F}_{2,n}^{(c)}(t) = -\mathbf{F}_{1,n}^{(c)}(t). \quad (3.11)$$

Similarly to the active links, $\mathbf{F}_{i,n}^{(c)}$ refers to the force resulting from the spring force applied to segment n of filament i , and these forces are applied for $n = 1, \dots, N$. k_c is some spring constant, which will dictate to what extent the swimmer retains a constant thickness, with $k^{(c)} \gg k^{(a)}$ and $k^{(c)} \gg k^{(b)}$ resulting in a swimmer that is very resistant to losing a constant cross-section in reaction to the active cross-links. The stiff springs modelled here are visualised by the yellow links in Figure 3.1.

3.2.4 Bending Dynamics using Variable Equilibrium Lengths

The bending in the system will be instigated by varying the equilibrium lengths along arc-length of the filaments, and by adding in time-dependence in order to instigate swimming. Formally, the previously defined equilibrium lengths will be modelled as follows,

$$r_{n,n+1}^{(a)}(t) = r_0^{(a)} + \lambda^{(a)} f^{(a)}(n, t), \quad (3.12)$$

$$r_{n+1,n}^{(b)}(t) = r_0^{(b)} + \lambda^{(b)} f^{(b)}(n, t), \quad (3.13)$$

$$r_{n,n}^{(c)} = r_0^{(c)}. \quad (3.14)$$

$r_0^{(\Xi)}$ refers to set constants for characteristic equilibrium length for $\Xi = a, b, c$. $\lambda^{(\Xi)}$ refers to characteristic amplitudes, and $f^{(\Xi)}(n, t)$ is a segment and time-dependent function, for $\Xi = a, b$. We often refer to $f^{(\Xi)}(n, t)$ as the function relating to inner driving forces.

In sperm cells there is a slow variation in cross-sectional area along the length of the flagellum (Johnson 1979, Chemes & Sedo 2012). However here for the passive links c we decide to have a constant equilibrium length with respect to arc-length and time to simulate a constant cross-sectional area. This is because motion is largely dictated by the amplitude of undulation, meaning that variation in cross-sectional area can be neglected (Johnson 1979). However, a variation in cross-sectional area, for example for the purposes of modelling a tapered tail, can also be enabled in this model. This can be done by introducing a segment and time-dependent addition to $r_{n,n}^{(c)}$, as seen above for the active links a and b .

3.2.5 Notation

In all of the examples to come the two principal amplitudes are equal, i.e. $\lambda^{(a)} = \lambda^{(b)}$, and so we notate both parameters as λ in this case. The same is true for the base equilibrium lengths, meaning we further simplify notation by writing $r_0 := r_0^{(a)} = r_0^{(b)}$. We non-dimensionalise n by introducing $s(n) := \frac{n}{N}$ where N is the total number of segments of a filament. This can be interpreted as a discrete non-dimensionalised arc-length. We write $s = s(n)$ for clarity, where $s \in \left\{ \frac{1}{N}, \frac{2}{N}, \dots, \frac{N-1}{N}, 1 \right\}$.

Unless stated otherwise, we use the following parameters.

Parameter	Numerical Value
$\lambda = \lambda^{(a)} = \lambda^{(b)}$	6.82
$k^{(a)}$	1
$k^{(b)}$	1
$k^{(c)}$	10
$r_0 = r_0^{(a)} = r_0^{(b)}$	5.46
$r_0^{(c)}$	5

Table 3.1: Standard geometrical and forcing parameters for axoneme model.

Note that r_0 and $r_0^{(c)}$ are set to the natural choice: $r_0 = \sqrt{D_f^2 + D^2}$ is the distance between two segments connected by a cross-link when the model is in its initial position, and $r_0^{(c)} = D_f$ is the initial horizontal distance between two adjacent segments connected by a cross-link. Furthermore, instead of the amplitude λ we later instead consider the ratio $\lambda_s = \frac{L}{\lambda}$, loosely giving a measure of how close the length scale of the undulation perpendicular to direction of motion is to the filament length.

3.2.6 Parameters for Filament Model

The filament model which we use to model this 2D representation, detailed in Section 2.3, relies on certain parameters which are important to understand in the context of our 2D representation. The numerical values are given in the table below to three significant figures where necessary.

Parameter	Interpretation	Numerical Value
N	Number of segments per filament	31
a	Segment radius, i.e. half-filament width	1
δ	Length/Segment scale	2.20
D	Distance between adjacent segment centres	2.20
D_f	Distance between two filaments	5
L	Length of individual filament	68.2
w	Weight per unit length	1
B	Elasto-gravitational constant	1000
K_B	Bending modulus	0.0682
T	Steps per unit time	600
R	Number of repetitions of unit time	1

Table 3.2: Standard parameters for filament model.

The number of segments N was chosen after initial experimentation to allow for sufficient detail in both simple bending motion and for more complex wave propagations in individual filaments. The distance between adjacent segment centres is defined as $D = \delta a$. The length of the filament L is defined as $L = ND$. D_f is the distance between the two filaments in the model, corresponding to $r_0^{(c)}$. The bending modulus K_B , introduced in Section 2.2.1, measures the ratio of stress to strain forces in the bending deformation of the filament. Here, $K_B := \frac{wL^3}{B}$, such that w is the weight per unit length and B is the elasto-gravitational constant. In the absence of gravity, the constant B is only relevant in this model for the calculation of the bending modulus. Finally, the filament model will run with $T = 600$ individual steps per unit time, and unless stated otherwise all simulations consist of a single repetition $R = 1$ of the unit time, giving a total of T time steps.

3.2.7 Justification

The cross-links defined here aim to fulfill the role of active motor dynein proteins which generate internal forces. In reality, dyneins attached to one microtubule reach over and attach themselves to adjacent microtubules. A beat is generated through the regular attachment and detachment of dyneins along with the motion of the nexin links and radial spokes. The cross-links modelled here loosely apply the principles of the *dynein cross-bridge cycle* model and the *geometric clutch control* model, as discussed in Section 1.2. The former is due to the fact that the links representing dynein attachments attach and detach according to a cycle, and that the beat cycle is the direct outcome of the cross-links (Lindemann & Lesich 2010). This is fused with the assumption of geometric clutch models that the distance between microtubule pairs is responsible for the activation of dynein motors. The ‘activation’ in our model can be thought of as the switching in direction of forces due to changes in cross-link lengths.

The biological mechanisms take place in three dimensional space, however a two dimensional model such as this one can accurately capture the beating patterns and behaviour (Camalet & Jülicher 2000, Riedel-Kruse et al. 2007). The only notable models in this field that use multiple filaments coupled with length-dependent forces in order to instigate bending in a composite body is in Han & Peskin (2018) and Elgeti et al. (2010). However our model differs from Han & Peskin (2018) in that it will not use a dynamical law in order to generate tension in the cross-links, instead relying entirely on geometric information and internal clocks, and our model differs from Elgeti et al. (2010) in that inter-filament cross-link lengths are varied instead of inter-segment lengths of the same filament in order to generate bending.

3.3 Bending Dynamics

In order to instigate bending, the inner driving force functions defined in Section 3.2.4 need to be set accordingly. First, we look at how a non-time-dependent set-up can cause bending towards an equilibrium position. This is done by setting the following for the inner driving force functions,

$$f^{(a)}(s, t) = s, \quad (3.15)$$

$$f^{(b)}(s, t) = 1 - s. \quad (3.16)$$

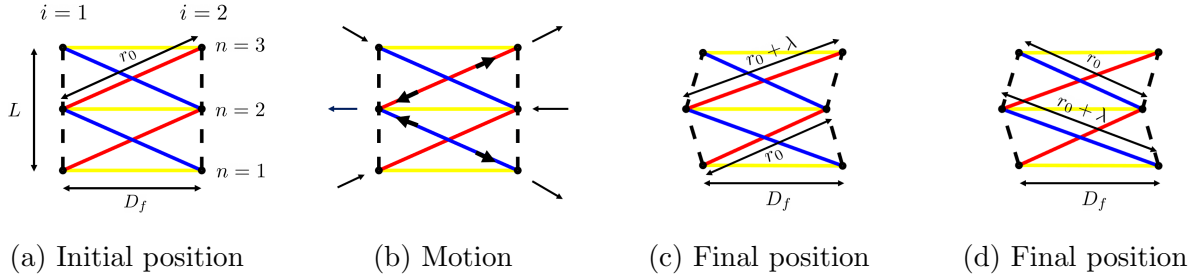


Figure 3.2: Bending Dynamics of Axoneme Model

Now, we investigate the consequences of introducing this pair of functions into our model.

3.3.1 Theoretical Understanding

For this first example, we will first consider the forces driving the filaments in the model analytically to demonstrate the behaviour that the computational model produces. We consider a simplified version in which $N = 3$, $L = 1$, and momentarily disregard hydrodynamic forces. We also assume $s \in \{0, 1\}$, instead of $s \in \{\frac{1}{2}, 1\}$, for simplicity. This is visualised in Figure 3.2a. Our governing equations for the equilibrium lengths are as follows, removing time-dependent notation where appropriate,

$$\begin{aligned} r_{1,2}^{(a)} &= r_0, & r_{2,1}^{(b)} &= r_0 + \lambda, \\ r_{2,3}^{(a)} &= r_0 + \lambda, & r_{3,2}^{(b)} &= r_0. \end{aligned} \quad (3.17)$$

This means that the equilibrium lengths for the red cross-links increase along arc-length, and decrease for the blue cross-links along arc-length. These equilibrium lengths are time independent, with the only time-dependent information available being the distance between two cross-linked segments. Therefore in the initial position the forces generated by the cross-links defined in Equation 3.10 repel or contract the connecting segments, prescribing the system to settle into the equilibrium lengths. In our simple case, this means that only one connector for each set of cross-links is prescribing a non-zero force at the initial time. The amplitude, λ , is greater than zero, meaning that these connectors have a higher equilibrium length than the initial length, causing the segments to repel each other, as seen in Figure 3.2b. The system then settles into its equilibrium position when all forces are balanced, i.e. when equilibrium positions have been attained. Figures 3.2c and 3.2d shows the final lengths of the red and blue cross-links respectively.

Finally, including the yellow horizontal stiff springs in Figure 3.1 preserves the overall structure of the body, in particular the horizontal distance between the left and right filaments. The spring constant $k^{(c)}$ is an order of magnitude higher than those for the cross-link forces, slightly biasing the system to prioritise structure over severe bending. In the simple example, these are the reason for which the composite body bends to the right as the middle horizontal link is preserving the distance between the middle segments of each filament. These horizontal springs also prevent the elongated links in reaching their full equilibrium length depending on how the spring constants are scaled, meaning that the labels for the diagonal distances in Figures 3.2c and 3.2d are larger than they would be with activated yellow links.

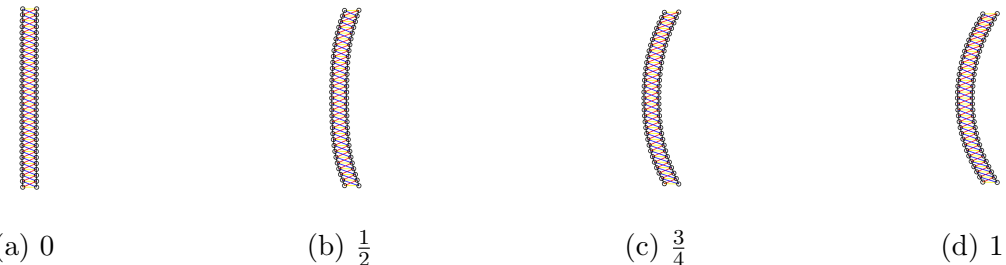


Figure 3.3: Bending Dynamics of Axoneme Model, Computational Result

3.3.2 Computational Demonstration

Now, we observe the motion of the filaments as produced by our full model, with the results in Figure 3.3, indexed by proportion of time taken to get to the equilibrium position. This computational demonstration follows our theoretical understanding and intuition, with the only addition being a displacement in centre of mass, i.e. the centre of mass of the body moves to the left due to hydrodynamic forces. As the filament on the right bends, work is done on the fluid. Explicitly, the upper segment pushes fluid downwards as it moves right and down, and the lowest segment pushes fluid upwards as it moves right and up. This would result in a flow of fluid from left to right, displacing the centre of mass.

3.4 Swimmer Model

In order to instigate swimming of the composite body, instead of simply having the body reach an equilibrium state, we introduce a wave propagation into the inner driving force functions $f^{(a)}(s, t)$ and $f^{(b)}(s, t)$. This is due to the fact that other individual-filament swimmer models often prescribe motion by sending a travelling wave through the filament (Saggiorato et al. (2017), Schoeller & Keaveny (2018)), and as discussed in Section 1.1 helical and planar wave propagations are prevalent in nature. As in this framework we do not have direct control on the curvatures of the individual filaments, we instead need to propagate waves by prescribing forces in the cross-links which will transfer to producing a waveform in the composite body. This is done by adding a time and length-dependent wave propagation to the equilibrium lengths of the cross-links.

In this section we visualise the motion of each swimmer by plotting the centreline motion of its head. These diagrams non-dimensionalise the distance travelled by reporting the proportion of the swimmer length L travelled. We also show the swimming motion over one full undulation cycle. Further visualisations can be found in Appendix E.

3.4.1 Asymmetric Swimmer

Here we outline the first attempt at modelling a swimmer, also introducing the necessary notation for the finalised model and other examples. We set the following for our inner driving force functions,

$$f^{(a)}(s, t) = \beta(s) \sin(\Phi(s, t)), \quad (3.18)$$

$$f^{(b)}(s, t) \equiv 0, \quad (3.19)$$

with the following wave propagation,

$$\Phi(s, t) = ks - \omega t + \phi, \quad (3.20)$$

such that the parameters k , ω and ϕ in the wave propagation are defined below along with additional controls as in Table 3.3, given to three decimal places where necessary.

Parameter	Interpretation	Numerical Value
$\beta(s)$	Beating amplitude scaling	1
k_s	Wavenumber	1.466 ¹
k	Angular wavenumber	9.213
γ	Undulations per unit time	5
T_{und}	Steps per undulation cycle	120
ω	Undulation frequency	0.0524
ϕ	Phase	0

Table 3.3: Parameters for wave propagation.

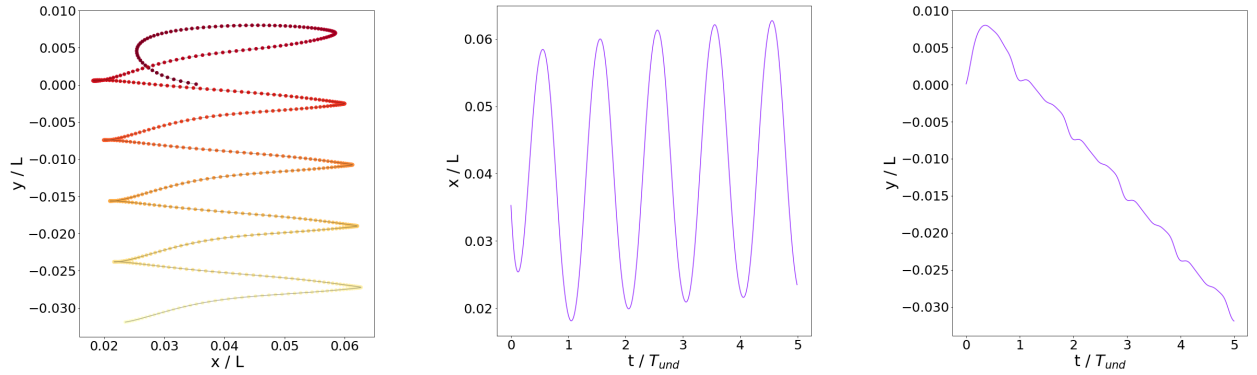
$\beta(s)$ varies the driving force amplitude λ for different sections of the swimmer body, which in this case is set to 1 but which may be arc-length dependent. The wavenumber k_s is approximately the number of complete wavelengths along a filament at any point in time, and the angular wavenumber is defined as $k = 2\pi k_s$. γ corresponds to the number of undulations the model completes over T time steps. Therefore $T_{\text{und}} = \frac{T}{\gamma}$ provides the number of steps taken for each cycle of undulation, and the undulation frequency $\omega = \frac{2\pi\gamma}{T}$ converts this frequency to radians. Finally, ϕ displaces the wave propagation by a fixed amount.

The motion of the centreline of the *head*, that is to say the average of the coordinates for the first segment of each filament, is visualised in Figure 3.4a. The motion of the swimmer in x and y directions can be seen in Figure 3.4b and 3.4c. The motion of the swimmer moving downwards over one undulation cycle with time period T_{und} is also shown in Figure 3.5, notating the start of the cycle as 0 and the end as T_{und} .

This first model demonstrates the capability of the hydrodynamic solver described in Schoeller et al. (2019a) to simulate microswimmers that are constructed according to the model described here. Figure 3.4a clearly displays the undulatory motion of the head swinging side to side as the travelling wave propagates down the length of the swimmer. There is a non-constant overall velocity in the direction of travel as shown by 3.4c, and the head follows a path closer to a saw tooth than a travelling sine wave. Finally, the travel is asymmetric, and the swimmer clearly drifts off in one direction instead of travelling in a straight line, with further experiments in which the running time of the simulation was extended indicating that the swimmer follows a circular trajectory. This reveals that the model may hold similarities to the circular gaits modelled in other studies such as Gong et al. (2019).

Note at the start of the simulation, shown by the darker nodes in Figure 3.4a, there is an apparent *settling time* where the swimmer has not achieved the standard locomotion it

¹This choice for the wavenumber is precisely $\frac{100}{L}$, which is a result of previous code which defined k_s differently. Originally, s was dimensional such that $s \in \{0, L\}$, of course requiring a non-dimensionalisation factor of $\frac{1}{L}$ in the wavenumber. Later on, s was changed to be non-dimensional such that $s \in \{0, 1\}$, but the factor of $\frac{1}{L}$ remained. It was decided to keep this initial choice for consistency, though a more sensible choice would be $k_s = 1.5$, representing exactly one and a half wavelengths along the length of the swimmer.



(a) Head motion, dark to light as time increases.

(b) Centreline x position of head over time.(c) Centreline y position of head over time.

Figure 3.4: Motion of Asymmetric Swimmer

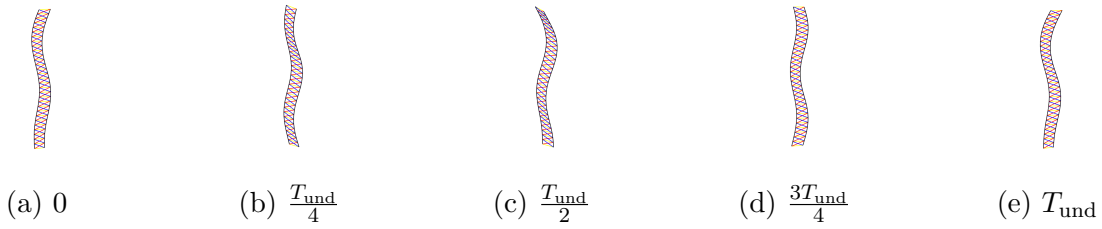


Figure 3.5: Undulation Cycle of Asymmetric Swimmer

follows later in the simulation. This is due to the fact that at the first time instance the two filaments are completely straight, and filaments require a period of time to deform into the curvature that the internal cross-link forces determine, and after this point the deformations that occur are smoother.

3.4.2 Symmetric Swimmer

In order to produce a spatially symmetric swimmer, both sets of driving forces in the cross-links need to oscillate in a complementary manner. This is done by adjusting the internal driving force functions,

$$f^{(a)}(s, t) = \beta(s) \sin(\Phi(s, t)), \quad (3.21)$$

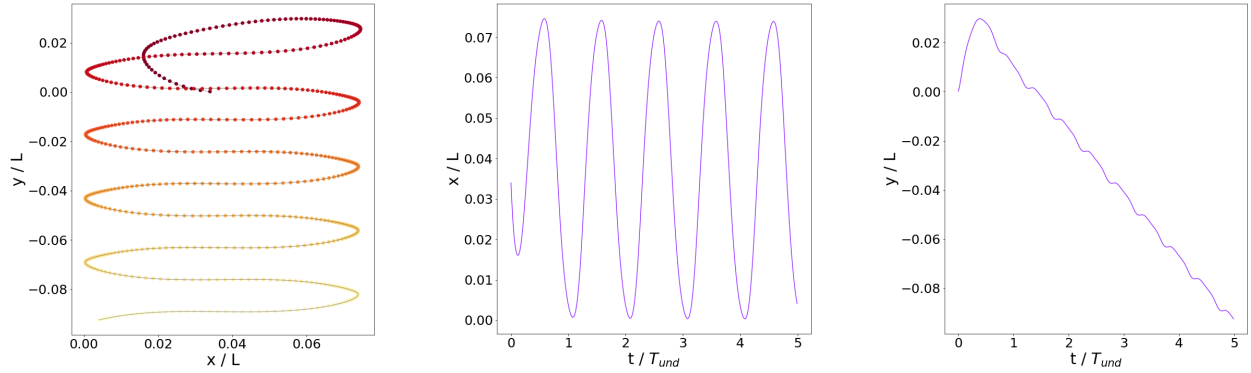
$$f^{(b)}(s, t) = \beta(s) \sin(\Phi(s, t) + \pi), \quad (3.22)$$

with the standard wave propagation,

$$\Phi(s, t) = ks - \omega t + \phi, \quad (3.23)$$

using the same parameters as in Table 3.3. This set up produces a spatially symmetric swimmer, due to the fact that for any level n and any point in time t , the sum of equilibrium lengths in Equations (3.12) and (3.13) is constant. The motion of the head of the centreline can be seen in Figure 3.6.

This model improves upon the previous two by removing spatial asymmetry from the system, ensuring that the centreline of the head follows a symmetrical travelling wave during undulation. Figure 3.6c also shows that there is less variation in velocity in the direction of



(a) Head motion, dark to light as time increases.

(b) Centreline x position of head over time.(c) Centreline y position of head over time.

Figure 3.6: Motion of Symmetric Swimmer

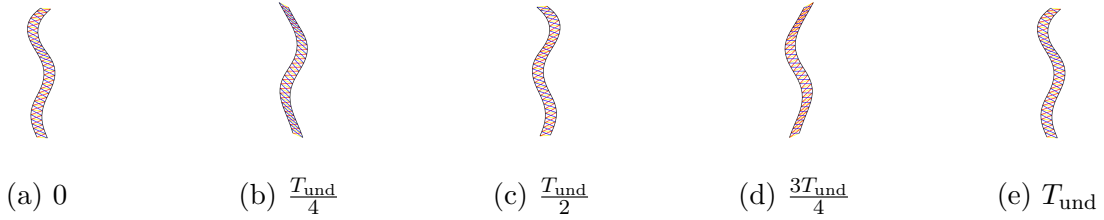


Figure 3.7: Undulation Cycle of Symmetric Swimmer

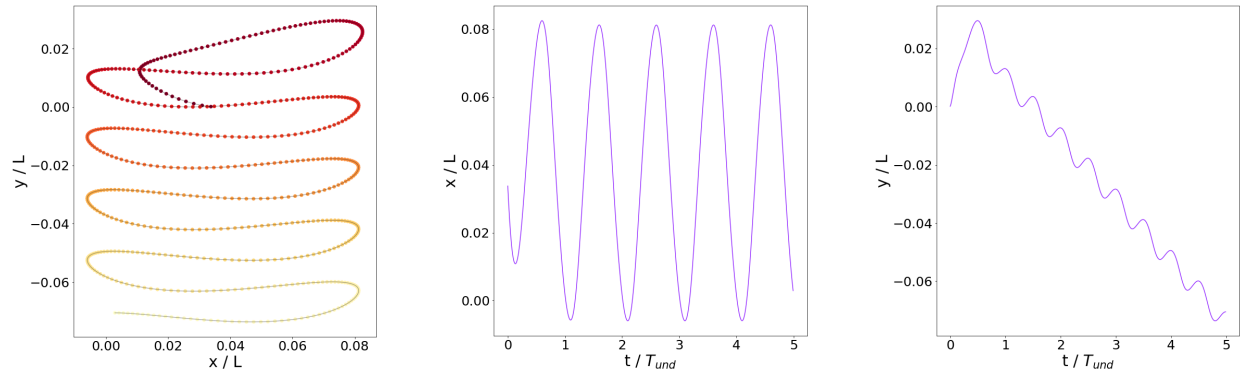
travel, however a reduction in speed in the negative y -direction still occurs as the swimmer switches direction of undulation. This swimmer also swims much faster than all previous models, swimming a distance over 8% of the length of the body, compared to 3% for the asymmetric swimmer. This signals that this model is more efficient, as the internal driving forces are the same for both models yet the symmetric swimmer moves further away from the origin. We come back to concepts of efficiency in Section 3.5. Now, we make one final adjustment to the swimmer in the following example.

3.4.3 Final Swimmer

One parameter which has not been fully used in the previous examples is $\beta(s)$, which can be used to vary the beating amplitude along the length of the filaments by controlling the level of internal forcing selectively. In our final model, we use the exact set up as in the previous example seen in Section 3.4.2, but now the beating amplitude decays linearly with respect to the arc-length, i.e. internal forcing decreases closer to the tip. This single alteration is achieved by setting $\beta(s)$ in the internal forcing functions given in Equation (3.21) as the following,

$$\beta(s) = \begin{cases} 1, & \text{if } 0 \leq s \leq \frac{1}{2}, \\ 2(1-s), & \text{if } \frac{1}{2} < s \leq 1. \end{cases} \quad (3.24)$$

The choice of this linear decay in the beating amplitude is motivated by similar assumptions seen in models for motile cilia (Han & Peskin 2018) and ram sperm (Schoeller & Keaveny 2018). In particular for the cilia model in Han & Peskin (2018), the motivational model discussed previously, $\beta(s)$ plays the same role as the level-dependent constant K_k for the



(a) Head motion, dark to light as time increases.

(b) Centreline x position of head over time.

(c) Centreline y position of head over time.

Figure 3.8: Motion of Swimmer, Final Model

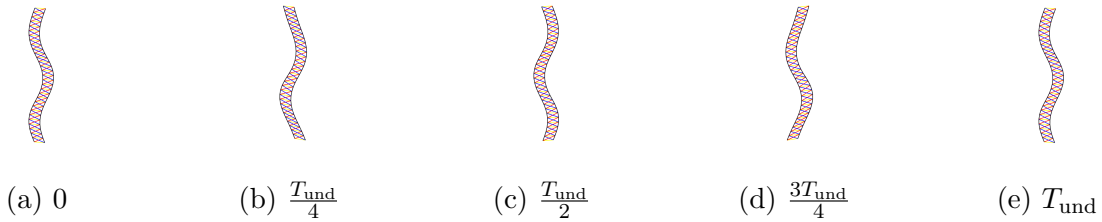
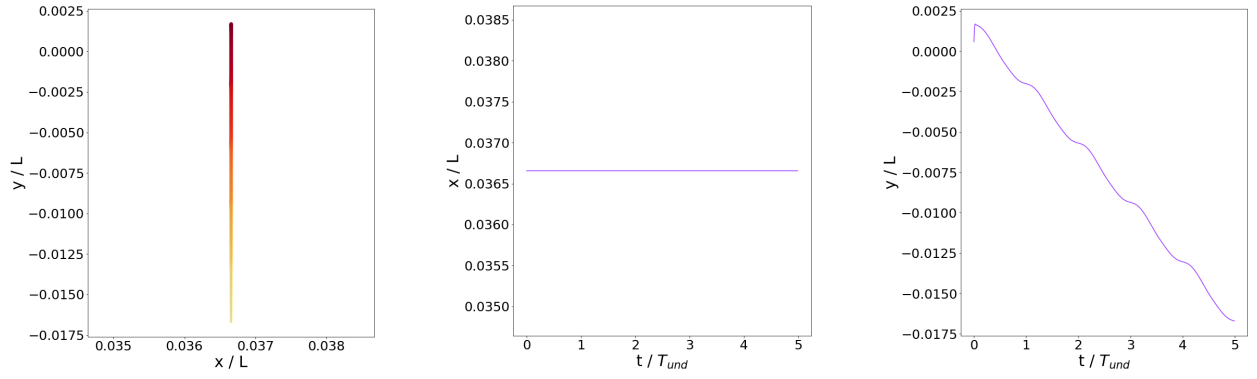


Figure 3.9: Undulation Cycle of Swimmer, Final Model

inner forcing represented by Equation (3.1). Han & Peskin (2018) justify this by stating that closer to the cell body there is less ATP available to dynein motors, resulting in a diminished energy source in the tip which leads to a decrease in flagellar motion from head to tail. Simply, in the context of sperm motility, the cell body refers to the head and so a higher availability of energy closer to the head of the sperm produces greater undulation nearer the head than the tail. See Appendix A.2.3 for an example where we explore the limitations in attempting to achieve more nuanced biological accuracy, and Section 4.1 in Chapter 4 for a deep dive into possibilities relating to tail variations introduced by Equation (3.28).

The resulting model produces significant qualitative differences to the symmetric swimmer in the previous example, with more circular wave forms being traced out by the head which results in more variation in the velocity in direction of travel. The decreased mobility in the tail can be clearly seen in Figure 3.9 as the swimmer moves downwards. Figure 3.8c compared to Figure 3.6c also shows that variation of velocity in the y -direction oscillates much more smoothly than for the symmetric swimmer. The swimmer is also marginally slower than the symmetric swimmer, swimming a total of just over 6% of the length of the body over 5 undulation cycles. Despite being marginally slower than the previous swimmer in Section 3.4.2, this is the swimmer model we use in Section 3.5 for evaluations according to energy and efficiency measurements. This means we retain some biological nuance in the model. In Chapter 4, in which we model more complex environments such as collective motion, we use the simpler swimmer defined in Section 3.4.2 instead.



(a) Head motion, dark to light as time increases.

(b) Centreline x position of head over time.(c) Centreline y position of head over time.

Figure 3.10: Motion of Non-Undulatory Swimmer

3.4.4 Non-Undulatory Swimmer

Now that we have refined the model, before moving onto evaluating the model we note that this framework can also produce non-undulatory swimmers. We explore this here, as a short detour, to show the versatility of the model. Despite our model being originally built with undulatory swimmers in mind, this allows us to gain a deeper understanding of what exactly the equilibrium-varying functions defined above are doing in the model. For example, we can set the following functions for varying the internal driving forces generated by the cross-links,

$$f^{(a)}(s, t) = f^{(b)}(s, t) = \beta(s) \sin(\Phi(s, t)), \quad (3.25)$$

where $\Phi(s, t)$ is as in Equation (3.23), with all the same parameters as in Table 3.3 for the symmetric swimmer, with an exaggerated amplitude of $\lambda = 11.4$. The resulting locomotion is completely different from the undulatory motions seen in the swimmers we have been considering. The centreline of the body remains completely stable with no variation perpendicular to the direction of travel. Movement is achieved through the propagation of circular contractions and expansions along the diameter of the body, a motion known as peristalsis. The clear candidate for the organism that this model represents are certain types of mites such as the *Gordialycus* discussed in Section 1.1, which uses moving zones of contractions as seen in this model. The motion of this model may be closer to that of the earthworm due to the radial contractions, though the earthworm does not live in Low-Reynolds number flow. Finally we also note that this swimmer is slower than all three undulatory swimmers, swimming a distance of under 2% of its body length over 5 undulation cycles despite the exaggerated amplitude λ , indicating a non-optimised mode of swimming in this context.

Interestingly, we also note that Juhász & Zelei (2013) model worm-like motion in a remarkably similar fashion to this model, by simulating artificial muscles internally which contract and expand through the use of torsional springs which have a periodic control function attached to them.

3.5 Optimisation

In this section we will perform data analysis on the swimmer model in order to investigate how small variations in parameters change the locomotion of the swimmer. We evaluate

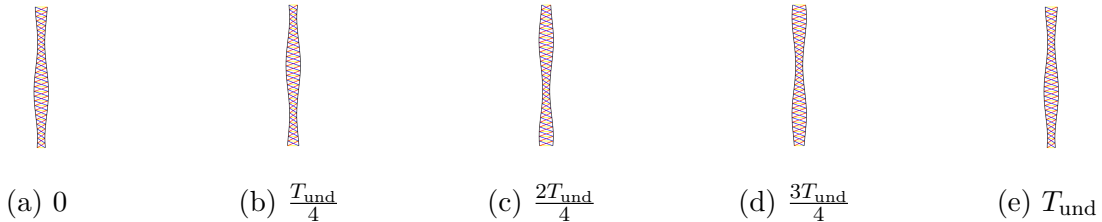


Figure 3.11: Undulation Cycle of Non-Undulatory Swimmer

changes in behaviour through observations of the following characteristics of the model: displacement, viscous dissipation, hydrodynamic efficiency, and centre-of-mass velocity.

3.5.1 Model Selection

Our final model is the model in Section 3.4.3, which we briefly recap here. We use the following functions for driving the internal forcing mechanisms,

$$f^{(a)}(s, t) = \beta(s) \sin(\Phi(s, t)), \quad (3.26)$$

$$f^{(b)}(s, t) = \beta(s) \sin(\Phi(s, t) + \pi), \quad (3.27)$$

with the following wave propagation and linear decay in internal forcing respectively

$$\Phi(s, t) = ks - \omega t + \phi, \quad (3.28)$$

$$\beta(s) = \begin{cases} 1, & \text{if } 0 \leq s \leq \frac{1}{2} \\ 2(1-s), & \text{if } \frac{1}{2} < s \leq 1. \end{cases} \quad (3.29)$$

Wave propagation parameters are kept the same as for the previous models, shown in Table 3.4, with the exception of the wavenumber $k_s = \frac{k}{2\pi}$ which will be varied in the parameter search.

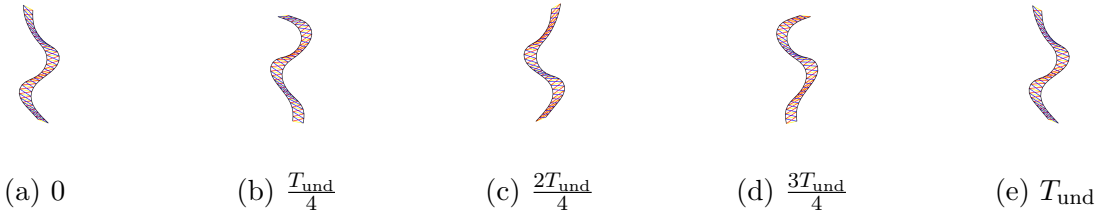
Parameter	Interpretation	Numerical Value
γ	Undulations per unit time	5
T_{und}	Steps per undulation cycle	120
ω	Undulation frequency	0.0524
ϕ	Phase	0

Table 3.4: Parameters for wave propagation, final model.

Filament model parameters such as the steps per unit time T , number of segments per filament N and bending modulus K_B are kept as in Table 3.2. Cross-link parameters such as spring force constants $k^{(\Xi)}$ and characteristic equilibrium lengths $r_0^{(\Xi)}$ are kept as in Table 3.1, with the exception of the amplitude $\lambda = \lambda^{(a)} = \lambda^{(b)}$ which will be varied in the parameter search.

3.5.2 Parameters

In this analysis, we explore the effects of two parameters: the amplitude of the inner forcing defined by λ , and the wavenumber defined by k_s . In order to investigate the amplitude, we instead investigate the characteristic amplitude ratio defined as $\lambda_s = \frac{L}{\lambda}$, which tells us how

Figure 3.12: Undulation Cycle of Symmetric Swimmer, Small λ_s

close the variation in the x -direction gets to the length of the filament². Specifically, λ_s can be thought of as the ratio of the filament length to the beating amplitude. For example, if $\lambda_s = 8$, then the undulation in the x -direction will be 10 times smaller than the length of the filament. Therefore, decreasing λ_s will decrease the difference length of the swimmer and the length of movement perpendicular to swimmer. The effects of decreasing this ratio can be seen in Figure 3.12. Intuition allows us to confidently make the prediction that a swimmer will swim further if the differences between these length scales is minimised, as it will allow for more aggressive undulation. Therefore, we expect that a smaller ratio λ_s will lead to a faster swimmer.

Table 3.5 gives the standard parameters for each variable when the other is varied in the following experiments. For simplicity, we assume independence of the parameters and perform a search where one is varied while the other is fixed, with later experiments instead using a full grid search.

Parameter	Interpretation	Numerical Value
k_s	Wavenumber	1.466
λ_s	Characteristic Amplitude Ratio	25

Table 3.5: Standard numerical values for parameters.

3.5.3 Displacement

This analysis provides an exploration into the variation of the displacement of the swimmer when the wavenumber k_s and the ratio λ_s are varied.

Parameter Selection

First with fixed $\lambda_s = 25$, wavenumber k_s is increased from $k_s = 0.0733$ to $k_s = 2.199$ with a step size of 0.0733³, additionally including the base case of $k_s = 0$. Initial experiments found that increasing k_s beyond $k_s = 2.2$ provided limited additional change in behaviour. These represent a range of having under a tenth of a total wavelength along the filament to having just over 2. The base case of $k_s = 0$ was chosen as in this case the wave propagation is entirely determined by the undulation frequency ω and time t , removing dependence on arc-length s . Then with fixed wavenumber $k_s = 1.466$, λ_s is increased from $\lambda_s = 10$ to $\lambda_s = 80$ with a step size of 5. Decreasing λ_s below 10 revealed computational challenges

²This is motivated by considering an ideal scenario in which the distance D between adjacent segments of the same filament is small compared to the distance between the two filaments D_f . Then $r_0 + \lambda$ is approximately the maximum distance a cross-link achieves in the x -direction.

³These choices are a consequence of previous code, with $\frac{5}{L} \approx 0.0733$ and $\frac{150}{L} \approx 2.199$.

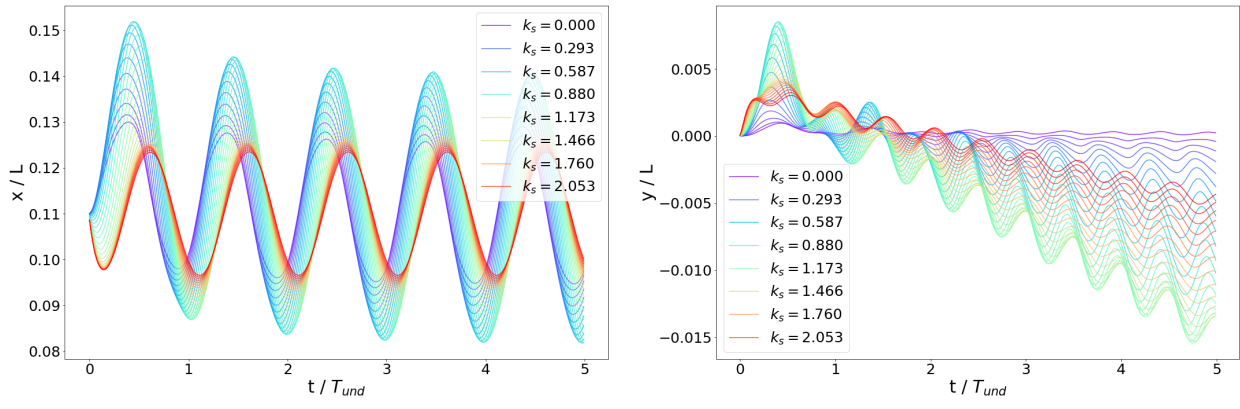
(a) Centreline x position of head over time.(b) Centreline y position of head over time

Figure 3.13: Motion of Swimmer, Varying Wavenumber

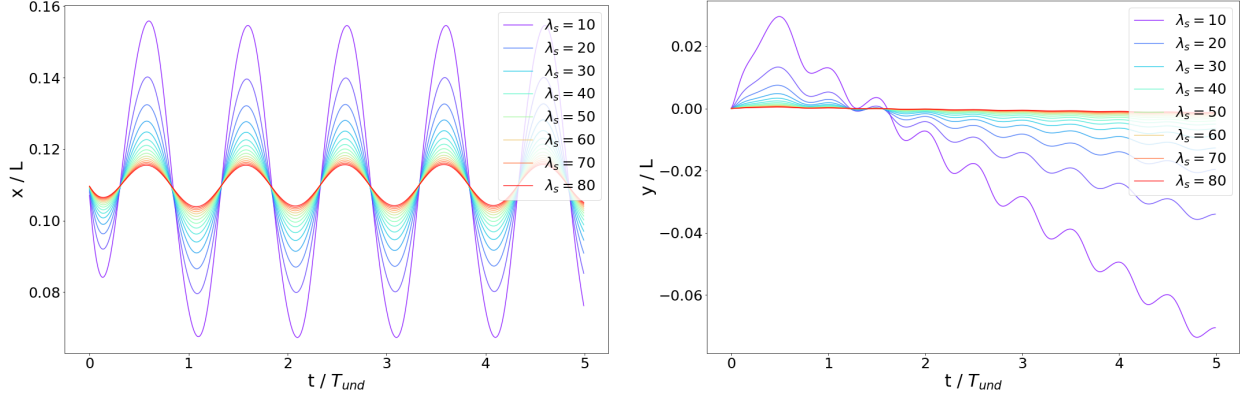
(a) Centreline x position of head over time.(b) Centreline y position of head over time.

Figure 3.14: Motion of Swimmer, Varying Characteristic Amplitude Ratio

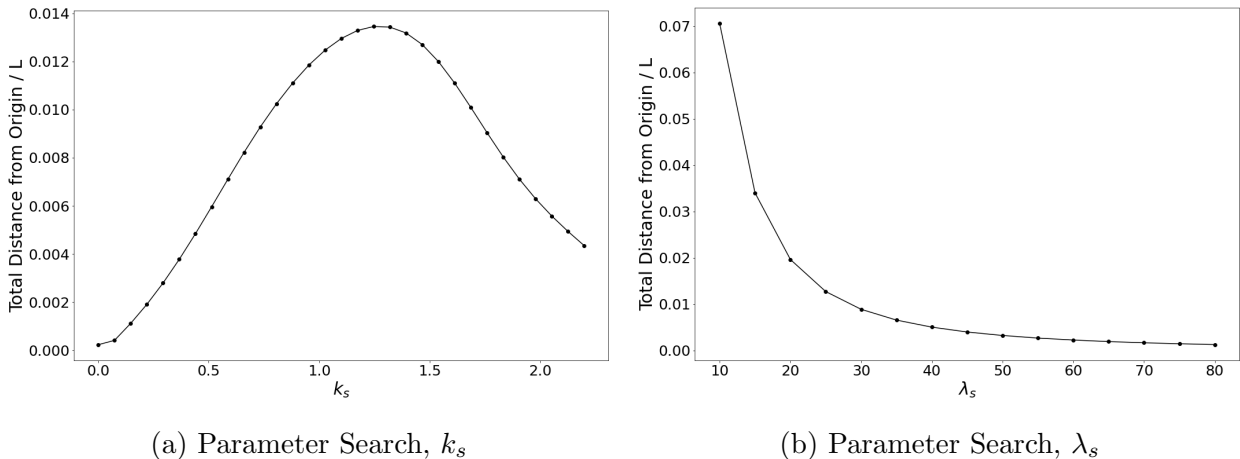
(a) Parameter Search, k_s (b) Parameter Search, λ_s

Figure 3.15: Motion of Swimmer, Final Distance from Origin

due to comparatively extremely aggressive undulation. Furthermore, increasing λ_s above 80 provided limited additional change in behaviour.

Results

The effects of varying the wavenumber can be seen in Figure 3.13. Firstly, we see the period of the undulation in the x -direction increases with the wavenumber. The relationship between the wavenumber and maximum final distance from the origin can be seen in Figure 3.15a, with the peak occurring at $k_s \approx 1.246$, which also coincides with the maximum in peaks of undulation in the x direction in Figure 3.13a.

The effects of varying the amplitude ratio can be seen in Figure 3.14. The behaviour of the body under variation of this parameter is simpler, with a decreased ratio λ_s resulting in further distance travelled in the y direction with a greater undulation amplitude in the x direction, referring to the peaks in the x -direction. The final distance travelled does not appear to follow a linear relationship, with the final distance from the origin increasing faster as the ratio λ_s gets smaller. As expected, a smaller ratio results in more aggressive undulation due to the equilibrium lengths of the cross-links achieving higher peaks during the wave propagation. Furthermore note that Figure 3.14a shows the periodicity of undulation in the x direction is constant with respect to λ_s . Figures 3.15a and 3.15b also show that λ_s has a greater effect on the distance travelled, and therefore the speed, than k_s .

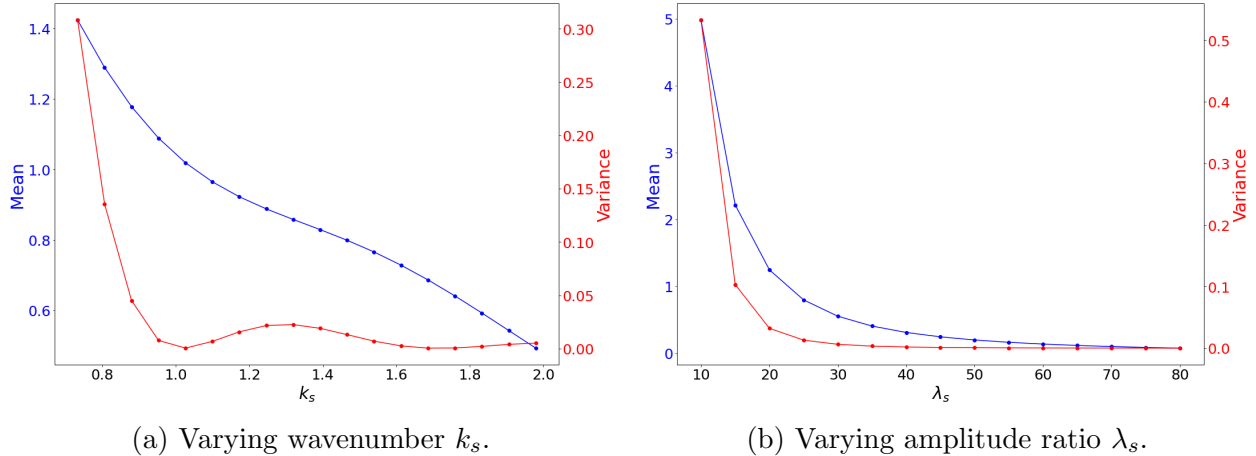
All parameter searches reveal a *settling time*, i.e. the time taken for the swimmer to reach a periodic motion. As discussed when initially defining the model, this is due to the swimmer starting in the straight configuration, followed by the forces prescribing the body into the wave form before a periodic swimming can properly commence. This is clearest in Figure 3.14b, with non-periodic behaviour during the first undulation cycle. During this time there is also a sharp rise in y position as the head of the swimmer is moved upwards in the initial forcing. Notably, the different swimmers appear to have a similar settling time in the sense that they return to the origin at similar times. Again this is clearest in Figure 3.14b, where after approximately one undulation cycle all of the swimmers' heads have returned to and then moved below the origin.

3.5.4 Viscous Dissipation

After investigating the displacements of different versions of our final swimmer, more numerical measurements are required in order to understand the energy each individual swimmer is using up as it travels. We define the viscous dissipation of the total composite body of the swimmer in the following way,

$$\text{Viscous Dissipation, } D(t) = \sum_{i=1}^2 \sum_{j=1}^N (\mathbf{F}_{i,j}(t) \cdot \mathbf{u}_{i,j}(t) + \mathbf{T}_{i,j}(t) \cdot \boldsymbol{\Omega}_{i,j}(t)), \quad (3.30)$$

such that at time t for segment j of filament i , $\mathbf{F}_{i,j}(t)$ is the total force that the segment exerts onto the fluid, $\mathbf{u}_{i,j}(t)$ is the instantaneous velocity of the segment, $\mathbf{T}_{i,j}(t)$ is the torque exerted by the segment onto the fluid, and $\boldsymbol{\Omega}_{i,j}(t)$ is the instantaneous angular velocity. Note that the torques and angular velocities only act in the z direction out of the plane, meaning

Figure 3.16: Viscous Dissipation of Swimmer, Mean and Variance over $t \in [0.2T, T]$

that we can rewrite them in the following way

$$\mathbf{T}_{i,j}(t) = \begin{pmatrix} 0 \\ 0 \\ T_{i,j}(t) \end{pmatrix}, \quad \boldsymbol{\Omega}_{i,j}(t) = \begin{pmatrix} 0 \\ 0 \\ \Omega_{i,j}(t) \end{pmatrix}, \quad (3.31)$$

for scalars $T_{i,j}(t)$ and $\Omega_{i,j}(t)$. Similarly for the forces and velocities,

$$\mathbf{F}_{i,j}(t) = \begin{pmatrix} \mathbf{F}_{i,j}(t) \cdot \hat{\mathbf{x}} \\ \mathbf{F}_{i,j}(t) \cdot \hat{\mathbf{y}} \\ 0 \end{pmatrix}, \quad \mathbf{u}_{i,j}(t) = \begin{pmatrix} \mathbf{u}_{i,j}(t) \cdot \hat{\mathbf{x}} \\ \mathbf{u}_{i,j}(t) \cdot \hat{\mathbf{y}} \\ 0 \end{pmatrix}. \quad (3.32)$$

This gives a measure for the change in effective work done by the composite body against the fluid as it swims, and a similar notion of viscous dissipation was also used by Spagnolie & Lauga (2010) for evaluating optimal elastic swimmers.

Parameter Selection

As above, we perform a parameter search to observe the behaviour of the swimmer with respect to work done over a range of parameters. First the wavenumber k_s is increased from $k_s = 0.0733$ to $k_s = 1.979$ with a step size of 0.0733^4 , with fixed $\lambda_s = 25$. Then, the amplitude ratio λ_s is increased from $\lambda_s = 10$ to $\lambda_s = 80$ with a step size of 5, and a fixed wavenumber $k_s = 1.466$.

Results

Figure 3.17 displays how work done evolves over time for the range of models. In the initial settling time of the swimmer, the swimmer expends a comparatively large amount of energy moving the filaments into the preferred instantaneous positions for swimming due to the inner driving forces. Consistent changes in the behaviour can be seen for variation of the amplitude, with a decrease in both variance and average work done as λ_s is decreased. This is intuitive, as a smaller ratio directly contributes to greater forcing against the fluid. Figure 3.17 also shows that variance changes less consistently when varying k_s , despite increased k_s leading to higher average work done in general. We also see a non-linear variation in

⁴ $50 \approx 0.733L, 135 \approx 1.979L, 5 \approx 0.0733L$

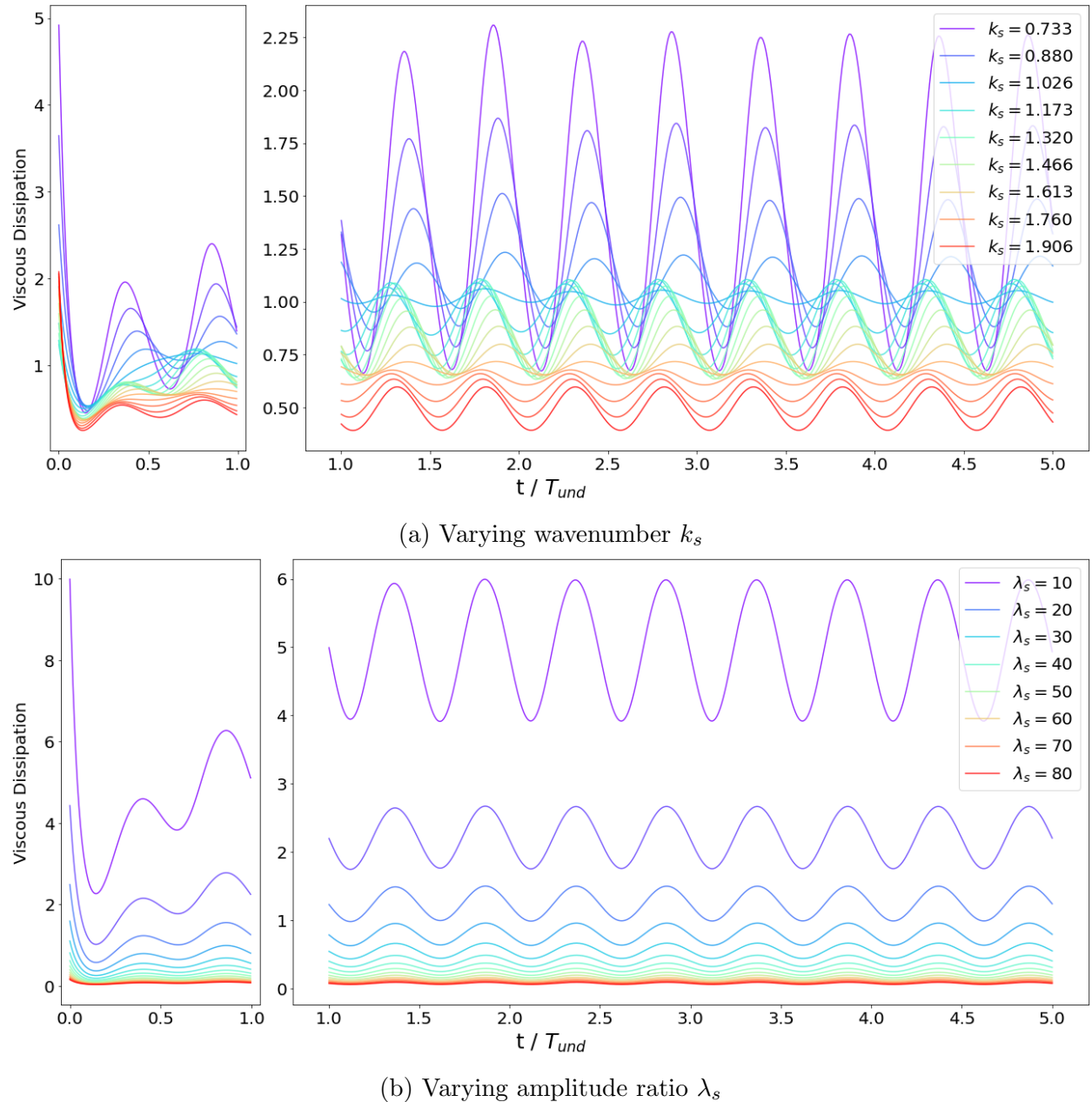


Figure 3.17: Viscous Dissipation of Swimmer over Time

the periodicity of work done when the wavenumber varies, which matches the variations in undulation periodicities in both the x and y directions seen previously. In Figure 3.16a, we see that despite an initial decrease in variance as k_s is increased from 0 to a whole wavelength, there is a local maximum variance where the total wavelength is approximately one and a third of the length of the swimmer body. These figures can be used to evaluate how much energy the swimmer is expending in order to move, however this can be made more intuitive by scaling the average work done according to how quickly the body is moving. This will be developed in the next section as a measure of efficiency.

3.5.5 Hydrodynamic Efficiency

In order to evaluate how our swimmers are using up their energy we use a measure of hydrodynamic efficiency η . We consider the same measurement of efficiency used by Majmudar et al. (2012) for the evaluation of models of the nematode *Caenorhabditis elegans* in a complex environment, defined in the following way,

$$\text{Hydrodynamic Efficiency, } \eta_m = \frac{\mu L (u_m)^2}{D_m}. \quad (3.33)$$

η_m is the hydrodynamic efficiency at an index m , with m signifying the start of a cycle of undulation. We use the term ‘cycle m ’ to signify the period of time which contains the full m^{th} cycle of undulation, with m ranging over all undulations⁵. u_m is the velocity of the centre of mass averaged over cycle m . Similarly, D_m is the viscous dissipation averaged over cycle m . μ is the viscosity of the fluid, which is fixed at $\mu = 1$ in the filament model. L is the length of an individual filament in the composite swimmer model, and so is set to $L = 68.2$.

The velocity of an individual swimmer at cycle m , u_m , is calculated as follows in a similar manner to the definition seen in Kamal & Keaveny (2018). Firstly, the instantaneous centre of mass velocity is defined for time t as,

$$\mathbf{u}(t) = \frac{1}{2N} \sum_{i=1}^2 \sum_{j=1}^N \mathbf{u}_{i,j}(t), \quad (3.34)$$

such that $\mathbf{u}_{i,j}$ is the velocity of segment j of filament i . Then for some cycle $m \geq 0$, we take the average of all the velocities $\mathbf{u}(t)$ that fall within the range of the undulation cycle, i.e. such that the time step t is in the range $t \in [mT_{\text{und}}, (m+1)T_{\text{und}}]$, to get the period-averaged velocity,

$$\mathbf{u}_m = \frac{1}{T_{\text{und}}} \sum_{t=mT_{\text{und}}}^{t=(m+1)T_{\text{und}}} \mathbf{u}(t), \quad (3.35)$$

keeping in mind our discrete space-time system. Then, we define u_m simply as the magnitude of \mathbf{u}_m . Unlike in Kamal & Keaveny (2018), orientation due to $\hat{\mathbf{t}}$, the unit vector tangent to an individual filament, is disregarded due to the increased computational time. Similarly, the viscous dissipation at the m^{th} cycle is calculated as,

$$D_m = \frac{1}{T_{\text{und}}} \sum_{t=mT_{\text{und}}}^{t=(m+1)T_{\text{und}}} D(t). \quad (3.36)$$

⁵In our case we have $m \in \{0, 1, \dots, \gamma - 1\}$, such that $\gamma = \frac{T}{T_{\text{und}}} = 5$.

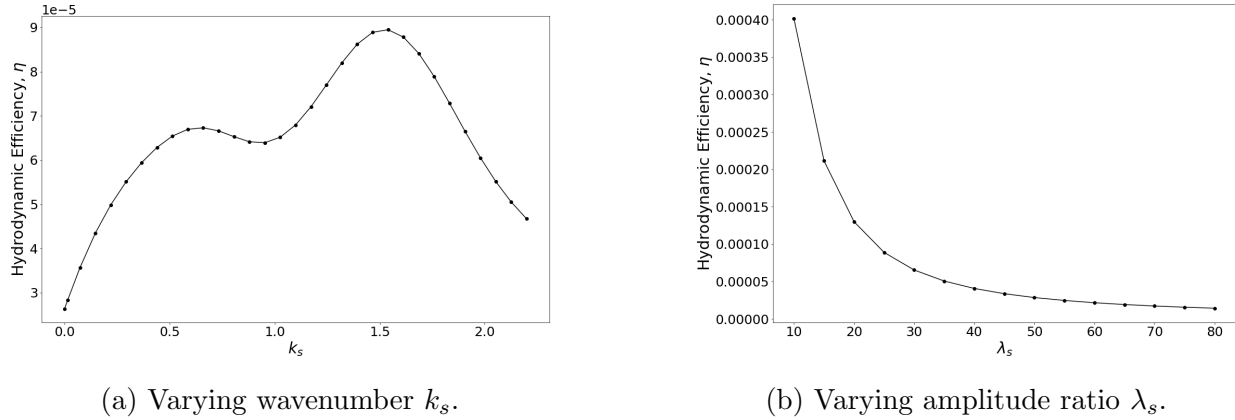


Figure 3.18: Hydrodynamic Efficiency of Swimmer

In later examples we are concerned with the evolution of velocity over time, which is the reason for which the period-averaged velocity and viscous dissipation are defined in this way. However presently we are not interested in the evolution of efficiencies over time, and instead seek one efficiency to associate to each model. Therefore, in this section we calculate,

$$\eta = \langle \eta_m \rangle_T, \quad (3.37)$$

such that η is the efficiency over an entire simulation run of T time steps. Note that in practice for independent undisturbed swimmers, $\eta = \eta_m = \langle \eta_m \rangle_T$ due to each undulation cycle being identical. This is not the case for environments with multiple swimmers, for example.

Parameter Selection

As above, we perform a parameter search to observe the behaviour of the swimmer with respect to work done over a range of parameters. We use the exact same range of parameters and step size for k_s and λ_s as in the displacement analysis in Section 3.5.3.

Results

The results from this experiment produced a clear outcome when varying each of the two parameters. For the amplitude ratio, maximum and minimum efficiencies of 0.04014% and 0.00143% resulted from $\lambda_s = 10$ and $\lambda_s = 80$ respectively. For the wavenumber, maximum and minimum efficiencies of 0.00895% and 0.00264% resulted from $k_s = 1.540$ and $k_s = 0$ respectively. Despite overall being small, the measurement of hydrodynamic efficiency allows us to make comparisons between the variants of the model.

For amplitude ratio, the dependence on λ_s of the hydrodynamic efficiency follows the exact same trend as seen in viscous dissipation in Figure 3.16b, and final distance from origin in Figure 3.15b. It is clear that the additional velocity is worth the great increase in internal driving force when the ratio λ_s between length of the body and the undulation perpendicular to the body is decreased. The minimum and maximum efficiencies seen above represent a 2709.800% increase from the least efficient to the most efficient model. This clearly signals an extreme change in how energy is being used up to propel the swimmer forward compared to energy lost in the internal forcing. However, we must bear in mind that the minimum

efficiency results from a swimmer that is barely moving due to the extremely small beating amplitude.

For wavenumber, Figure 3.18a shows that the maximum efficiency occurs for approximately one and a half wavelengths, with a local minimum at one complete wavelength. The effect of the wavenumber of efficiency is important with a 240% increase from minimum to maximum efficiency. This is less important than the effect of amplitude, which has a percentage change an order of magnitude higher. Furthermore, we also note that the minima and maxima of the efficiencies occur near half-integer wavenumbers. This initial finding is consistent with the observation of a bias towards half-integer wavenumbers by Spagnolie & Lauga (2010).

These efficiencies are smaller than those reported for some existing single-filament models. For example, Spagnolie & Lauga (2010) reports a hydrodynamic efficiency of approximately 6% for finite-length flagellum, comparing this to an efficiency of approximately 1% demonstrated by biological cells which use planar waves to swim. There are many reasons for which the efficiencies for our models may be lower than existing models. For example, as discussed in Appendix A.2.3, the length scales used may not be sufficient for efficient swimming. As the length of the filament L is not much larger than the distance between the filaments, this means that the amount of work done perpendicular to the swimmer body is comparable to the work done in direction of travel. A simple observation⁶ of the swimmer movement shows that the displacement is very small despite the high level of variation in the inner cross-links, leading to low efficiency. However, the measure of hydrodynamic efficiency is sufficient for the purposes used here of making comparisons between variants of our model.

3.5.6 Final Optimisation

For our final experiment, we run a finer grid search over λ_s and k_s to optimise our model using the hydrodynamic efficiency η to evaluate each model. Wavenumber k_s is varied within the range of $k_s = 1.34$ to $k_s = 1.56$ with a step size of 0.02, and λ_s is varied within the range of $\lambda_s = 8$ to $\lambda_s = 26$ with a step size of 2, therefore testing a total of 110 variants of the model. These parameters were chosen due to the indications of the previous experiment that the optimal swimmers had wavenumbers within the range of 1.35 to 1.55, and small amplitude ratios. Initial experiments were ran to confirm that the maximum efficiencies for each λ_s had corresponding wavenumber within the range given. Resultant time-averaged velocities for swimmers are also presented for comparison.

Results

The optimal swimmer had parameters $\lambda_s = 8$ and $k_s = 1.38$, with a hydrodynamic efficiency of 0.0545% and an average velocity of 0.00804. This experiment also revealed other notable behaviours of the models. Firstly, the graphs again show the relative importance of the amplitude compared to the wavenumber, regarding both velocity and efficiency. Secondly, Figure 3.19b shows that, within the range of parameters considered, the best swimmers with sufficiently small amplitude ratios⁷ will always swim fastest with a wavenumber $k_s = 1.34$, though this may change if the grid search were to be expanded to include wavenumbers $k_s < 1.34$. Thirdly, Figure 3.19a shows that the wavenumber k_s of the most efficient swimmer is dependent on its amplitude, with a linear relationship between k_s and λ_s for $8 \leq \lambda_s \leq 18$.

⁶Representative frames of examples in Appendix E. Videos can be found on the author's GitHub.

⁷i.e. $\lambda_s \leq 16$

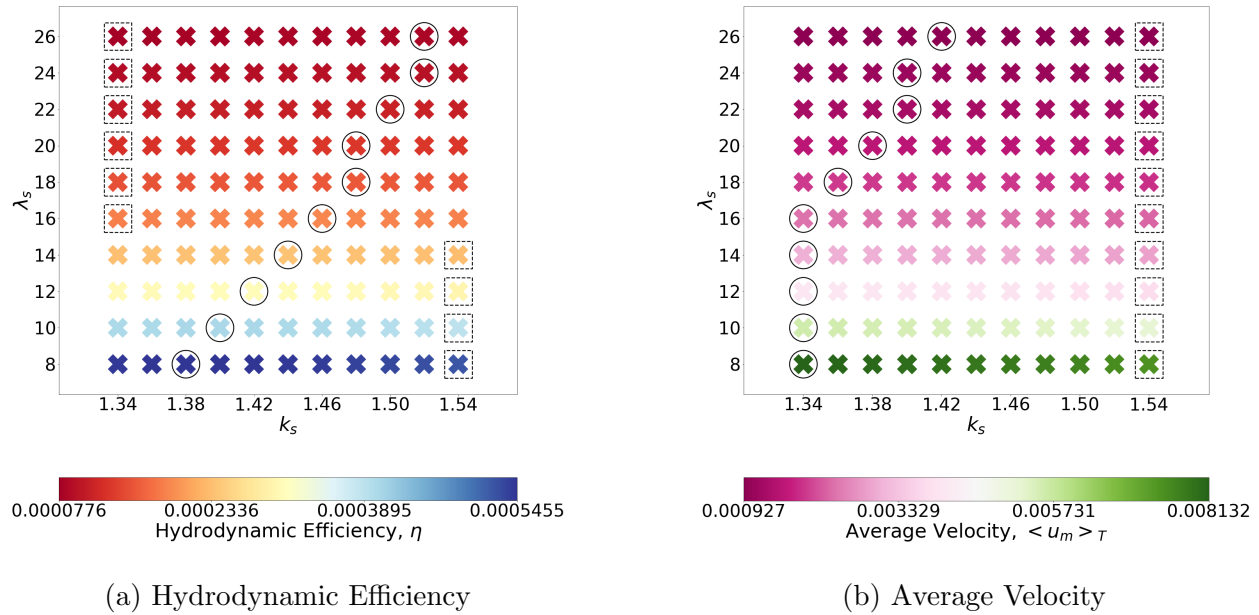


Figure 3.19: Grid Search over (k_s, λ_s) . For each row (λ_s) a circle gives the highest value and a dotted square gives the lowest value.

Interestingly past this point, when the ratio is increased such that $\lambda_s > 16$, we also see that the fastest swimmers no longer have wavenumber $k_s = 1.34$. Within the range considered, $\lambda_s = 16$ appears to be a critical value at which the relationship between the wavenumber and amplitude ratio changes with respect to efficiency and velocity. Finally, the two figures also show that for fixed λ_s , the choice of k_s giving the most efficient swimmer does not coincide with the choice of k_s giving the fastest swimmer.

3.6 Conclusion

In this chapter we presented a novel approach to modelling the axoneme for microswimmers in Stokes Flow, inter-connecting individual filaments modelled using the Kirchhoff rod model with additional mechanisms for simulating the behaviour of active dynein motor proteins. To investigate the parameters of the model, a parameter search was completed on the wavenumber and amplitude ratio, using displacement, viscous dissipation and hydrodynamic efficiency as optimisation parameters. Our final experiment revealed how wavenumber and amplitude ratio profoundly change the efficiency of the swimmer, with the optimal choice of wavenumber being dependent on the amplitude ratio. Now that this model has been outlined and tested, in the next chapter we employ the techniques developed here to develop further versions of the model in more complicated systems inspired by biological environments.

Chapter 4

Further Biological and Environmental Modelling

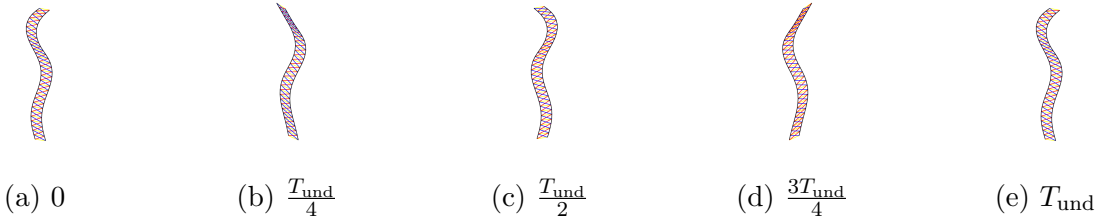
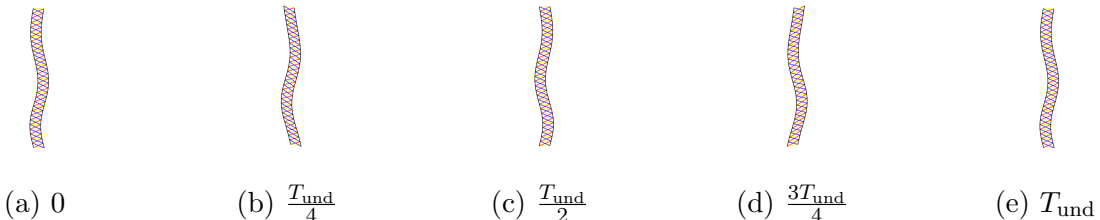
A key question for mathematicians and biologists is how more complicated biological and environmental factors influence the overarching behaviour of individual swimmers and coordination of groups of swimmers. For example, in the motivating paper for this thesis, Han & Peskin (2018) are mainly concerned with how motile cilia can spontaneously synchronise on large-scales through the small-scale mechanisms that occur in each individual cilia. In a different context, Fu & Powers (2007) study how viscoelasticity influences the swimming speed and direction of sperm, motivated by a need to understand the non-Newtonian fluid dynamics of the female reproductive tract which is essential for understanding fertility complications in humans. With these and numerous other studies in mind, this chapter aims to examine how more complicated environmental and biological influences can affect the swimming motion of the models defined in this thesis. In particular we investigate if more nuanced modelling of tails can result in more optimal swimming and if the model can be scaled to observe collective motion.

4.1 Variations in Tail Beating

In Chapter 3, our swimmers incorporated the following linear decay for the inner forcing mechanisms that drive the beating amplitude,

$$\beta(s) = \begin{cases} 1, & \text{if } 0 \leq s \leq \frac{1}{2}, \\ 2(1-s), & \text{if } \frac{1}{2} < s \leq 1. \end{cases} \quad (4.1)$$

Biological research indicates a more complex range of movement in sperm cells. Lindemann & Lesich (2016) detail counterbend formation in mammalian sperm, extreme bending in the midpiece of mouse sperm near the head, and extremely asymmetric behaviour near the basal connecting piece. Rikmenspeol (1978) observes higher amplitudes in the tails of hinged and free bull sperm compared to their heads, behaviour not effectively captured by mathematical modelling completed at the time. Visual imaging by Ounjai et al. (2012) demonstrate the extreme bending that takes place at the mid-piece of the spermatozoa tail nearer the head, rather than at the principal and tail pieces which make up the majority of the swimmer body.

Figure 4.1: Undulation Cycle of Tail-Driven Swimmer ($\beta_A = 2, \zeta = \frac{1}{6}$)Figure 4.2: Undulation Cycle of Head-Driven Swimmer ($\beta_A = \frac{1}{16}, \zeta = \frac{1}{5}$)

In an attempt to explore these complex relationships, using our framework we can implement a generalisation of the linear decay $\beta(s)$ used in Section 3.5, to determine how more complex tail beating can change the efficiencies and velocities of the swimmer. We do this by defining $\beta(s)$ in the following way¹,

$$\beta(s) = \begin{cases} 1, & \text{if } 0 \leq s \leq \zeta \\ \frac{1}{1-\zeta} (\beta_A(s - \zeta) + 1 - s), & \text{of } \zeta < s \leq 1. \end{cases} \quad (4.2)$$

This prescribes greater or weaker internal forcing in the tail, for $\beta_A > 1$ and $\beta_A < 1$ respectively. The *tail* is defined to start at $s = \zeta < 1$. Explicitly, β_A controls the increase in the internal forcing, such that from $s = \zeta$ to $s = 1$ the amplitude λ increases linearly from λ to $\beta_A \lambda$. For example, if $\zeta = \frac{1}{2}$ and $\beta_A = \frac{1}{3}$, then from the middle of the swimmer to the tip, the internal forcing decreases by a factor of three. If $\zeta = \frac{1}{6}$ and $\beta_A = 2$, then over the latter five sixths of the body the internal forcing amplitude increases by a factor of two. This latter example can be seen in Figure 4.1. Intuitively, $\beta_A < 1$ will result in decreased movement in the tail of the swimmers, and $\beta_A > 1$ will result in increased movement in the tail of the swimmers. Therefore, $\beta_A < 1$ will result in a head-driven swimmer, $\beta_A > 1$ in a tail-driven swimmer. ζ controls where the tail begins, or can be thought of as the proportion of the body that the head takes up. Therefore the extreme cases are $\zeta = 0$, which gives a swimmer that is only tail, and $\zeta = 1$, giving a swimmer that has no tail at all such that $\beta(s) = 1$ for all s .

4.1.1 Initial Grid Search

Model and Parameter Selection

All parameters are kept as in the standard model used in Section 3.5, with wavenumber and amplitude ratio such that² $k_s = 1.45$ and $\lambda_s = 15$. The only alteration is of course defining

¹Note that we obtain the swimmer used in Chapter 3 by choosing $\zeta = \frac{1}{2}$ and $\beta_A = 0$.

²This combination was chosen to coincide with the optimal swimmers determined in Section 3.5.6, however noting the relationship between λ_s and k_s for optimal swimmers likely only holds for the original model such that $\zeta = \frac{1}{2}, \beta_A = 0$.

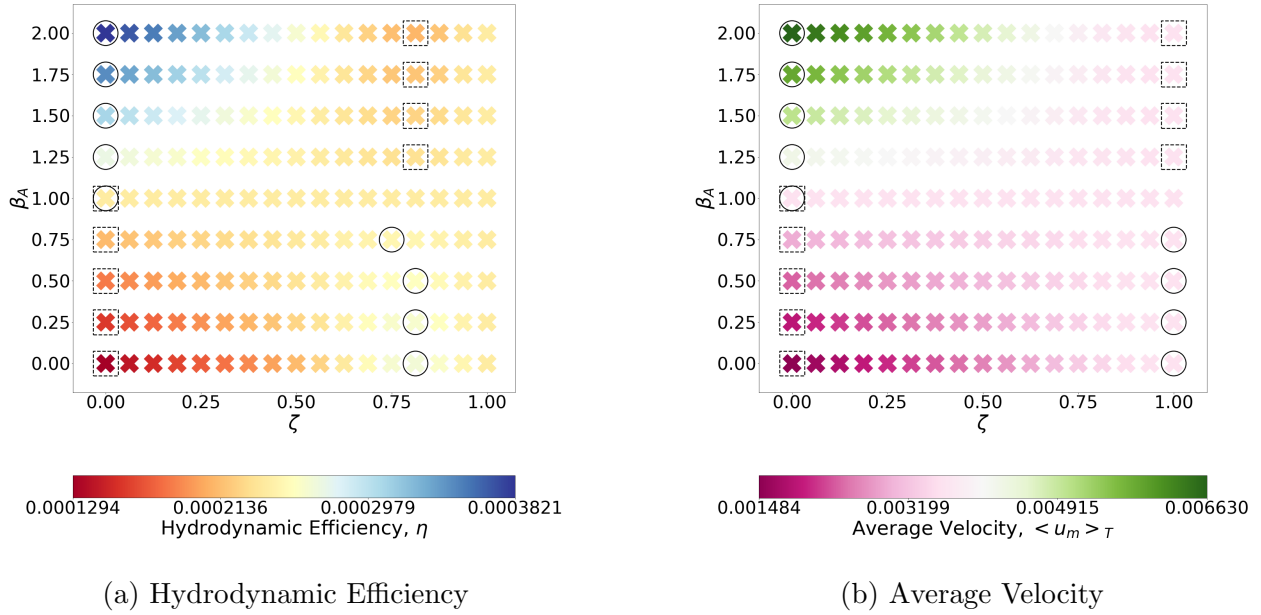


Figure 4.3: Grid Search over (ζ, β_A) . For each row (β_A) a circle gives the highest value and a dotted square gives the lowest value.

$\beta(s)$, which is a multiplicative factor on λ_s , being defined as above in Equation (4.2). We run a grid search with ζ and β_A as our inputs and hydrodynamic efficiency and velocity as our outputs. ζ is varied from 0 to 1 with a step-size of 0.0625, and β_A is varied from 0 to 2 with a step size of 0.25, therefore testing a total of 153 variants of the model.

Results

The grid search over β_A and ζ first showed that for tail-driven swimmers such that $\beta_A > 1$, the most efficient and fastest swimmers come from setting $\zeta = 0$. This means that if amplitude increases along the tail, then the swimmer benefits from having this increase occur along the whole length of the body. We can deduce that tail-driven swimmers simply benefit from having as large an inner forcing as possible, with a distinction between the tail and the head not benefiting the swimmer either in velocity or efficiency. So if the internal forcing is going to increase instead of decrease, it is best if it increases along as much of the body as possible.

For head-driven swimmers such that $\beta_A < 1$, the situation is more nuanced. The results clearly show that for $0 < \beta_A < 0.5$, the optimal swimmer results from $\zeta = 0.8125$, meaning that having the tail begin approximately $\frac{4}{5}$ along the length of the body results in the most efficient use of energy. Note that the optimal swimmers in this case do not coincide with the fastest swimmers, which are the swimmers with no tail at all such that $\zeta = 1$, seen in Figure 4.3b. Therefore, having a small tail approximately a fifth of the total body length results in the most effective use of energy despite not giving the fastest swimmers. We clarify this also holds for $\frac{1}{2} < \beta_A < 1$ in a finer grid search in Section 4.1.2. For $\beta_A > 1$, this trend is reversed, with head-driven swimmers with a tail that starts approximately $\frac{4}{5}$ along the length of the body being the least efficient for a given value of β_A . Similarly, the least efficient head-driven swimmers are also not the slowest swimmers, with the slowest swimmers instead being those with no tail at all.

This experiment showed a more nuanced relationship between the two variables than that

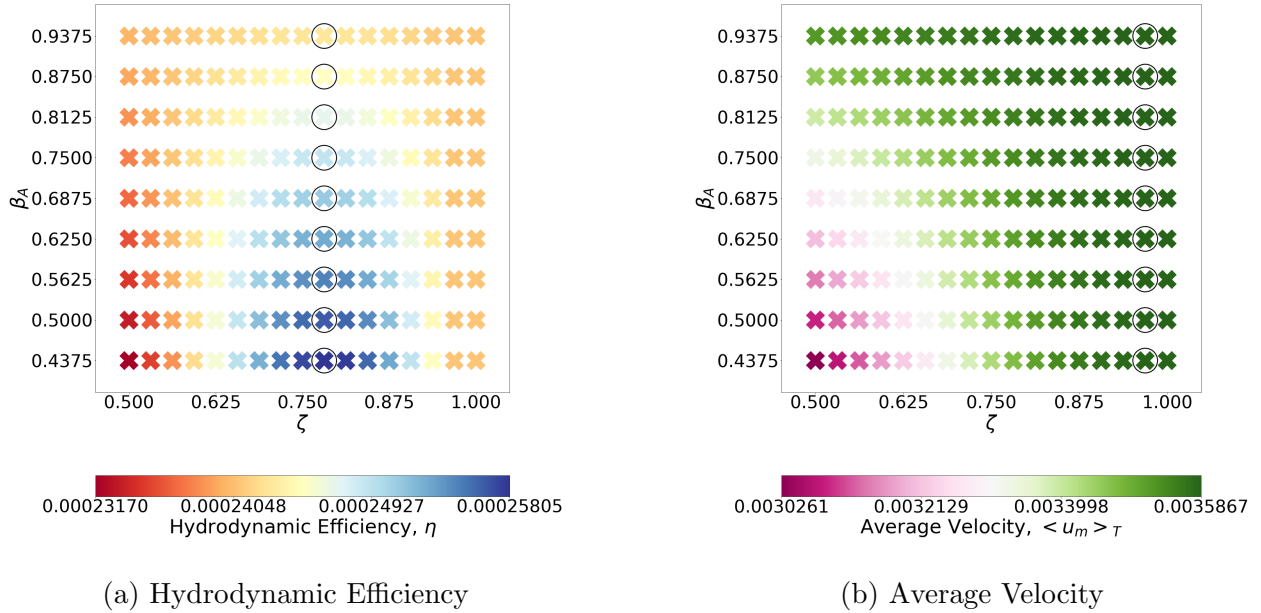


Figure 4.4: Fine Grid Search over (ζ, β_A) . For each row (β_A) a circle gives the highest value.

seen between λ_s and k_s previously. We can see that unlike λ_s , increasing β_A for any value of ζ will not always result in a more efficient or faster swimmer, shown by the roughly diagonal lines of consistent efficiency for both velocity and efficiency. Secondly, both parameters are of equal importance at this level of fineness, with a small variation in either resulting similar variations in efficiency, whereas earlier we saw that λ_s was much more important than k_s . There is also a duality between $\beta_A < 1$ and $\beta_A > 1$, with the best and worst choices of ζ nearly exactly reversed in terms of both velocity and efficiency.

4.1.2 Finer Grid Search for Head-Driven Swimmers

Due to the less clear outcome for head-driven swimmers within the range $\frac{1}{2} < \beta_A < 1$, we run a finer grid search on the bottom right quarter of the grids in Figure 4.3, with the goal of clarifying what tail size is optimal for swimmers with a weak³ decay in tail beating.

Model and Parameter Selection

The same base model used in the initial grid search in Section 4.1.1 is used here, with $k_s = 1.45$ and $\lambda_s = 15$. We again run a grid search over ζ and β_A with hydrodynamic efficiency and velocity as outputs. β_A is varied from 0.4375 to 0.9375 with a step size of 0.0625, only considering the range of β_A where behaviour is not already clear from the initial search. Initial experiments showed that the maximum values of hydrodynamic efficiency for each β_A lied within the range 0.5 to 1, and so ζ is varied from 0.5 to 1 with a step-size of 0.03125. This evenly splits the range for β_A and ζ into 17 and 9 possibilities each, producing 153 variants of the model. The signalling of minimum outputs for each β_A with dotted squares as done previously is omitted.

Results

Firstly, Figure 4.4a confirms the key finding of the initial grid search, namely that for any head-driven swimmer such that $\beta_A < 1$, the optimal case results from $\zeta \approx \frac{4}{5}$. To this level of fineness, we can precisely determine that $\zeta = 0.78125$ gives the optimal swimmer for any value of $\beta_A < 1$, and further degrees of accuracy would require a finer discretisation of our model given that each filament is made up of 31 segments. The contour mapped out by Figure 4.4a demonstrates that efficiency has an increased sensitivity to ζ as β_A decreases, with the least and most efficient variants both occurring when $\beta_A = 0.4375$ for different values of ζ , which is intuitive given the role the two parameters play. Furthermore, Figure 4.4b confirms that the optimal head-driven swimmers are not the fastest, with the fastest cases resulting from a very small tail such that $\zeta = 0.96875$, instead of $\zeta = 1$ as determined by the coarser parameter search.

Here we have obtained strong evidence for the optimal length of tails regarding efficiency and velocity for this type of swimmer. A key take away from both grid searches in this section is that the simple linear decay used in Chapter 3, in which $\beta_A = 0$ and $\zeta = \frac{1}{2}$, is not an optimal modification to the model. In fact, within the range of the second parameter search, this is the second worst case in terms of efficiency and the third slowest. Including a tail decay at all results in a slower and less efficient swimmer, and if a swimmer is head-driven, then the tail needs to be shorter and only take up a fifth of the total body to produce the most efficient case.

4.2 Multiple Swimmers

In the final section of this thesis, we examine how multiple swimmers in the same environment can influence locomotion, motivated by numerous studies demonstrating the profound effects on fluid flows generated by multiple swimmer interactions. For example, in an experimental investigation, Fisher et al. (2014) demonstrate that as cluster sizes of rodent sperm increase so does the swimming speed, with this advantage diminishing with larger group sizes, of approximately 7 and over, due to the geometry of the swimmers. Differences are also shown between average aggregate sizes for sperm from different species that evolve under different types of competition. Furthermore, Brumley et al. (2014) experimentally demonstrate that *Volvox carteri* cells, a species of green alga, synchronise robustly despite differences in intrinsic beating frequencies. The flagella of these cells were also shown to be able to synchronise for movement in opposite directions as well as in the same direction depending on orientations, and the lack of biochemical interactions firmly showed that two flagella can synchronise solely through the changes in fluid flow around them. Studies such as these are the primary motivation for the experiments carried out in this section, with the goal of observing whether the models built in this thesis capture the behaviour of other models in previous theoretical and experimental work.

4.2.1 Model Selection

Unless stated otherwise, the model we use is as outlined in Section 3.4.3, a standard symmetric swimmer without amplitude variation along arc-length with the parameters of $\lambda_s = 10$

³We can think of $0 < \beta_A < \frac{1}{2}$ as a strong decay in beating across the tail, and $\frac{1}{2} < \beta_A < 1$ as a weak decay in beating across the tail.

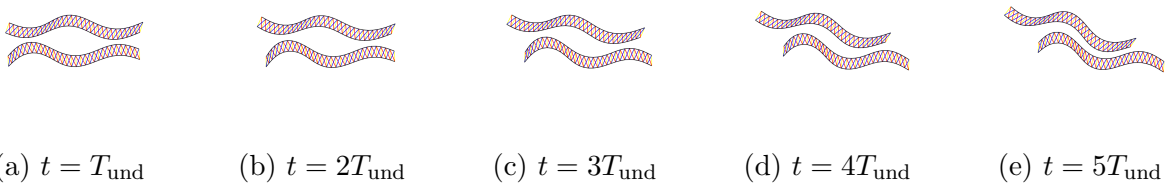


Figure 4.5: Synchronisation of Swimmers with a Phase Difference $\Delta\phi = \pi - \varepsilon$

and $k_s = 1.466$. Due to the findings of Section 4.1, we use this variant where the swimmers have no decay in beating amplitude, instead of the model used for Section 3.5. The measurements we consider include velocities, viscous dissipation, and hydrodynamic efficiency. Finally, in Chapter 3 the steps per unit time $T = 600$ was deemed to be sufficient for individual swimmers, however this parameter is increased in the experiments here with the justification being that more steps per unit time lowers the difference between each time step, allowing for more complicated movement to be captured.

4.2.2 Synchronisation of Out-of-Phase Swimmers

A question recently developed in the literature is that of synchronisation. Here we develop some experiments to see whether identical swimmers that are out of phase exhibit synchronisation tendencies. We say that two swimmers are out of phase if they have differing values of ϕ in the standard wave propagation equation $\Phi(s, t)$ regulating the inner driving forces.

Experiment

The only modifications we make to the standard simulation is increasing the steps per unit time to $T = 1800$ due to the more subtle changes in interactions, and we introduce $R = 10$ repetitions of the unit time period T to observe long-term behaviour. The parameter of interest in this experiment is the phase ϕ in the wave-propagation equation first defined in Section 3.4.1. We consider two swimmers positioned side-by-side, with the only difference being that their wave propagations are out of phase, with a phase difference of $\phi_1 - \phi_2 = \Delta\phi$. We consider three cases: $\Delta\phi = \pi$, $\Delta\phi = \pi - \varepsilon$ for some small $\varepsilon > 0$, and $\Delta\phi = \frac{\pi}{2}$. See Figures E.13, E.14, and E.15 in Appendix E for complete visualisations.

Results

Firstly, we discover that two swimmers swimming parallel which are exactly out of phase, such that $\Delta\phi = \pi$, do not synchronise. The symmetrical hydrodynamic forces separating the swimmers keeps them in the same stable motion without shifting for phase-locking. For the case with a small disturbance to the symmetrical phase-difference such that $\Delta\phi = \pi - \varepsilon$ for some small $\varepsilon > 0$, we see in Figure 4.5 that the spatial disturbance leads to a displacement. Unlike the previous case the two swimmers shift in order to swim with their physical waveform locked in phase, with the angle of attack of swimming shifted in order to enable this. This final composite body results in similar behaviour as seen for two swimmers locked in phase as seen in the next experiment in Section 4.2.3, but with an initially altered angle of attack. Finally, we observe the outcome for two swimmers with a phase difference of $\Delta\phi = \frac{\pi}{2}$. The result is very similar to the previous case with the small disturbance resulting in the two swimmers locking in phase.

We conclude that the swimmer model appears to follow similar synchronisation tendencies seen in theoretical and experimental studies discussed previously. Further validation would require a more careful numerical analysis of the fluid flow surrounding the filaments, and precisely why the generated flow causes phase-locking when there is a small spatial disturbance to symmetric swimmers. Further experimentation may also reveal an analytical relationship between the resulting angle of attack of the two swimmers and the difference in phase $\Delta\phi$.

4.2.3 Coplanar and Frontal Swimmers

As seen in the previous example, swimmers in close proximity will significantly alter each other's behaviour due to the complex hydrodynamic forces generated between them. Here we ask whether these alterations in behaviour scale when there are a large number of swimmers. The primary motivation for exploring this question is the theoretical study by Llopsis et al. (2013), supported experimentally by Brumley et al. (2014), in which complex findings relating to velocity gains for cooperative swimming were revealed. Namely, parallel swimmers profit from hydrodynamic interactions only when they are directly on top of one another. These studies take place in three-dimensions, so here we aim to discover whether similar trends are possible when more swimmers are added to clusters in our two-dimensional framework.

Experiment

In this experiment we consider two different types of cluster. Firstly, N_s identical swimmers are stacked on top of each other in a coplanar fashion, with the same direction of travel in the positive x -direction. The initial position in the $x - y$ plane for the first segment of the first filament of each swimmer is as follows,

$$x_n = 0, \quad (4.3)$$

$$y_n = \frac{3}{2}D_f(n-1), \quad (4.4)$$

for $n = 1, \dots, N_s$. This represents a vertical separation of $\frac{D_f}{2}$ between swimmers, such that D_f is the inter-filament spacing for an individual swimmer defined previously. The second case we consider is for N_s swimmers in a horizontal chain, which we refer to as frontal swimmers, in which N_s identical swimmers are stacked one behind the other with the same direction of travel in the positive x -direction. For this second case, the initial position in the $x - y$ plane of the first segment of the first filament of each swimmer is as follows,

$$x_n = -(n-1)(L + D_f), \quad (4.5)$$

$$y_n = 0, \quad (4.6)$$

for $n = 1, \dots, N_s$. This represents a horizontal separation of D_f between the tail of one swimmer and the head of the next. Both sets of simulations have the same parameters as before but with steps per unit time $T = 1200$, and the number of repetitions of the unit time period T set to $R = 10$. For each cluster of size N_s , we present measurements averaged across all swimmers to show the average behaviour of an individual swimmer in a cluster of size N_s . Centre of mass velocities are defined as in Section 3.5.5 and averaged over the whole simulation, $\langle u_m \rangle$. When calculating the average hydrodynamic efficiency $\langle \eta_m \rangle$, viscous dissipation $\langle D_m \rangle$ is estimated⁴ by using the viscous dissipation $D_{m'}$ for the final cycle m' .

⁴This was done to cut down on computational time, and is justified due to negligible variation of D_m over the simulation time.

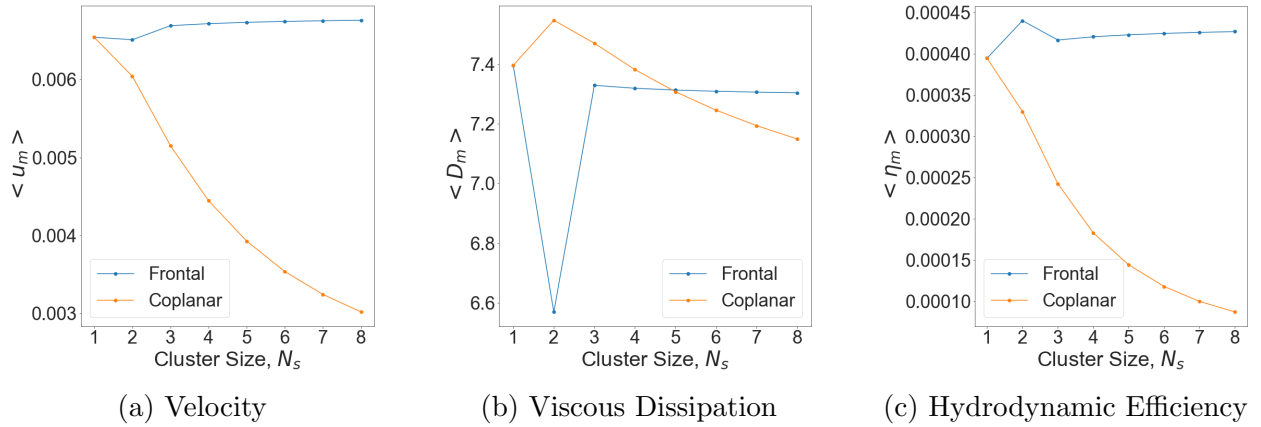


Figure 4.6: Average Individual Swimmer Measurements for Coplanar and Frontal Clusters

Results

Figure 4.6a clearly shows that coplanar swimmers do not benefit from swimming together, with the average swimmer velocity decreasing with each additional swimmer and a total decrease of 53.8% from $N_s = 1$ to $N_s = 8$. This is matched by a decrease in efficiency of 78.0% showed by Figure 4.6c. On the other hand, we see a marginal increase in efficiency for frontal swimmers, with an increase of 8.10% in efficiency and 3.33% for velocity between $N_s = 1$ and $N_s = 8$. This shows that frontal swimmers benefit from swimming one in front of the other, whereas coplanar swimmers one on top of the other are not able to profit from coordination. Figure 4.6b shows the particularly notable case of $N_s = 2$ for frontal swimmers, i.e. two swimmers one in front of the other. The two swimmers in this case greatly benefit in that their average work done against the fluid drops by 10.76% compared to the case for one swimmer. This leads to the higher efficiency seen in Figure 4.6c for this case.

Here we have considered the average velocity and efficiency of an individual swimmer within a cluster. However, in Appendix C the distribution of these measurements within the cluster is detailed. For example, for coplanar clusters of size $3 \leq N_s \leq 5$ the inner swimmers of the cluster are more efficient than those at the top and bottom, with this trend reversing for $N_s \geq 7$. Finally, note that the inter-segment repulsive forces defined by \mathbf{F}^S in Section 2.3.1 may be significantly influencing the inter-swimmer interactions for coplanar swimmers due to the small separation gap leading to a greater contribution of repulsive forces.

On a final note, in the study by Llopsis et al. (2013), coplanar swimmers approach each other and frontal swimmers repel each other, with coordination between coplanar swimmers being made possible by rotations. Rotations such as this are not possible in our two-dimensional model, as it does not allow for twisting or rotation through an axis placed in the plane of undulation. In the case of one swimmer we noted that two dimensions were sufficient for capturing the detail of the axoneme, however we see this becomes a limitation when introducing multiple swimmers.

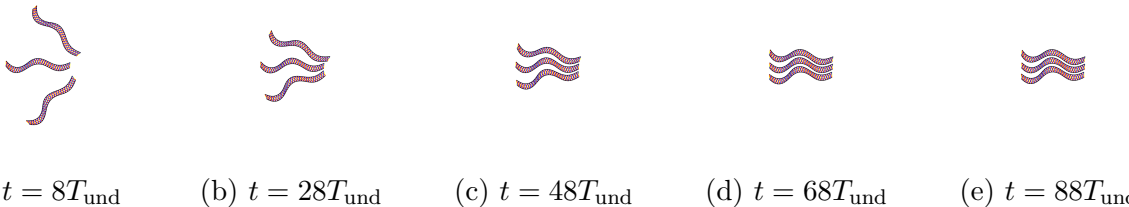


Figure 4.7: Collision Between Three Swimmers

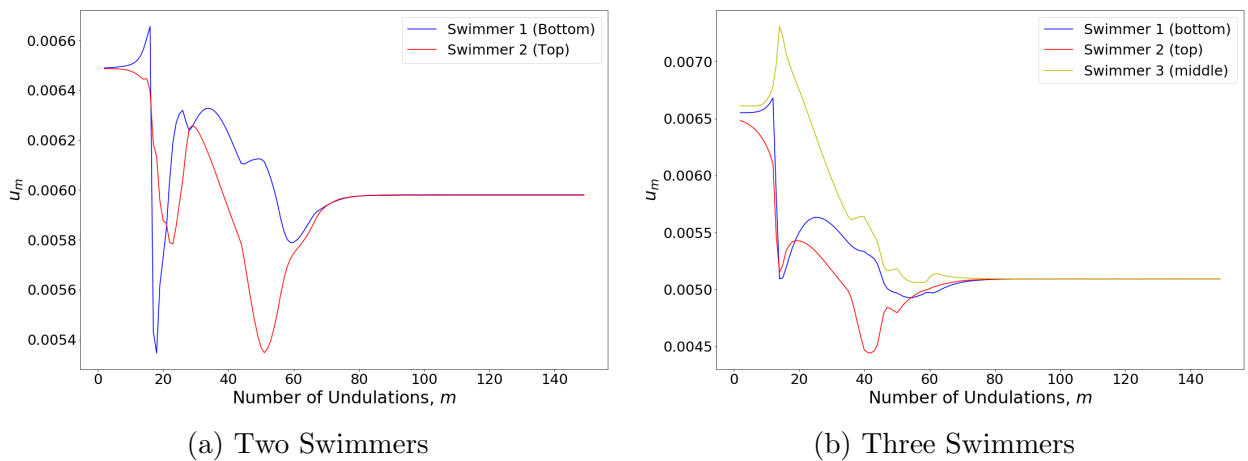


Figure 4.8: Collision between Multiple Swimmers, Velocity

4.2.4 Collisions

Experiment

Now we consider a similar experiment with coplanar swimmers, but instead of instigating motion at the point of being coupled we investigate what happens if coplanar swimmers collide, expecting that they couple after a sufficient amount of time. First we consider two identical swimmers approaching each-other with a right-angle difference in initial swimming direction, and then we consider the same two swimmers with the addition of a third identical swimmer placed in between them with all three approaching each-other. See Figure 4.7 for the case of three swimmers. Again, we set the steps per unit time to $T = 1200$ and the number of repetitions $R = 30$, allowing a much longer running time than for previous experiments.

We consider the moving-average centre-of-mass velocity defined in Section 3.5.5, u_m , such that $m \in \{0, 1, \dots, \gamma R - 1\}$ for γ the number of undulations per unit time period T . To recap, u_m gives a measure for the average velocity over the period of the m^{th} undulation, and here the index m can also be thought of as the number of undulations completed by an individual swimmer. It is consistent to use this as a time index when reporting velocities of multiple swimmers as all the swimmers have identical undulation cycles. Figure 4.8 shows how centre-of-mass velocities change over time for the two cases, omitting $m = 0$ and $m = 1$ to remove the initial undulations of settling time.

Results

First we discuss the case of two swimmers. Figure 4.8a shows that the two swimmers start at the average velocity of one independent swimmer, with the approach considerably altering their velocities. The collision lasts approximately $m = 80$ undulation cycles, after which the swimmers assume the approximate velocities seen for two coplanar swimmers in Section 4.2.3. This example shows clear coordination between two identical swimmers that are not initially coordinated, as after their approach the swimmers assume the coordinated behaviour seen for non-colliding coplanar swimmers, with a negligible difference of 0.01% between the average velocities for both cases. Secondly we consider an additional swimmer approaching between the two swimmers that are at a right-angle. The colours for each swimmer in Figure 4.8b are consistent with Figure 4.8a, showing that the bottom and top swimmers follow similar trends regarding velocities as the approach occurs, with the middle swimmer initially gaining velocity significantly. The final settled velocities are again similar to those seen for three non-colliding coplanar swimmers in Section 4.2.3, with a slightly higher but still small difference of 3.2% between average velocities of the two cases. These two experiments demonstrate the capability of the swimmers to coordinate into a settled state despite having initially different angles of attacks and positionings.

These two cases provide insight into further capabilities of the swimmer model we have created when it comes to modelling multi-swimmer environments. Also note that the interactions observed here, and in the coplanar and frontal swimmers experiment, are similar to the theoretical study by Yoshinaga & Liverpool (2018) for individual particles. The experiments by Yoshinaga & Liverpool (2018) differ in that each swimmer is a single particle, and the near-field fluid dynamic interactions are theoretically analysed using lubrication theory, whereas the near-field interactions in this model may instead be influenced by the repulsive forces that model the steric interactions discussed in Section 2.3.1. A similar study applied to the collisions and multi-swimmer set up here may provide a theoretical framework for the observed outcomes discussed above regarding collisions, clusters and synchronisation.

4.3 Conclusion

This section demonstrated the capability of the swimmer model to be expanded for more complicated tails and for producing characteristics that one would expect when multiple swimmers are set up to interact with each other. First, we successfully defined and evaluated two different kinds of swimmers, head-driven and tail-driven, and we optimised the former case in which there is a decay in internal forcing in the tail motivated by an assumed decrease in ATP. Secondly, in the case of multiple swimmers we demonstrated synchronisation, coordination, the effects of different cluster sizes, and in Appendix D we present two further examples of larger scale multiple swimmer interactions. In the conclusion of this thesis, we review and evaluate these findings and consider how to expand the model further.

Chapter 5

Conclusion

5.1 Summary of Results

The goal of this thesis was to define, refine and extensively test a novel axoneme model for microswimmers in Stokes Flow. The axoneme model consisted of two individual Kirchhoff filaments, inter-connected by a network of internal cross-linked driving forces dependent on geometrical information and an internal clock, representing the biological nature of active dynein motor proteins connecting the microtubules of the flagellum cytoskeleton. The axoneme model was simulated using a modification of an existing hydrodynamic solver for Kirchhoff filaments in Stokes Flow. After exploring how the model functioned, a final model with a symmetrically spatial movement and arc-length-dependent decay in beating amplitude was selected for evaluation. The model was also shown to be adaptable to different modes of locomotion such as peristalsis seen in mites. The subsequent optimisation on the final model revealed the importance of two parameters in particular, namely the wavenumber and the amplitude, by observing the effect that their variation had on displacement, viscous dissipation, hydrodynamic efficiency, and centre-of-mass velocity. In the final experiment, efficiencies near 0.055% were recorded for the most efficient swimmers, a result below that of single-filament models in the literature, however the efficiency measurements proved useful in comparing variants of the model. A significant result from the optimisation was that the optimal wavenumber for a swimmer is non-trivially dependent on the undulation amplitude, and that optimal variants of the model rarely coincide with the fastest variants.

This model was then modified in an attempt to capture more nuanced biologically-motivated behaviour, and placed in complex environments to observe interactions with other swimmers. Firstly, the model was expanded by introducing a variation of the inner driving force amplitude, which defined two sets of swimmers referred to as head-driven and tail-driven respectively. A detailed parameter search revealed that head-driven swimmers are optimal when their tails are approximately one fifth of the total body length, with the initial head-driven model proving to be one of the least efficient variants. Finally, experiments on multiple swimmers revealed a number of interesting results: two identical swimmers swimming out of phase will shift to swim in phase; two identical swimmers symmetrically out of phase will not change their swimming behaviour; the most efficient case for a chain of frontal swimmers is to have two swimmers; the average velocity of a swimmer in a coplanar cluster will decrease as the cluster size increases; and that the model can be used to capture coordination of

multiple swimmers at different initial positions and orientations.

5.2 Conclusions, Applications, and Further Work

The axoneme model for microswimmers presented in this thesis can be developed further in order to capture more intricate biological behaviours. In particular, a similar model could be computationally set up in three-dimensions, adapting the theoretical framework defined by Schoeller et al. (2019a) with the corresponding computational environment in Schoeller et al. (2019b) for individual filaments falling under gravity. This would require extending the axoneme model presented in Section 3.2 to three-dimensions, which would be reasonably intuitive to carry out using three equally spaced Kirchhoff filaments inter-connected by cross-linked driving forces to instigate either planar beating or helical travelling waves. However the physics defined in Section 2.3 becomes more complex, requiring the use of quaternions and a geometric time integration scheme (Schoeller et al. 2019a). Furthermore, a version of the computational model that develops the dynamical system defined in Han & Peskin (2018) in order to generate spontaneous oscillations in ciliary beating could be explored, despite being more appropriate for tethered motile cilia with a recovery and power stroke rather than for microswimmers.

Despite primarily using measurements of hydrodynamic efficiency as a method for comparing variants of our model, the efficiencies produced were low compared to other existing models. Maximising this measure of efficiency would enable more direct comparisons between this model and those seen elsewhere, such as the *Caenorhabditis elegans* model by Majmudar et al. (2012) and the optimal elastic flagellum by Spagnolie & Lauga (2010). Efficiencies of individual swimmers may be increased by greatly increasing the inner driving amplitudes, ensuring that the length of the body is much longer than the inter-filament gap, manipulating the variation of cross-sectional distance using the passive cross-links, and selectively choosing wavenumber according to the amplitude.

Finally, in this thesis we undertook numerical tests with multiple identical swimmers in different kinds of groupings. However further studies could observe how the behaviours of individuals in clusters change when the individuals are assigned wildly different initial parameters as well as the different types of tails explored in Section 4.1. For example, the framework presented here would have the capability of placing multiple swimmers with varying wavenumbers together, with the expectation that swimmers of similar wavenumbers will congregate.

The pursuit of modelling biological organisms in the manner carried out here has two main applications. The first is to acquire a systematic understanding of how organisms work, gaining more insight into what kinds of mathematical mechanisms accurately govern biological motion. The axoneme has fascinated scientists for decades, and mathematical models which replicate real-world behaviour are essential as they reveal the most important characteristics of the axoneme in the context of organism locomotion. The second is to use the models defined here for biomedical purposes. For example, for the delivery of biological matter including cells and bacteria. This is being made possible by recent developments in biomechanical engineering, such as the construction of microscopic self-propelled tori that move according to magnetic fields (Baker et al. 2019). Similar studies have been undertaken to develop microswimmers that can adapt to different environments with minimal additional

tools such as sensors (Lauga & Powers 2009). The model defined here could be similarly adapted for the development of physical mechanical microswimmers which exhibit biological locomotion. Finally, an understanding of internal structures of sperm flagella alongside the use of established sperm sorting technology (Katigbak et al. 2019) can be developed to better understand the causes of infertility. In particular, our model could be adapted to introduce magnetic fields with the goal of understanding how the swimmers react to magnetophoresis, with extensive applications for sperm cell sorting in assisted reproduction (Koh 2015, 2018). Developing a deeper understanding of the human sperm cell is crucial in tackling infertility, experienced by 8-12% of couples around the world with up to 2% of men experiencing some form of sub-optimal sperm concentration and mobility (Kumar & Singh 2015).

5.3 Code for Multiple Swimmers

The code used for the axoneme model is available with instructions at the following link:

<https://github.com/petermnhull/MastersProject>.

This version has been set up in MATLAB R2019b for further use and organised so that the user can easily modify parameters such as initial positions and number of swimmers. The reader is encouraged to experiment with the model, particularly for implementing further modifications and exploring how the swimmers operate in complex environments.

Bibliography

- Acheson, D. J. (1990), *Elementary Fluid Dynamics*, Oxford University Press.
- Adams, M., Smith, U. M., Logan, C. V. & Johnson, C. A. (2007), ‘Recent advances in the molecular pathology, cell biology and genetics of ciliopathies’, *Journal of Medical Genetics* **45**.
- Ascher, U. M. & Petzold, L. R. (1998), *Computer Methods for Ordinary Differential Equations and Differential-Algebraic Equations*, Vol. 61, SIAM.
- Audoly, B. & Pomeau, Y. (2010), *Elasticity and Geometry: From Hair Curls to the Non-Linear Response of Shells*, Oxford University Press.
- Baker, R. D., Montenegro-Johnson, T., Sediako, A. D., Thomson, M. J., Sen, A., Lauga, E. & Aranson, I. S. (2019), ‘Shape-programmed 3d printed swimming microtori for the transport of passive and active agents’, *Nature Communications* **10**.
- Blum, J. J. & Lubliner, J. (1973), ‘Biophysics of flagellar motility’, *Annu. Rev. Biophysics. Bioeng.* **2**.
- Bolton, S., Bauchan, R. G., Ochoa, R., Pooley, C. & Klompen, H. (2015), ‘The role of integument with respect to different modes of locomotion in the nematalycidae (endeostigmata)’, *Experimental and Applied Acarology* **15**, 149–161.
- Brokaw, C. J. (1965), ‘Non-sinusoidal bending waves of sperm flagella’, *J. Exp. Biol.* **43**.
- Brokaw, C. J. (1972), ‘Flagellar movement: a sliding filament model’, *Science (Wash. D.C.)* **178**.
- Broyden, C. G. (1965), ‘A class of methods for solving nonlinear simultaneous equations’, *Mathematics of Computation* **19**, 577–593.
- Brumley, D. R., Wan, K. Y., Polin, M. & Goldstein, R. E. (2014), ‘Flagellar synchronization through direct hydrodynamic interactions’, *eLife* **3**.
- Camalet, S. & Jülicher, F. (2000), ‘Generic aspects of axonemal beating’, *New Journal of Physics* **2**, 1–23.
- Chemes, E. C. & Sedo, C. A. (2012), ‘Tales of the tail and sperm head aches: Changing concepts on the prognostic significance of sperm pathologies affecting the head, neck and tail’, *Asian Journal of Andrology* **14**, 12–23.
- Childress, S. (1981), *Mechanics of Swimming and Flying*, Cambridge University Press.
- Cummins, J. & Woodall, P. (1985), ‘On mammalian sperm dimensions’, *Journal of Reproduction and Fertility* **75**, 153–175.

-
- Dance, S. L., Climent, E. & Plouraboué, F. (2004), ‘Collision barrier effects on the bulk flow in a random suspension’, *Physics of Fluids* **16**, 828–831.
- Elgeti, J., Kaupp, U. B. & Gompper, G. (2010), ‘Hydrodynamics of sperm cells near surfaces’, *Biophysical Journal* **99**, 1018–1026.
- Fackler, O. T. & Grosse, R. (2008), ‘Cell motility through plasma membrane blebbing’, *Journal of Cell Biology* **181**, 879–884.
- Fisher, H. S., Giomi, L., Hoekstra, H. E. & Mahadevan, L. (2014), ‘The dynamics of sperm cooperation in a competitive environment’, *Proceedings of the Royal Society B* **281**.
- Fu, C. H. & Powers, T. R. (2007), ‘Theory of swimming filaments in viscoelastic media’, *Physical Review Letters* **99**.
- Gibbons, I. R. (1981), ‘Cilia and flagella of eukaryotes’, *Journal of Cell Biology* **91**, 107–124.
- Gong, A., Rode, S., Kaupp, B., Gompper, G., Elgeti, J., Friedrich, B. M. & Alvarez, L. (2019), ‘The steering gaits of sperm’, *Philosophical Transactions of the Royal Society B* **375**.
- Gray, J. & Hancock, G. J. (1955), ‘The propulsion of sea-urchin spermatozoa’, *J. Exp. Biol.* **32**, 802–814.
- Han, J. & Peskin, C. S. (2018), ‘Spontaneous oscillation and fluid-structure interaction of cilia’, *Proceedings of the National Academy of Sciences of the United States of America* **155**, 4417–4422.
- Hilfinger, A., Jülicher, F. & Chatopadhyay, A. K. (2009), ‘Nonlinear dynamics of cilia and flagella’, *Physical Review E* **79**.
- Johnson, R. E. (1979), ‘A comparison between Resistive-Force Theory and Slender-Body Theory’, *Biophysical Journal* **25**, 113–127.
- Juhász, Z. & Zelei, A. (2013), ‘Analysis of worm-like locomotion’, *Periodica Polytechnica* **57**.
- Kamal, A. & Keaveny, E. E. (2018), ‘Enhanced locomotion, effective diffusion and trapping of undulatory micro-swimmers in heterogeneous environments’, *Journal of Royal Society Publishing Interface* **15**.
- Katigbak, R. D., Turchini, G. M., de Graaf, S. P., Kong, L. & Dumée, L. F. (2019), ‘Review on sperm sorting technologies and sperm properties toward new separation methods via the interface of biochemistry and material science’, *Advanced Biosystems* **3**.
- Koh, J. B. Y. (2015), ‘The study of spermatozoa and sorting in relation to human reproduction’, *MicroFluid Nanofluid* **18**, 755–774.
- Koh, J. B. Y. (2018), Theoretical study of spermatozoa sorting by dielectrophoresis or magnetophoresis with supervised learning, PhD thesis, Nanyang Technological University, Singapore.
- Kumar, N. & Singh, K. A. (2015), ‘Trends of male factor infertility, an important cause of infertility: A review of literature’, *Journal of Human Reproductive Sciences* **8**, 191–196.
- Lammermann, T. & Sixt, M. (2009), ‘Mechanical modes of ‘amoeboid’ cell migration’, *Current Opinion in Cell Biology* **21**, 636–644.

-
- Landau, L. D. & Lifshitz, E. M. (1970), *Course of Theoretical Physics, Volume 7: Theory of Elasticity*, Permagon Press Ltd.
- Lauga, E. & Powers, T. R. (2009), ‘The hydrodynamics of swimming microorganisms’, *Reports on Progress in Physics* **72**.
- Lighthill, J. (1975), *Mathematical Biofluidynamics*, SIAM.
- Lim, S., Ferent, A., Wang, X. S. & Peskin, C. S. (2008), ‘Dynamics of closed rod with twist and bend in fluid’, *SIAM Journal on Scientific Computing* **31**, 273–202.
- Lindemann, C. B. & Lesich, K. A. (2010), ‘Flagellar and ciliary beating: the proven and the possible’, *Journal of Cell Science* **123**, 519–528.
- Lindemann, C. B. & Lesich, K. L. (2016), ‘Functional anatomy of the mammalian sperm flagellum’, *Cytoskeleton* **73**, 652–669.
- Liu, S., Leung, C., Lu, Z. & Sun, Y. (2013), ‘Quantitative analysis of locomotive behaviour of human sperm head and tail’, *IEEE Transactions on Biomedical Engineering* **60**.
- Llopsis, I., Paganabarraga, I., Consentino Lagamarsino, M. & Lowe, C. (2013), ‘Cooperative motion of intrinsic and actuated semiflexible swimmers’, *Physical Review E* **87**.
- Lodish, H., Berk, A., Zipursky, S. L., Matsudaira, P., Baltimore, D. & Darnell, P. (2000), *Molecular Cell Biology*, 4 edn, W.H. Freeman.
- Majmudar, T., Keaveny, E. E., Zhang, J. & Shelley, M. J. (2012), ‘Experiments and theory in a simple structured medium’, *Journal of Royal Society Interface* **9**, 1809–1823.
- Nan, B., McBride, M. J., Chen, J., Zusman, D. R. & Oster, G. (2014), ‘Bacteria that glide with helical tracks’, *Current Biology* **24**.
- Ounjai, P., Kim, K. K., Lishko, P. V. & Downing, K. H. (2012), ‘Three-dimensional structure of the bovine sperm connecting piece revealed by electron cryotomography’, *Biology of Reproduction* **87**, 1–9.
- Porter, M. E. & Sale, W. S. (2000), ‘The 9+2 axoneme anchors multiple inner arm dyneins and a network of kinases and phosphatases that control motility’, *Journal of Cell Biology* **151**.
- Purcell, E. (1977), ‘Life at low reynolds number’, *American Journal of Physics* **45**, 3–11.
- Riedel-Kruse, I. H., Hilfinger, A., Howard, J. & Jülicher, F. (2007), ‘How molecular motors shape the flagellar beat’, *HFSP Journal* **1**, 192–208.
- Rikmenspeol, R. (1978), ‘Equations of motion for sperm flagella’, *Biophysical Journal* **23**, 177–206.
- Ruban, A. I. & Gajjar, J. S. B. (2014), *Fluid Dynamics: Part 1: Classical Fluid Dynamics*, Oxford University Press.
- Saggiorato, G., Alvarez, L., Jikeli, J. F., Kaupp, U. B., Gompper, G. & Elgeti, J. (2017), ‘Human sperm steer with second harmonics of the flagellar beat’, *Nature Communications* **8**.
- Schoeller, E., Townsend, A. K., Westwood, T. A. & Keaveny, E. E. (2019a), ‘Methods for suspensions of passive and active filaments’. arXiv:1903.12609.

-
- Schoeller, E., Townsend, A. K., Westwood, T. A. & Keaveny, E. E. (2019b), ‘Methods for suspensions of passive and active filaments, supplementary MATLAB/Octave code’, <https://github.com/ekeaveny/filaments/tree/master/matlab-2d-rpy>. Accessed: 01.10.2019.
- Schoeller, S. F. & Keaveny, E. E. (2018), ‘From flagellar undulations to collective motion: predicting the dynamics of sperm suspensions’, *Journal of the Royal Society Interface* **15**.
- Spagnolie, S. E. & Lauga, E. (2010), ‘The optimal elastic flagellum’, *Physics of Fluids* **22**.
- Wajnryb, E., Mizerski, K. A., Zuk, P. J. & Szymczak, P. (2013), ‘Generalization of the Rotne-Prager-Yamakawa mobility and shear disturbance tensors’, *Journal of Fluid Mechanics* **731**.
- Wolgemuth, C., Hoiczyk, E., Kaiser, D. & Oster, G. (2002), ‘How myxobacteria glide’, *Current Biology* **12**, 369–377.
- Woolley, D. M. & Vernon, G. G. (2001), ‘A study of helical and planar waves on sea urchin sperm flagella’, *The Journal of Experimental Biology* **204**, 1333–1345.
- Yoshinaga, N. & Liverpool, T. A. (2018), ‘From hydrodynamic lubrication to many-body interactions in dense suspensions of active swimmers’, *The European Physical Journal E* **41**.
- Zusman, D. R., Scott, A. E., Yang, Z. & Kirby, J. R. (2007), ‘Chemosensory pathways, motility and development in *Myxococcus xanthus*’, *Nature Reviews Microbiology* **5**, 862–872.

Appendices

Appendix A

Additional Examples

Here we detail some additional examples of configurations for bending motion and swimming not used in the final model. These models were motivated more by curiosity when initially building the cross-link mechanism.

A.1 Bending Dynamics

A.1.1 Trigonometric Arc-Length Dependence

Instead of the linear variation, trigonometric functions can be used in the forcing variation to achieve a different equilibrium position.

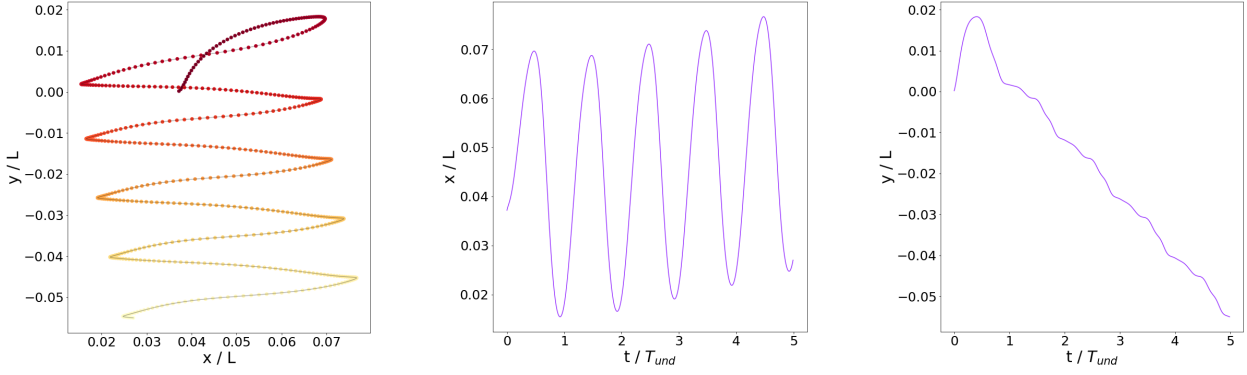
$$f^{(a)}(s, t) = \sin(\pi s) \quad (\text{A.1})$$

$$f^{(b)}(s, t) = \cos(\pi s) \quad (\text{A.2})$$

The motion of the filaments can be seen in Figure A.1, indexed by proportion of time taken to obtain equilibrium position. The shape is much less uniform than in the linear example in the main text.



Figure A.1: Bending Motion to Equilibrium, Trigonometric Arc-Length Dependence



(a) Head motion, dark to light as time increases.

(b) Centreline x position of head over time.

(c) Centreline y position of head over time.

Figure A.2: Motion of Swimmer, Second Example

A.2 Swimming Examples

A.2.1 Asymmetric Swimmer, Second Example

In an attempt to reduce the asymmetry in the Example 3.4.1, we set the following for our arc-length and time dependent functions,

$$f^{(a)}(s, t) = \beta(s) \sin(\Phi(s, t)) \quad (\text{A.3})$$

$$f^{(b)}(s, t) = \beta(s) \cos(\Phi(s, t)) \quad (\text{A.4})$$

for the usual wave propagation function,

$$\Phi(s, t) = ks - \omega t + \phi. \quad (\text{A.5})$$

We use the usual parameters as given in Table 3.3. The motion of the centreline of the head can be seen in Figures A.2a, A.2b and A.2c. This model has similar issues to that in Section 3.4.1.

A.2.2 Swimmers without Passive Links

An interesting detour revealed the importance of the passive horizontal stiff springs in the functioning of the asymmetric swimmers. If the yellow cross-links are removed from the asymmetric swimmer in Section A.2.1, then the filaments move in a completely decoupled way, as can be seen in Figure E.3 in Appendix E. The asymmetry leads to the motion being dictated by the filament which first experiences the majority of the driving force, leading to an undulation of the left filament which is passively attached to the right filament. This decoupling is not present for a version of the swimmer in Section 3.4.2 without passive links, appearing to undulate as normal as can be seen in Figure E.5. Decoupling is also much less apparent for the asymmetric swimmer in Section 3.4.1 with passive links removed.

We can conclude that in some cases the passive links are not necessary in order to achieve undulatory motion in completely symmetric systems, however these are retained in further models due to the biological motivation to preserve structure and in order to substitute for the geometric constraint presented by Han & Peskin (2018).

A.2.3 Biologically-Motivated Swimmer

In this section we briefly consider how we can more closely represent a biological organism. In particular we can choose parameters so that our model mimics the flagellum of mammalian sperm such as ram sperm, as reported in the relevant literature. The primary issue relates to the length scales of the swimmer. Our models had the following parameters, measuring the diameter from the middle of a segment across to the middle of the corresponding segment of the adjacent filament.

Parameter	Interpretation	Formula	Numerical Value
L_d	Swimmer diameter	$2a + D_f$	7
L	Swimmer length	ND	68.2

Table A.1: Standard parameters for filament lengths.

Therefore, $L \approx 9.7L_d$ in our model so far. Normally one would expect a difference of at least an order of magnitude. In order to more accurately replicate flagellum behaviour, we increase N from 31 to 65, which gives $L = 143$. This gives a new proportionality of $L \approx 20.4L_d$, a more convincing difference. This is still not in the same region as reported in the literature for some species of spermatozoa. For example, Koh (2015) reports a length-diameter ratio of 76 to 94 for human male sperm, and Schoeller & Keaveny (2018) use a ratio of 70.1 in mathematical modelling of ram sperm. Furthermore, in the biological literature Cummins & Woodall (1985) report a ratio of 448 for human spermatozoa, which is significantly higher than the ratio used here. However, increasing N significantly higher will lead to high computational cost. Also note that a more direct way to increase the length without adding the same computational cost would be to decrease the inter-filament separation D_f while retaining the same value of N .

Now, we re-use the internal forcing defined in Section 3 with number of segments increased to $N = 65$. All other parameters are kept the same as in Section 3.4.3, apart from replacing the amplitude with $\lambda = 2.86$, and in particular noting the linear decay in forcing $\beta(s)$ that was introduced to represent the decrease in availability of ATP. The motion can be seen in Figure A.3. There are many other factors that should be considered in further work to better optimise the model for the purpose of biological accuracy. Most importantly, sperm cells have a head to which the tail is clamped. This has recently been overlooked when considering sperm gait (Gong et al. 2019), however it is often taken into account in computational models (Elgeti et al. (2010), Schoeller & Keaveny (2018)) and is integral to the motion of the organism (Liu et al. (2013)).

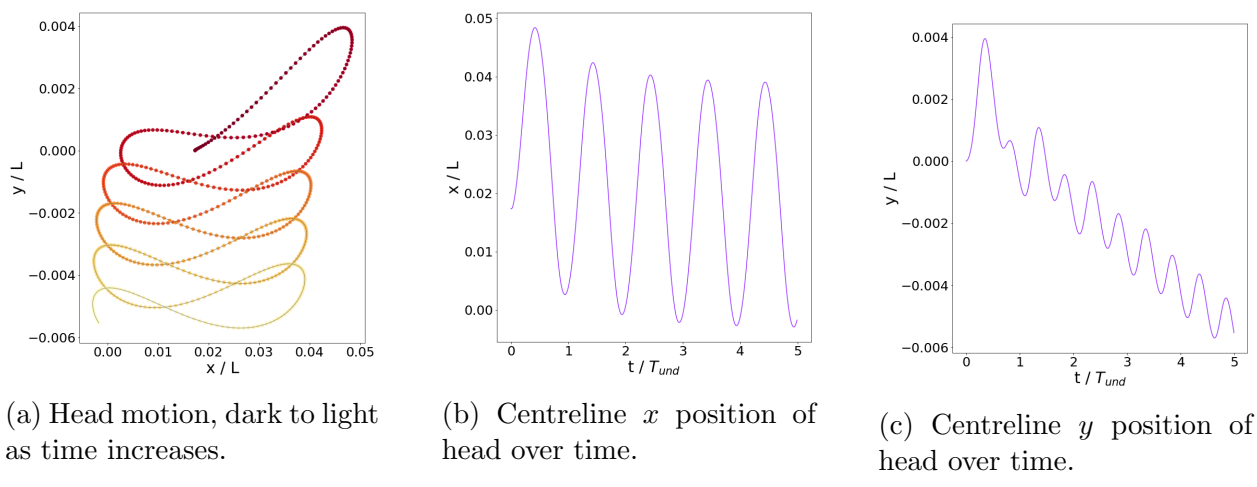


Figure A.3: Motion of Biologically-Motivated Swimmer

Appendix B

Hydrodynamic Efficiency

Before arriving at the final definition of efficiency used in Section 3.5.5, an alternate definition was used for optimisation which we detail here. In finding flagellar motion that achieves a minimum rate of working to achieve a given swimming speed, Lighthill (1975) defines the parameter η as ‘the ratio of an animal’s rate of working at a swimming speed to the rate of working required by an external force to drag the animal through the fluid at that speed with its flagellum stretched straight behind it’. Therefore, in contrast to the measurements used in the main text with this as the motivation, we can define the following as the hydrodynamic efficiency of our swimmer at time step m ,

$$\eta_m = \frac{\alpha_f(u_m)^2}{D_m}, \quad (\text{B.1})$$

further defining $\eta = \langle \eta_m \rangle_T$ as in Section 3.5.5. Velocity u_m and viscous dissipation D_m are calculated as in Section 3.5.5. Here the only difference in the efficiency measurement to the definition in Section 3.5.5 is the introduction of α_f , the frictional coefficient associated with dragging an inactive cross-linked body through the liquid at speed u . The frictional coefficient can be thought of intuitively as the ratio of normal to tangential resistance. This is consistent with commonly used measures of hydrodynamic efficiency for Low Reynolds number swimming. This measure was used in calculations by Spagnolie & Lauga (2010) for determining optimal elastic swimmers. Spagnolie & Lauga (2010) also note that this measure of hydrodynamic efficiency can be further modified to include measures of bending and sliding to penalise certain behaviours when optimising against this parameter.

Due to the Low-Reynolds number hydrodynamics outlined in Section 2.3.2, we know that velocity and forces are linearly related. Therefore, we can consider our cross-linked filament body but with inactive cross-linked forces, where the only forces and velocities to account for are a constant velocity u_f in the direction of travel, and F_f , a constant external force dragging the body through the fluid. This means that we can simply choose a pulling force F_f , calculate the centre of mass velocity v over the period T , giving us our frictional coefficient α_f ,

$$u_f = \alpha_f F_f \implies \alpha_f = \frac{u_f}{F_f}. \quad (\text{B.2})$$

Therefore, a total force of $F_f = 1$ is applied to the swimmer with the same parameters as

before except with the inner driving force functions set to zero,

$$f^{(a)}(s, t) = f^{(b)}(s, t) = 0. \quad (\text{B.3})$$

The pulling force is applied through two forces of magnitude 0.5 to the first segment of each of the two filaments. This gives a value of $\alpha_f \approx 0.00309$. Note that this will be the same as the average velocity of the inactive composite body.

Note that choosing this value as our coefficient of friction makes sense, as we define the hydrodynamic efficiency as the ratio of rate of work done to the rate of work required by an external force to drag the animal at that velocity. Substituting $\alpha_f = \frac{u_f}{F_f}$ back into (B.1) would give a ratio of two different rates of work done. We know that α_f is constant with respect to λ_s and k_s as, in this case, these parameters have no function in the inactive cross-links.

Due to the fact that the efficiencies provide a an approximation of how much work is going into displacement, this measurement of efficiency is useful for comparing variants of the same model defined in the main text. However the hydrodynamic efficiencies produced with the measurement here are considerably below those reported in the literature for mathematically modelled flagellum, and is small compared to the efficiency measurements calculated in Section 3.5.5. This likely results in the choice of the value of α_f being too small.

Appendix C

Coplanar and Frontal Swimmers

The bar plots below display the variation of the velocity, work done and efficiency of individual swimmers in coplanar and frontal clusters seen in Section 4.2.3.

For coplanar clusters, swimmer 1 signifies the swimmer on the bottom of the cluster and the highest number signifies the swimmer on the top. For $N_s \geq 5$ Figure C.1a shows that as N_s increases over $N_s \geq 5$ the swimmers on the inside of the cluster start swimming considerably slower than those on the outside. Figure C.2a shows that the swimmers on the top and the bottom of the cluster always do the most work and that the amount of work against the fluid is constant regardless of the cluster size. Figure C.3a shows that for $3 \leq N_s \leq 5$, the inner swimmers of coplanar clusters are more efficient than the outer swimmers.

For frontal clusters, swimmer 1 signifies the swimmer at the front of the cluster and the highest number signifies the swimmer at the back. In Figure C.2b we can clearly see that the cluster size N_s has no effect on the viscous dissipation, apart from the case $N_s = 2$ where the two swimmers coordinate effectively. This is shown in Figure C.3b by a notable increase in efficiency, particularly for the swimmer at the front of the pair. Furthermore, in Figure C.1b we see that whilst the average velocity marginally increases as N_s increases, so does the range of velocities. We also see that the further back the swimmer is in the cluster, the slower it swims.

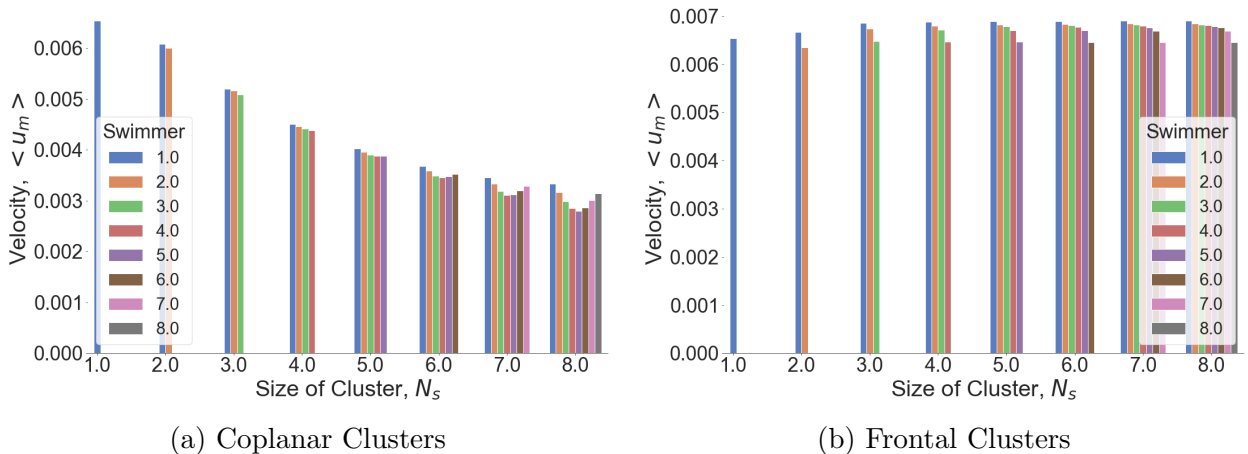


Figure C.1: Velocities of Individual Swimmers in Clusters

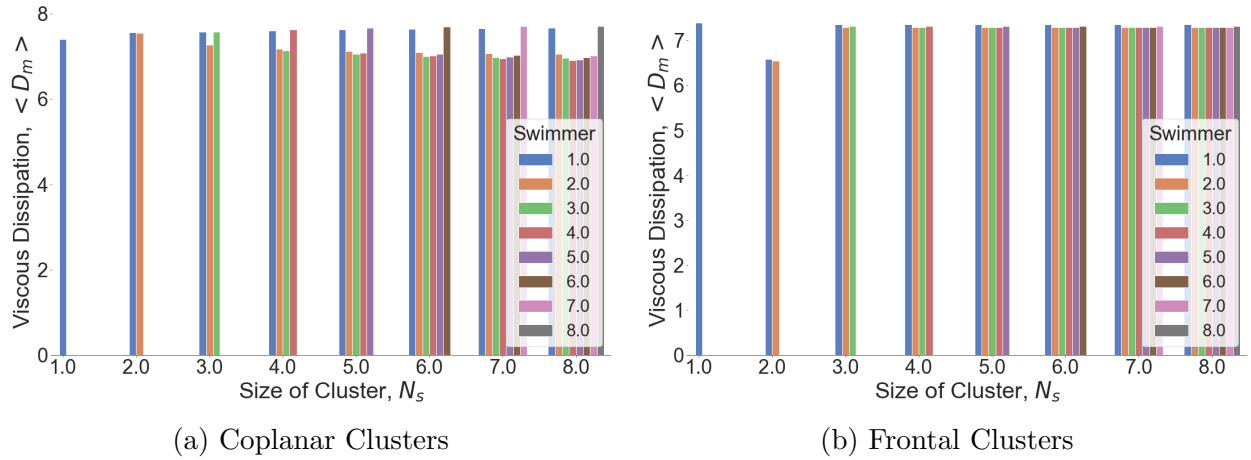


Figure C.2: Average Viscous Dissipation of Individual Swimmers in Clusters

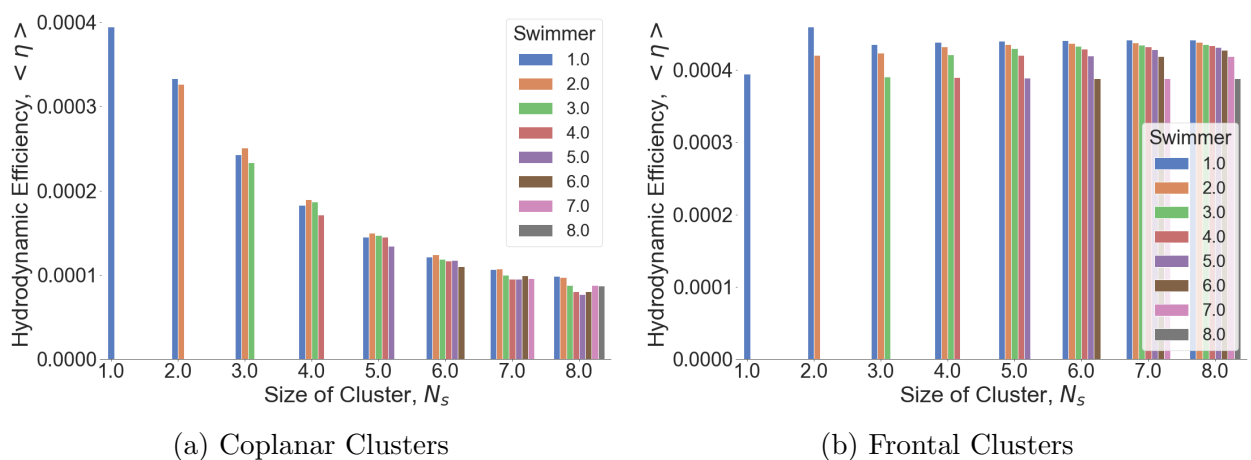


Figure C.3: Hydrodynamic Efficiency of Individual Swimmers in Clusters

Appendix D

Large-Scale Coordination

In Section 4.2 we sought numerical results through observations of simple scenarios involving two or three identical models. Here we present two proof of concept experiments for large-scale multi-swimmer interactions. Our first experiment consists of eight identical swimmers which vary only in amplitude ratio λ_s and phase ϕ . These parameters, along with initial positions, direction of travel, and angle of incidence, are randomised. The results of their interactions over 20 repetitions of the unit time period T can be seen in Figure D.1. Due to the slow speed of most of the swimmers, there is not considerable movement for six of the eight swimmers. However, two of the swimmers clearly influence each other's behaviour. It is also clear that swimmers that do not come into sufficiently close contact do not influence each others' behaviours.

The second environment is specifically created for large-scale coordination, with the goal of observing the outcome of having multiple swimmers come together in the same way seen in Figure D.1. Here, we initialise five identical swimmers according to our standard model with an amplitude ratio $\lambda_s = 11$, which differ only in phase ϕ and initial positioning. The full visual results can be seen in Figure E.18, Appendix E. The initial position and centre-of-mass velocity of swimmers can be seen here in Figure D.2.

Figure D.2b shows the evolution of the velocities of the swimmers over time. Due to the less structured environment, none of the swimmers settle into a certain pattern within the simulation time, but they do seem to approach a common velocity towards the end. Another notable feature is that after approximately $m > 60$ undulations, the red and blue swimmers near the front of the cluster have similar patterns in speed variation, as do the three swimmers in the middle-back of the cluster. The first group speed up together and the second group appear to slow down closely together.

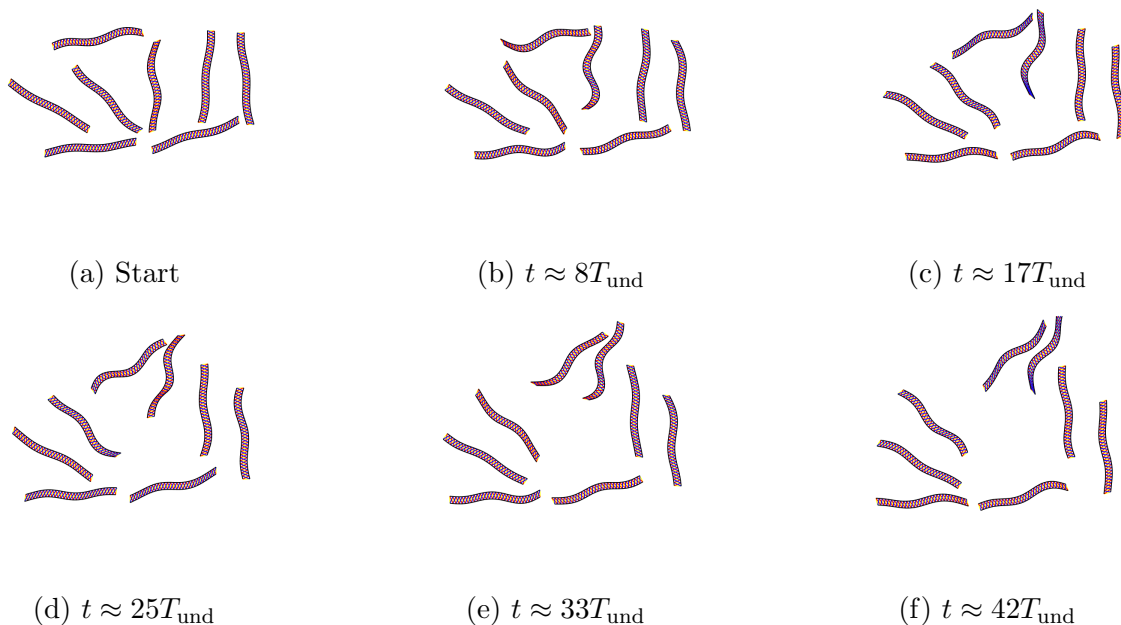


Figure D.1: Multiple Swimmers, Randomised Phase and Amplitude

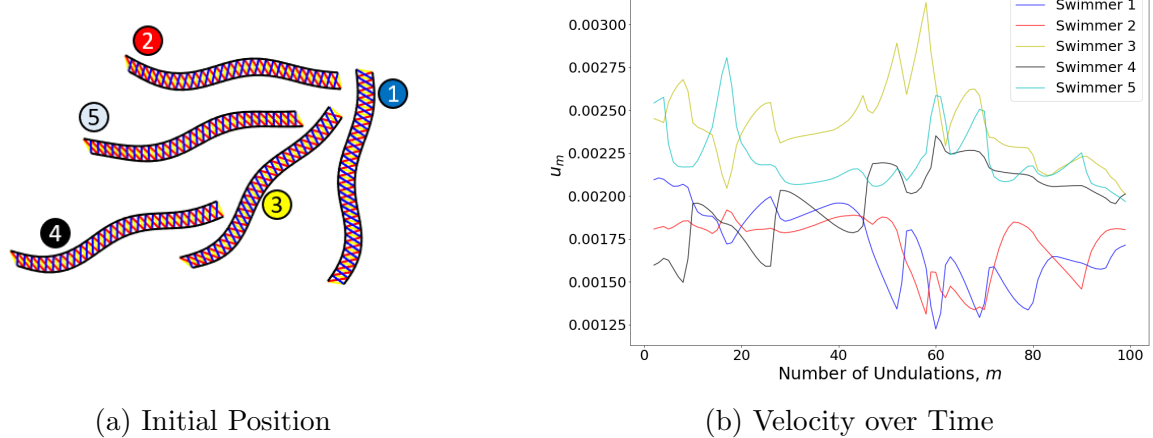


Figure D.2: Multiple Coordinated Swimmers

Appendix E

Swimmer Visualisations

Representative locomotive behaviour of most of the models considered in this thesis are presented below. The frame is fixed at the average (x, y) coordinate of the segments of the filaments. Representative behaviour during periods of the locomotion is displayed left to right as time increases. The frames increase at equal time steps from left to right. The direction of travel for individual swimmers is in the negative y -direction.

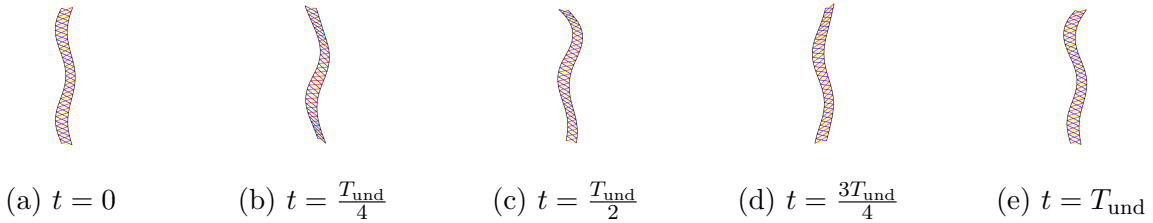


Figure E.1: Undulation Cycle of Second Asymmetric Swimmer

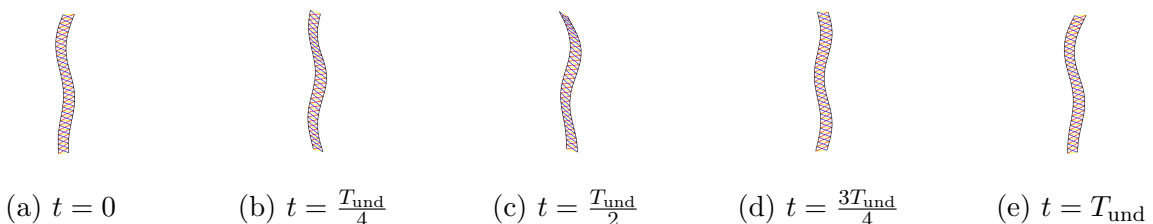


Figure E.2: Undulation Cycle of Asymmetric Swimmer

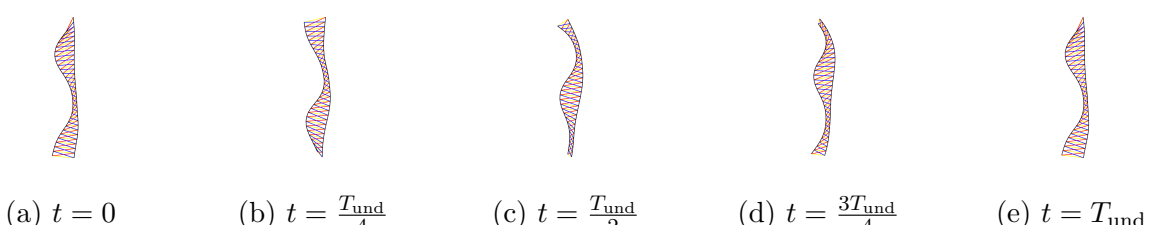


Figure E.3: Undulation Cycle of Second Asymmetric Swimmer with No Passive Links

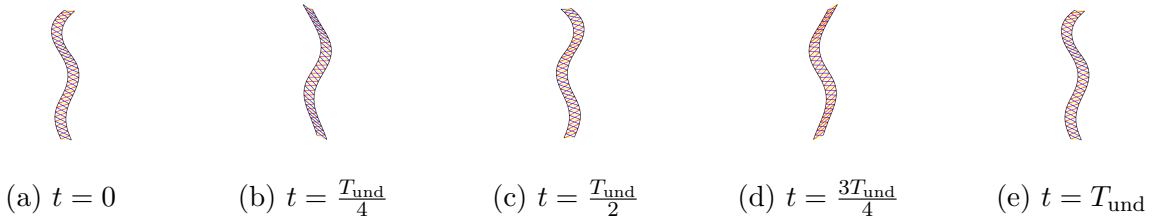


Figure E.4: Undulation Cycle of Symmetric Swimmer

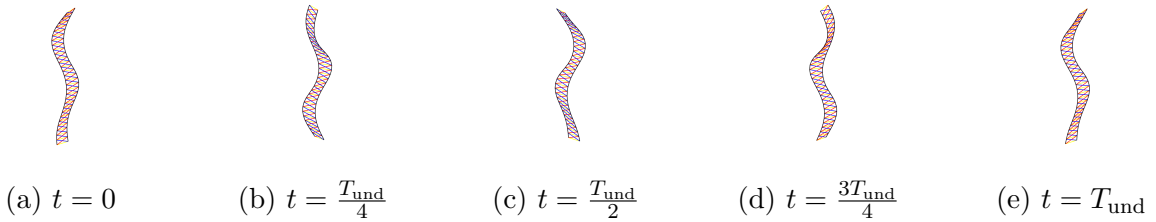


Figure E.5: Undulation Cycle of Symmetric Swimmer with No Passive Links

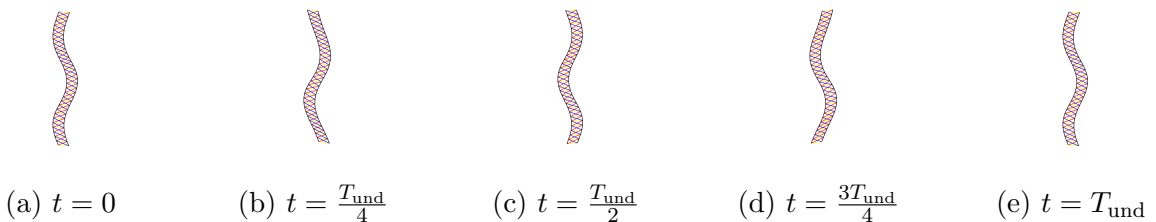


Figure E.6: Undulation Cycle of Swimmer, Final Model

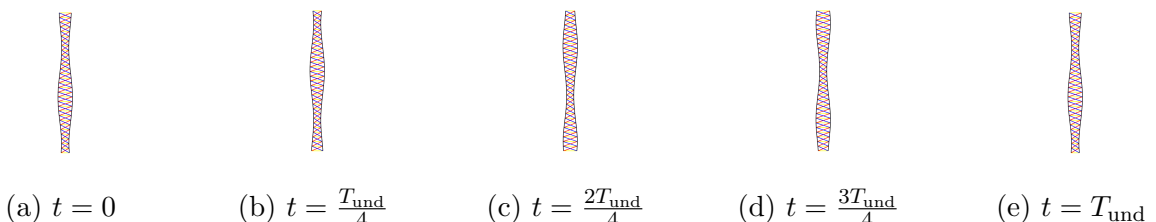


Figure E.7: Undulation Cycle of Non-Undulatory Swimmer

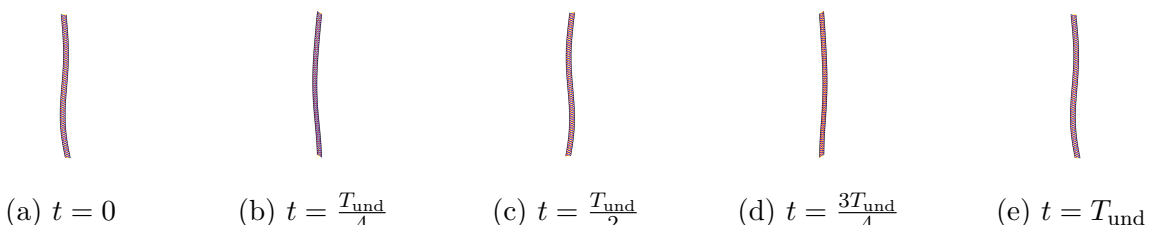


Figure E.8: Undulation Cycle of Biologically-Motivated Swimmer

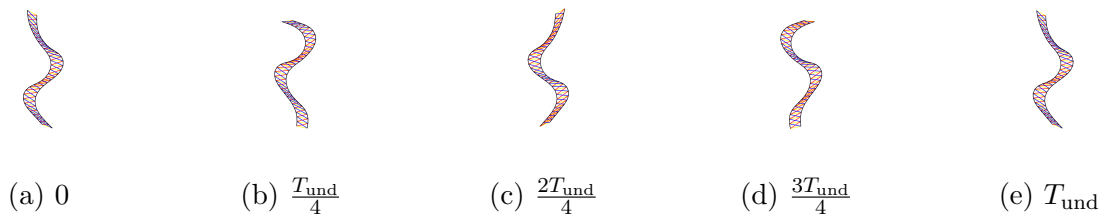


Figure E.9: Undulation Cycle of Symmetric Swimmer, Small λ_s

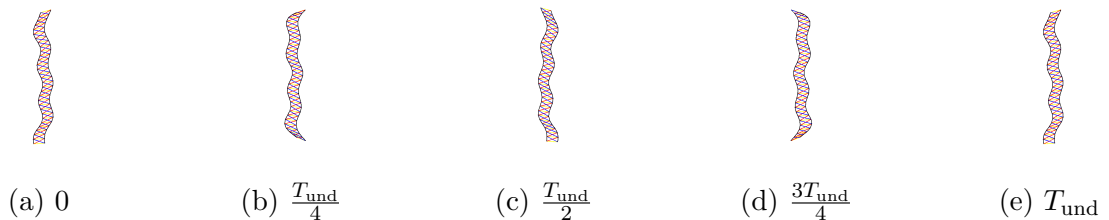


Figure E.10: Undulation Cycle of Symmetric Swimmer, High Wave Number ($k_s = 4$)

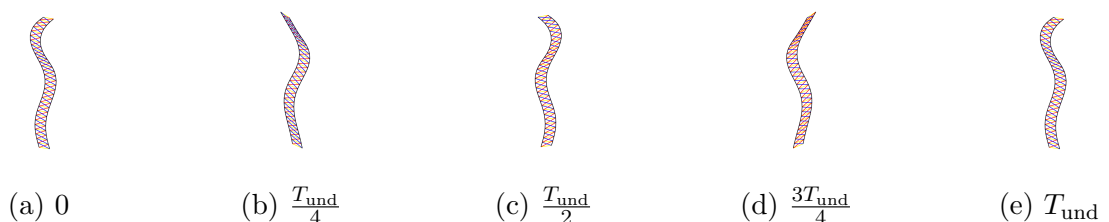


Figure E.11: Undulation Cycle of Tail-Driven Swimmer ($\beta_A = 2$, $\zeta = \frac{1}{6}$)

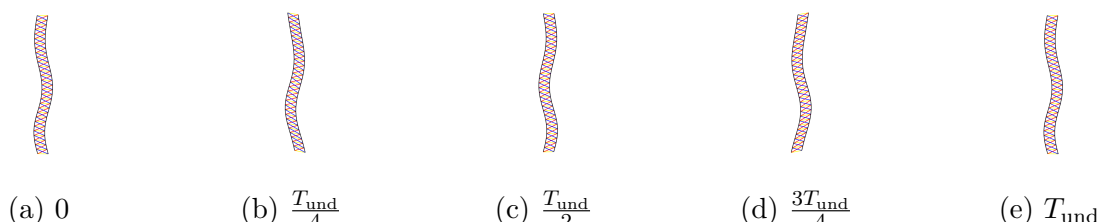


Figure E.12: Undulation Cycle of Head-Driven Swimmer ($\beta_A = \frac{1}{16}$, $\zeta = \frac{1}{5}$)

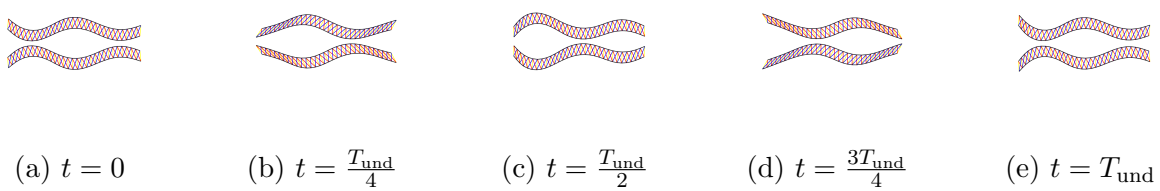


Figure E.13: Synchronisation of Swimmers with a Phase Difference $\Delta\phi = \pi$

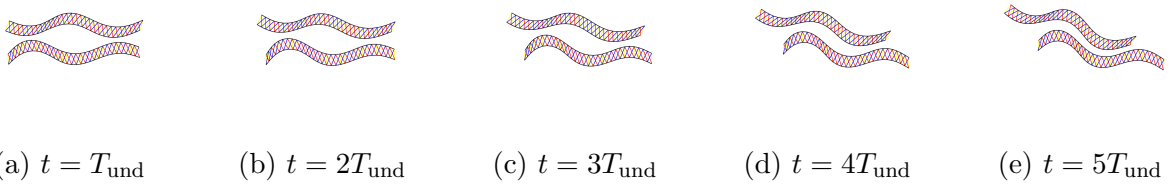


Figure E.14: Synchronisation of Swimmers with a Phase Difference $\Delta\phi = \pi - \varepsilon$

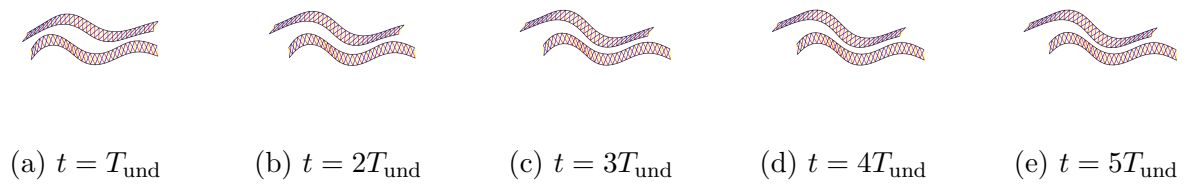


Figure E.15: Synchronisation of Swimmers with a Phase Difference $\Delta\phi = \frac{\pi}{2}$

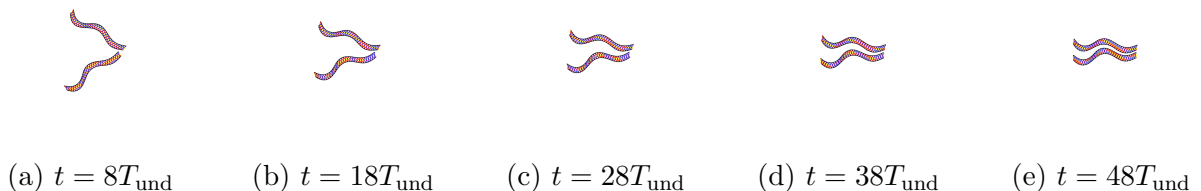


Figure E.16: Collision Between Two Swimmers

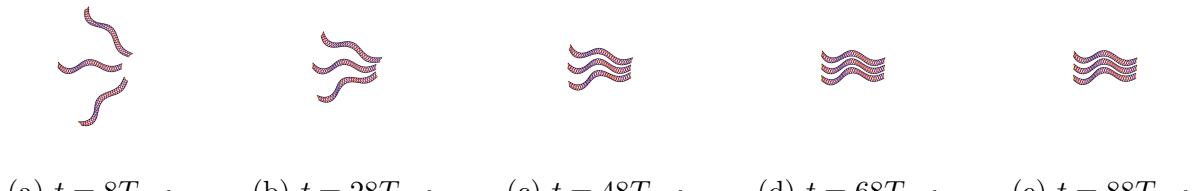
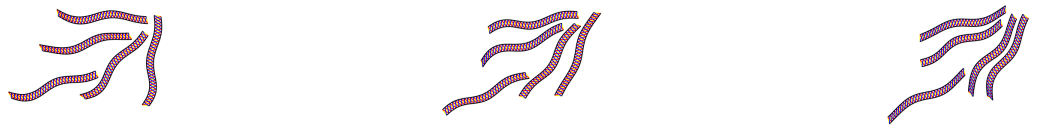


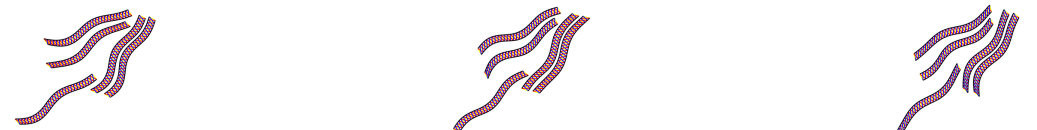
Figure E.17: Collision Between Three Swimmers



(a) $t \approx 8T_{\text{und}}$

(b) $t \approx 50T_{\text{und}}$

(c) $t \approx 92T_{\text{und}}$



(d) $t \approx 133T_{\text{und}}$

(e) $t \approx 175T_{\text{und}}$

(f) $t \approx 217T_{\text{und}}$



(g) $t \approx 258T_{\text{und}}$

(h) $t \approx 300T_{\text{und}}$

(i) $t \approx 342T_{\text{und}}$



(j) $t \approx 383T_{\text{und}}$

(k) $t \approx 425T_{\text{und}}$

(l) $t \approx 467T_{\text{und}}$

Figure E.18: Large-Scale Behaviour of Coordinated Swimmers